DECENTRALIZED STRUCTURAL DAMAGE DETECTION AND MODEL UPDATING WITH MOBILE AND WIRELESS SENSORS

A Thesis
Presented to
The Academic Faculty

by

Dapeng Zhu

In Partial Fulfillment
of the Requirements for the Degree
Doctor of Philosophy in the
School of Civil and Environmental Engineering

Georgia Institute of Technology
December 2014

DECENTRALIZED STRUCTURAL DAMAGE DETECTION AND MODEL UPDATING WITH MOBILE AND WIRELESS SENSORS

Approved by:

Dr. Yang Wang, Advisor
School of Civil and Environmental Engineering
Georgia Institute of Technology

Dr. Kok-Meng Lee, Co-advisor
School of Mechanical Engineering
Georgia Institute of Technology

Dr. Reginald DesRoches
School of Civil and Environmental Engineering
Georgia Institute of Technology

Dr. Bruce Ellingwood
Civil and Environmental Engineering
Georgia Institute of Technology

Dr. Alper Erturk
School of Mechanical Engineering
Georgia Institute of Technology

Date Approved: [August 18, 2014]

ACKNOWLEDGEMENTS

First of all, I would like to express my gratitude to my advisor, Dr. Yang Wang, for his continuous support and guidance throughout my Ph.D. life. He has kept me on the right path toward completing my degree and taught me to work proactively, for which I am extremely grateful. I would also like to thanks Dr. Kok-Meng Lee for his guidance and insightful advising on my research in the field of mobile sensor design. I would also like to thank Dr. Reginald DesRoches, Dr. Bruce Ellingwood and Dr. Alper Erturk for sitting on my dissertation committee, and for their valuable time and support of my research.

I want to thank Jiajie Guo for his assistance on developing and validating the mobile sensing network. I would like to thank Xiaohua Yi for his assistance on validating the mobile sensing network on structural damage detection. I would also like to thank Xinjun Dong for his assistance on structural modeling for model updating purpose. Sincere thanks are also given to my colleagues and friends at Georgia Tech, including Quanquan Qi, Chunxu Qu, Lei Feng, Chia-Hung Fang, Hongchuang Liu, Shuo Chen, Chunhee Cho, Xi Liu, Shaohui Foong and all others that I have not listed here, for helping me with various aspects of my research and life.

Last, but no means least, I would like to thank my wife, Feng Li, for her love and support at all times. Special thanks also owe to my parents for their encouragement and unconditional trust and love.

This research was partially funded by the National Science Foundation (CMMI-0928095, CMMI-1150700 and CMMI-1041607) and the Georgia Department of

Transportation (RP12-21). Any opinions, findings, and conclusions or recommendations expressed in this publication are those of the author and do not necessarily reflect the view of the sponsors.

TABLE OF CONTENTS

ACKNOWLEDGEMENTS III

LIST OF TABLES VIII

LIST OF FIGURES IX

SUMARY XIII

CHAPTER 1 INTRODUCTION 1

1.1 Background and Motivation 1

1.2 Research Objectives 3

1.3 Organization of the Dissertation 5

CHAPTER 2 LITERATURE REVIEW 7

2.1 Mobile Sensors for SHM 7

2.2 Structural Damage Detection Algorithms 8

2.3 Finite Element Model Updating Algorithms 9

2.3.1 Frequency-Domain Approaches 10

2.3.2 Time-Domain Approaches 11

2.3.3 Substructure Model Updating 13

CHAPTER 3 HARDWARE AND SOFTWARE DEVELOPMENT OF MOBILE SENSING NODES 16

3.1 Design of the Single-Car MSN 17

3.2 Laboratory Experiments Using the Single-Car MSN 19

3.2.1 Experimental Setup 19

3.2.2 Measurement Results from MSNs 21

3.2.3 Modal Analysis Using Mobile Sensor Data 23

3.3 Design of the Flexure-Based MSN 24

3.3.1 Reliable Mobility 26

3.3.2 Flexure-Based Design 28

3.4 Field Testing of the Flexure-Based MSNs 29

3.4.1 Test Configuration 30

3.4.2 Test Results and Modal Analysis 32

3.4.3 Preliminary Model Updating Using Mobile Sensor Data 34

3.5 Summary 38
CHAPTER 4 DECENTRALIZED STRUCTURAL DAMAGE DETECTION USING MOBILE SENSOR DATA THROUGH TRANSMISSIBILITY ANALYSIS 39
4.1 Introduction to Transmissibility Function Analysis 40
4.2 Decentralized Damage Detection Using Mobile Sensor Data 43
4.2.1 Experimental Setup 43
4.2.2 Damage Scenario I –Mass Change 46
4.2.3 Damage Scenario II – Loosened Bolts 50
4.2.4 Damage Scenario III – Section Loss 52
4.3 Damage Sensitivity Study of Decentralized Transmissibility Functions 54
4.3.1 Transmissibility Function for A Multi-DOF Spring-Mass-Damper System 54
4.3.2 Damage Scenario I – Mass Change 57
4.3.3 Damage Scenario II – Stiffness Change 60
4.4 Numerical and Experimental Validation to Decentralized Transmissibility Analysis 64
4.4.1 Numerical Validation 64
4.4.2 Experimental Validation 67
4.5 Summary 73
CHAPTER 5 DECENTRALIZED SYSTEM MODEL UPDATING THROUGH MINIMIZATION OF MODAL DYNAMIC RESIDUALS 75
5.1 Substructure Modeling 76
5.1.1 Structural Model Condensation 76
5.1.2 Sensitivities of Model Updating Variables 78
5.2 Substructure Updating 80
5.2.1 Modal Dynamic Residual Approach 81
5.2.2 Modal Property Difference Approach 84
5.3 Numerical Validation 85
5.3.1 Lumped Spring-Mass Model 85
5.3.2 Plane Truss Model 89
5.3.3 Plane Frame Model 92
5.3.4 Space Frame Model 95
5.3.5 Discussion of Model Updating Results 100
5.4 Investigations on Substructure Location and Size 101

5.4.1 Performance Comparison with Model Updating of Entire Structure 101
5.4.2 Investigation on Substructure Location 104
5.4.3 Performance Evaluation of Substructure Size 108
5.5 Summary 112
CHAPTER 6 CONCLUSIONS AND FUTURE DIRECTIONS 114
6.1 Conclusions 114
6.2 Future Work 116
REFERENCES 118

LIST OF TABLES

TABLE 3.1. Dimensions of the steel bridge 30

TABLE 3.2. Selected parameters for model updating 35

TABLE 3.3. Comparison of modal properties extracted from mobile sensing data and FE model 37

TABLE 4.1. Model properties of the 10-DOF spring-mass-damper model 64

TABLE 4.2. First five natural frequencies for undamaged five-story shear building 68

TABLE 5.1. Structural properties in the selected substructure 86

TABLE 5.2. Updated parameter changes (%) for substructure elements on the lumped spring-mass model by minimization of modal dynamic residuals 87

TABLE 5.3. Updated parameter changes (%) for substructure elements on the lumped spring-mass model by minimization of modal property differences 88

TABLE 5.4. Structural properties of the plane truss 89

TABLE 5.5. Updated parameter changes (%) for substructure elements on the plane truss model by minimization of modal dynamic residuals 90

TABLE 5.6. Updated parameter changes (%) for substructure elements on the plane truss model by minimization of modal property differences 91

TABLE 5.7. Updated parameter changes (%) for substructure elements on the plane frame model by minimization of modal dynamic residuals 93

TABLE 5.8. Updated parameter changes (%) for substructure elements on the plane frame model by minimization of modal property differences 95

TABLE 5.9. Structure stiffness parameters 96

TABLE 5.10. Updated parameter changes (%) for substructure elements on the space frame model by minimization of modal dynamic residuals 98

TABLE 5.11. Updated parameter changes (%) for substructure elements on the space frame model by minimization of modal property differences 100

TABLE 5.12. Updated stiffness parameter changes (%) for the entire structure by minimization of modal dynamic residuals 103

TABLE 5.13. Updated stiffness parameter changes (%) for the substructure models with five available modes 106

TABLE 5.14. Updated parameter changes (%) for substructure elements on the smaller substructure model by minimization of modal dynamic residuals 110

TABLE 5.15. Updated parameter changes (%) for substructure elements on the larger substructure model by minimization of modal dynamic residuals 111

LIST OF FIGURES

Figure 1.1. Comparison between static sensor networks and mobile sensor networks: (a) A static sensor network with fixed deployment scheme and low spatial resolution; (b) A mobile sensor network with flexible deployment scheme and high spatial resolution..... 3

Figure 3.1. Pictures of a single-car MSN: (a) front view; (b) back view 17

Figure 3.2. Functional diagram of the single-car MSN 18

Figure 3.3. 2D steel portal frame for testing MSNs..... 20

Figure 3.4. Two example test configurations from Figure 3.3 (a) configurations #3; (b) configuration #6 21

Figure 3.5. A single-car MSN transiting over the beam-column connection of the laboratory steel frame: (a) on the column; (b) at the corner; (c) on the beam 21

Figure 3.6. Comparison between static and mobile sensor data at two locations..... 22

Figure 3.7. Comparison between data measured by a MSN and a static sensor mounted on the left column: (a) time history data; (b) FFT results..... 23

Figure 3.8. First four vibration mode shapes identified using mobile sensor data 24

Figure 3.9. Photo of the flexure-based MSN 25

Figure 3.10. Functional diagram of the flexure-based MSN 26

Figure 3.11. A Hall effect sensor measuring wheel rotation: (a) sensor is placed above a rotating magnet wheel; (b) the output signal of the Hall effect sensor when the magnet wheel rotates 27

Figure 3.12. Side view of the magnet-wheeled MSN: (a) transition over a right angle; (b) sensor attachment; (c) sensor detachment..... 28

Figure 3.13. Photo of the space frame bridge on Georgia Tech campus 29

Figure 3.14. Experimental setup for mobile sensor testing: (a) 3D illustration of five measurement configurations for the MSNs; (b) a laptop as the wireless server; (c) four MSNs deployed at the 1st configuration; (d) an MSN attaches an accelerometer onto the structural surface; (e) a hammer impact is being applied 31

Figure 3.15. Experimental setup for the testing with static wireless sensors 32

Figure 3.16. Example vibration records and corresponding frequency spectra recorded by mobile sensors when hammer impact is applied on the floor below location 8N 32

Figure 3.17. Example vibration records and corresponding frequency spectra recorded by static sensors when hammer impact is applied on the floor below location 8N 33

Figure 3.18. First three mode shapes of the bridge extracted from mobile sensing data with hammer impact excitation..... 34

Figure 3.19. First three mode shapes of the bridge extracted from static sensor data with hammer impact excitation..... 34

Figure 3.20. FE model for the steel bridge: (a) 3D view of the bridge model; (b) support condition at MRDC side for model updating; (c) support condition at MARC side for model updating..... 35

Figure 3.21. First five mode shapes of the FE model..... 37

Figure 4.1. Laboratory steel portal frame for damage detection using mobile sensing nodes: (a) photo of the portal frame with two mobile nodes at locations A1 and A2; (b) schematic of sensor and impact locations, where undimmed area shows hammer impact being applied between A1 and A2..... 43

Figure 4.2. Acceleration data recorded by mobile sensing nodes: (a) location A1; (b) location A2. Hammer impact is applied between A1 and A2 (as shown in Figure 4.1b) 44

Figure 4.3. Frequency spectra of the mobile sensing data in Figure 4.2: (a) location A1; (b) location A2..... 45

Figure 4.4. Repeatability of transmissibility functions among data sets for undamaged structure..... 46

Figure 4.5. Damage Scenario I – an extra mass block and two mobile sensing nodes, one node allocated at location A1, and the other node at A2 (locations A1 and A2 are as shown in Figure 4.1b)..... 47

Figure 4.6. Damage Scenario I – comparison of transmissibility functions between data sets of the undamaged and damaged structures..... 48

Figure 4.7. Damage Scenario I – the damage indicators and repeatability indicators for ten pairs of measurement locations..... 49

Figure 4.8. Damage Scenario II – the torque of each of the four bolts is reduced from 13.56Nm (120 lbs-in) to 0.565Nm (5lbs-in). The bolts are between locations A3 and A4 shown in Figure 4.1(b)..... 50

Figure 4.9. Damage Scenario II – comparison of transmissibility functions between data sets of the undamaged and damaged structures..... 51

Figure 4.10. Damage Scenario II – the damage indicators and repeatability indicators for ten pairs of measurement locations..... 51

Figure 4.11. Damage Scenario III – loss in section area is introduced to the left column between locations A2 and A3 shown in Figure 4.1(b)..... 52

Figure 4.12. Damage Scenario III – comparison of transmissibility functions between data sets of the undamaged and damaged structures..... 53

Figure 4.13. Damage Scenario III – the damage indicators and repeatability indicators for ten pairs of measurement locations..... 53

Figure 4.14. A multi-DOF spring-mass-damper system..... 54

Figure 4.15. Damage scenario I: mass change at DOF n, while measurements are taken at DOFs i and $j=i+1$. The external excitation is applied at DOF $i+1$: (a) $i < n$; (b) $i = n$; (c) $i > n$..... 58

Figure 4.16. Damage scenario II: stiffness loss between DOFs n-1 and n, while measurements are taken at DOFs i and $j = i+1$. An external excitation is applied at DOF i+1: (a) $i < n$-1; (b) $i = n$-1; (c) $i = n$; (d) $i > n$ 61

Figure 4.17. Comparison of transmissibility functions between undamaged structure and damaged structure with mass change..... 65

Figure 4.18. Damage scenario I - the damage indicators of the nine measurement pairs 66

Figure 4.19. Comparison of transmissibility functions between undamaged structure and damaged structure with stiffness loss 67

Figure 4.20. Damage scenario II - the damage indicators of the nine measurement pairs 67

Figure 4.21. A five-story shear-building structure..... 68

Figure 4.22. Test configurations with MSNs..... 69

Figure 4.23. Example acceleration time histories when the hammer impact is applied at the 3rd floor: (a) acceleration at the 2nd floor; (b) acceleration at the 3rd floor 69

Figure 4.24. Example acceleration spectra when the hammer impact is applied at the 3rd floor: (a) acceleration spectra at the 2nd floor; (b) acceleration spectra at the 3rd floor.. 70

Figure 4.25. Transmissibility function T_{23} calculated using the example acceleration data 70

Figure 4.26. Damage scenario I – a 0.5kg additional mass is attached on the 2nd floor.. 71

Figure 4.27. Comparison of averaged transmissibility functions between undamaged structure and damaged structure (with additional mass)..... 71

Figure 4.28. Damage scenario I - the damage indicators at four measurement pairs 72

Figure 4.29. Damage scenario II - 20% stiffness loss is introduced to the section of one column between 2nd and 3rd floors 72

Figure 4.30. Comparison of averaged transmissibility functions between undamaged structure and damaged structure (with stiffness loss) 73

Figure 4.31. Damage scenario II - the damage indicators at four measurement pairs..... 73

Figure 5.1. Illustration of substructure modeling strategy 77

Figure 5.2. Pseudo code of the iterative linearization procedure..... 82

Figure 5.3. Illustration of substructure selection (10% stiffness reduction is introduced to k_{20}, k_{30}, k_{45}, k_{50}, k_{60}, k_{62}, k_{82}, k_{100}, k_{120}, and k_{150} as damage) 86

Figure 5.4. Relative errors of the updated parameters on the lumped spring-mass model by minimization of modal dynamic residuals 87

Figure 5.5. Relative errors of the updated parameters on the lumped spring-mass model by minimization of modal property differences..... 88

Figure 5.6. Illustration of substructure selection of a plane truss 89

Figure 5.7. Relative errors of the updated parameters on the plane truss model by minimization of modal dynamic residuals 91

Figure 5.8. Relative errors of the updated parameters on the plane truss model by minimization of modal property differences 92
Figure 5.9. Illustration of substructure selection of a plane portal frame 92
Figure 5.10. Relative errors of the updated parameters on the plane frame model by minimization of modal dynamic residuals 94
Figure 5.11. Relative errors of the updated parameters on the plane frame model by minimization of modal property differences 95
Figure 5.12. Illustration of substructure selection of a space frame bridge 95
Figure 5.13. Detailed view of the substructure showing stiffness parameters to be updated 97
Figure 5.14. Sensitivities of the updated parameters to the objective function 99
Figure 5.15. Relative errors of the updated parameters on the space frame model by minimization of modal dynamic residuals 99
Figure 5.16. Relative errors of the updated parameters on the space frame model by minimization of modal property differences 100
Figure 5.17. Uniform sensor instrumentation on the entire structure 102
Figure 5.18. Relative errors of the updated parameters for the entire structure by minimization of modal property differences 103
Figure 5.19. Substructures at various locations 105
Figure 5.20. Relative errors of the updated parameters for substructures at various locations 107
Figure 5.21. Smaller substructure with first two segments 109
Figure 5.22. Larger substructure with first four segments 109
Figure 5.23. Relative errors of the updated parameters for the smaller substructure 110
Figure 5.24. Relative errors of the updated parameters for the larger substructure 111
Figure 5.25. Relative errors of the updated parameters for the substructure with three frame segments in Section 5.3.4 (excluding E_4) 111

SUMMARY

Recent years have seen increasing research interest in structural health monitoring (SHM). Among the many advances in SHM research, "smart" wireless sensors capable of embedded computing and wireless communication have been highly attractive. Wireless communication in SHM systems was originally proposed to significantly reduce the monetary and time cost for installing lengthy cables in an SHM system. Besides wireless sensing, the next revolution in sensor networks has been predicted to be mobile sensor networks that implant mobility into traditional wireless sensor networks.

This research explores decentralized structural model updating and damage detection using mobile and wireless sensors. In the first stage of this research, mobile sensing nodes (MSNs) are developed for SHM purposes. The MSNs can maneuver upon structures built with ferromagnetic/steel materials. The first generation adopts a single-car design, and accelerometers are fixed on the body. As a result, the accelerometer cannot be directly installed on structural surface. The second generation adopts a flexure-based design with a flexible beam connecting two car bodies. The flexure-based design can attach an accelerometer to structural surface during measurement, so that measurement accuracy is improved. The performance of the MSNs is validated through laboratory and field experiments.

To further investigate the mobile sensing strategy, transmissibility analysis is applied on mobile sensing data for structural damage detection. A decentralized structural damage detection procedure is proposed herein for the MSNs. The decentralized procedure only requires measurements in one small neighborhood at a time, and thus, is ideal for adoption by a small group of MSNs that take measurements in one area at a time and automatically scan through a structure. Laboratory experiments are conducted on a steel portal frame where various structure damage scenarios are emulated. Besides

experiments with MSNs, this study also investigates the nature of transmissibility functions for damage detection in an analytical manner based on a general multi-DOF spring-mass-damper system. The analytical derivation is validated through numerical simulation and laboratory experiments using MSNs.

Finally, this research also explores substructure model updating through minimization of modal dynamic residuals, which can best benefit from dense mobile or wireless sensor data concentrated in one area. The entire structural model is divided into a substructure, corresponding to the area currently being instrumented and to be updated, and the residual structure. The Craig-Bampton transform is adopted to condense the residual structure using a limited number of dominant mode shapes, while the substructure model remains at high resolution. To update the condensed structural model, physical parameters in the substructure and modal parameters of the residual structure are chosen as optimization variables; minimization of the modal dynamic residuals is determined as the optimization objective. An iterative linearization procedure is adopted for efficiently solving the optimization problem. The presented substructure updating method is validated through numerical examples. For comparison, a conventional approach minimizing modal property differences is also applied, and shows worse updating accuracy than the proposed approach. The performance of the proposed substructure model updating approach is further investigated through numerical simulation of three topics of interest, i.e. performance comparison with model updating of entire structure, investigation on substructure location, and investigation on substructure size.

CHAPTER 1 INTRODUCTION

In this chapter, Section 1.1 first briefly introduces the background and motivation of this research. Section 1.2 discusses research purpose and objective. Finally, Section 1.3 presents the organization of this dissertation.

1.1 Background and Motivation

The deterioration of civil infrastructure systems is a constant challenge faced by today's civil engineers. In the United States, more than half of the bridges were built before 1940's, and more than one in nine of the bridges were categorized as structurally deficient [1]. It was estimated that a $20.5 billion annual investment is needed to substantially improve the bridge conditions, yet currently, only $12.8 billion is available annually. Due to the lack of funding for timely retrofitting, average condition of the bridges in the US is expected to continuously deteriorate in the foreseeable future. In order to efficiently utilize the limited resources, a need-based scheduling for bridge retrofitting should be established based upon the actual condition of individual bridges.

The U.S. federal highway administration (FHWA) requests local transportation authorities to inspect the entire inventory of over 600,000 highway bridges every two years. These biennial inspections may not be timely enough for capturing rapidly growing structural damage. As shown by a FHWA study, visual inspections are highly subjective; significantly different condition ratings can be given for the same bridge by different inspectors [2]. Furthermore, visual inspections can only identify damage that is visible on the structural surface; damage located below the surface often remains unrevealed. As a result, there is a pressing need for reliable structural monitoring systems that can automatically and quantitatively assess the real-time condition of civil structures.

As a complimentary approach to visual inspections, structural health monitoring (SHM) systems have been widely studied for assessing the condition of large-scale civil structures [3, 4]. Environmental excitation/condition and structural response data are used for identifying subtle structural abnormalities. In an SHM system, various types of sensors, such as accelerometers, stain gauges, thermometers, displacement and velocity transducers, can be used for monitoring structural behavior. A data acquisition (DAQ) system usually collects all the sensor measurements at a central server. Traditionally, cable connections between sensors and the central server are used. Cable installation usually suffers from high cost and is time consuming. For example, the cost of installing a typical structural monitoring system in a mid-rise building can exceed a few thousand dollars per sensing channel [5]. Extensive lengths of cables can consume over 75% of the total installation time for a cabled SHM system [6]. In order to overcome the difficulties associated with cable installation, wireless SHM systems have been developed by exploiting latest advances in microelectromechanical systems (MEMS) and wireless communication [6-11]. MEMS and wireless technology lead to the development of smart, low-cost, miniaturized wireless sensing nodes that are capable of collecting sensor data and wirelessly transmitting data without the need of cables. For example, the wireless SHM platform developed by Wang *et al*. [12] has been successfully validated on a number of bridges, buildings, and wind turbines, including structures located in the US, Taiwan, South Korea, China, and Germany [13-15].

Low-cost wireless sensing units usually need to be incorporated with high-precision accelerometers for accurate vibration measurement and system identification of civil structures. Such an accelerometer typically costs at least a few hundred dollars. Therefore, even using a wireless SHM system, it is still usually unaffordable to densely instrument a civil structure with a large number of sensors. On the other hand, a small number of sensors on a structure can only provide very coarse spatial resolution that is far from enough for high-accuracy system model updating and damage detection. The next

revolution of wireless sensor network is predicted to be mobile sensor network [16]. A mobile sensor network contains multiple mobile sensing nodes (MSNs). Each MSN can be a miniature robot equipped with smart wireless sensors. The MSN explores its surroundings and exchanges information with peers through wireless communication. Compared with static wireless sensor deployment, MSNs can take measurements in one small neighborhood at a time to achieve high spatial resolutions. After measurement, the limited number of MSNs move to the next configuration, and repeat the procedure till the entire structure is scanned. In short, adaptive and high spatial resolutions can be achieved using a relatively small number of mobile sensor nodes and with little human effort, as shown in Figure 1.1.

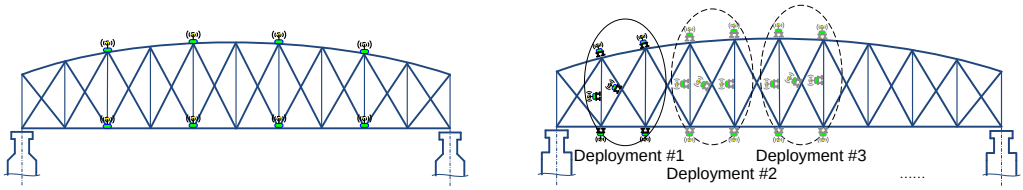

(a) (b)

Figure 1.1. Comparison between static sensor networks and mobile sensor networks: (a) A static sensor network with fixed deployment scheme and low spatial resolution; (b) A mobile sensor network with flexible deployment scheme and high spatial resolution

1.2 Research Objectives

The main research objective of this dissertation is to investigate mobile sensing networks for SHM. To best utilize the mobile sensing data with high spatial resolution and concentrated in a small neighborhood of a large structure, decentralized structural damage detection and model updating algorithms are proposed. In contrast to centralized approaches that operate on an entire structure model and require data from the entire structure, the decentralized approaches operate on a local part of a structure and mainly require only local structural response data. The objectives are elaborated as followings:

1. Develop magnetic wheeled mobile sensing nodes (MSNs) that are capable of reliably navigating steel structures with narrow sections, high abrupt angle changes, inclined elements, and underside surfaces. Meanwhile, the MSNs can provide accurate acceleration data and transmit the data through wireless communication. The MSNs will be validated through laboratory and field experiments.

2. Explore decentralized structural damage detection using transmissibility functions of mobile sensor data. The transmissibility function is defined as the ratio between the response vibration spectra of two locations. The decentralized structural damage detection procedure only requires measurements in one small neighborhood at a time, and thus, is ideal for adoption by a small group of MSNs that take measurements in one area at a time and automatically scan through a structure. Laboratory experiments will be conducted with MSNs to detect various emulated structural damage scenarios. Besides experiments with MSNs, the nature of transmissibility functions for damage detection will be investigated in an analytical manner for a general multi-DOF spring-mass-damper system. Finally, the analytical derivation will be validated through numerical simulation and laboratory experiments using MSNs.

3. Investigate decentralized structural model updating through minimization of modal dynamic residuals. The entire structural model is divided into a substructure (currently being instrumented and to be updated) and the residual structure. The Craig-Bampton transform is adopted to condense the residual structure using a limited number of dominant mode shapes, while the substructure remains at high resolution. To update the condensed structural model, physical parameters in the substructure and modal parameters of the residual structure are chosen as optimization variables; minimization of the modal dynamic residuals is determined as the optimization objective. The proposed substructure updating approach will be validated through numerical examples, and compared with a conventional approach minimizing modal property differences. Furthermore, the performance of the proposed substructure model updating approach will

be further investigated through numerical simulation of three topics of interest, i.e. performance comparison with model updating of entire structure, investigation on substructure location, and investigation on substructure size.

1.3 Organization of the Dissertation

The rest of this dissertation is organized as follows.

Chapter 2 conducts detailed technical reviews, including the development of mobile sensors for SHM, structural damage detection algorithms, and finite element model updating algorithms.

Chapter 3 presents two mobile sensing prototypes developed for SHM. The first prototype adopts a single-car design, and its performance is validated through laboratory experiments. The second prototype adopts a flexure-based design to offer more accurate measurement. Field testing is conducted on a campus pedestrian bridge to validate the performance of the flexure-based MSN.

Chapter 4 proposes a decentralized structural damage detection approach using MSNs. The basic formulation of transmissibility function analysis is introduced first. Then laboratory experiments are conducted to verify the decentralized damage detection using MSNs. Analytical studies on damage sensitivity of the decentralized transmissibility functions are proposed, followed by numerical simulation and experimental validation using MSNs.

Chapter 5 proposes a decentralized structural model updating approach through minimization of modal dynamic residuals. The formulation of substructure modeling is presented first, followed by a description of substructure updating through an optimization procedure of minimizing of modal dynamic residuals. The proposed approach is then validated through a number of numerical examples. The proposed substructure model updating approach is further explored through numerical simulations

for a few key issues, such as comparison with updating an entire structure, and guidance to choose appropriate substructure location and size.

Chapter 6 presents a summary of the research and primary conclusions. Further research topics are recommended.

CHAPTER 2 LITERATURE REVIEW

This chapter begins with the review on mobile sensors for SHM, and then discusses relevant work on structural damage detection and finite element model updating.

2.1 Mobile Sensors for SHM

As a transformative change to wireless sensing, mobile robots have been explored in recently years for automatically inspecting engineered structures. These inspection robots have been mainly used for individual and localized nondestructive evaluation, rather than as a mobile sensing network that provides meaningful and coordinated measurements at multiple locations. For example, to inspect the inner casing of ferromagnetic pipes with complex-shaped structures, a compact robot with two magnetic wheels in a motorbike arrangement has been developed [17]. In another example, a mobile inspection robot was designed with an automatic pipe tracking system through machine vision for inspecting exterior surface of pipes [18]. An agile wall climbing robot was developed for navigating on smooth surface of any orientation by employing elastomeric dry adhesion [19]. Another climbing robot was developed by utilizing alternating handholds. The tail of the robot can help the robot adjust its orientation during climbing [20]. Some researchers have incorporated mobility with traditional sensors for SHM. For example, a beam-crawler has been developed for wirelessly powering and interrogating battery-less peak-strain sensors; the crawler moves along the flange of an I-beam by wheels [21]. A robot able to crawl on a 2D surface was developed for visually inspecting an aircraft exterior; the robot used ultrasonic motors for mobility and suction cups for adhesion [22]. More recently, a remotely-controlled model helicopter has been demonstrated for charging and communicating with wireless sensors as a mobile host [23]. However, to the best of our knowledge, mobile sensor networks with dynamic reconfiguration have rarely been explored by researchers for SHM purpose.

2.2 Structural Damage Detection Algorithms

In recent years, significant research efforts have been devoted to nondestructive structural damage detection techniques for identifying the existence of damage in structures [24, 25]. Most of the algorithms can be categorized as two groups. The first category is local damage identification, such as acoustic emission [26], laser image [27], radar image [28], and impact-echo [29], etc. These approaches are applied mainly to detect local structural defect, such as cracks and erosion. The second category is global damage identification, which has been mainly applied on structural vibration data. These approaches are based on the assumption that damage induced changes in structural mass, damping, or stiffness cause detectable changes in vibration properties, such as frequency response function, modal properties, etc. For example, a comprehensive review on work on vibration-based damage identification algorithms can be found in [24, 25]. Nevertheless, very few studies explore decentralized structural damage detection. One such example is [30], where frequency response functions are adopted to locate substructure damage on building structures under an earthquake excitation. Recording of ground excitation is required for calculating frequency response functions.

Among vibration-based damage identification approaches, transmissibility function analysis attracts considerable interest due to its effectiveness in damage identification, and independency to the magnitude and waveform of the excitation records. Based on these features, transmissibility functions can be potentially applied on mobile sensor data for decentralized structural damage detection without recording structural excitations. A number of researchers investigated the application of transmissibility function analysis for damage detection in past decades. For example, Zhang *et al.* studied the performance of transmissibility functions for damage detection within various frequency ranges through a laboratory experiment [31]. In the experiment, a piezoceramic patch actuator was used to excite a cantilever beam, in which translational and curvature transmissibility functions were adopted to calculate damage indicators and

successfully locate damage. Kess and Adams analyzed the effects of operational and environmental variability on the transmissibility function analysis for damage detection on a woven composite plate [32]. Their work suggested that the damage detection accuracy based on transmissibility function could be improved by identifying specific frequency ranges that are more sensitive to damage and immune to sources of uncertainties. Devriendt and Guillaume [33] concluded that arbitrary forces could be used to perform the transmissibility-function-based operational modal analysis, as long as the structure is persistently excited in the frequency range of interest. Mao and Todd analyzed the uncertainty of the magnitude of transmissibility functions under random excitation [34]. The probability density of transmissibility functions were derived and validated through Monte Carlo simulation. Finally, Johnson and Adams explored the explicit formulation of transmissibility functions using a three degrees-of-freedom (DOFs) system [35]. Nevertheless, little research has been devoted to exploring decentralized damage detection using transmissibility function analysis. Furthermore, analytical nature of transmissibility functions for damage detection of general structures with an arbitrary number of DOFs is not available in the literature.

2.3 Finite Element Model Updating Algorithms

In modern structural analysis, a great amount of efforts have been devoted to developing accurate finite element (FE) models. However, predictions by numerical models often differ from experimental results. The discrepancy may be caused by various inaccuracies in numerical models. For example, in actual civil structures, the connections are far more complicated than ideal hinges or fixed connections, although ideal connections are commonly used in FE models. Besides, some critical structural components may deteriorate over time. FE models based on original structural drawings cannot accurately describe the deteriorated structure.

To obtain a more accurate FE model, experimental data collected from the actual structure can be used to update the FE model, which is known as model updating. The updated model can predict structural response with higher fidelity. In addition, by tracking major property change at individual structural components, model updating can assist in diagnosing structural damage. Most of the existing FE updating algorithms are based upon structural vibration data and can be categorized into two groups, i.e. frequency-domain approaches and time-domain approaches. This section first reviews these two groups of algorithms, and then discusses their application in a substructure context.

2.3.1 Frequency-Domain Approaches

Frequency-domain approaches update an FE model using frequency-domain structural properties extracted from experimental measurement (including natural frequency, mode shape, and damping ratio) [36]. According to the typical eigenvalue equation in structure dynamics, some early researchers directly reconstructed system matrices using modal properties from experimental data, in a one-step non-iterative procedure [37, 38]. However, these approaches cannot ensure that updated matrices maintain the same sparsity patterns and entry-wise relationships that should originate from the global matrix assembly. Therefore, the updating results do not maintain structural connectivity and cannot be related to physical quantities of individual structural members.

Iterative model updating algorithms have become more popular because they can maintain structural connectivity and identify physical parameters, such as elastic modulus, density, cross section, dimensions, etc. Difference between experimental measurements and FE simulations are typically used to construct the objective function of an optimization problem. The optimization procedure searches for optimal parameter values that minimize the difference. To this end, many research efforts have been devoted

to choosing appropriate objective functions for model updating. The difference in experimental and simulated modal properties is often adopted, because modal properties are intrinsic to the structure and independent of external excitation. For example, Salawu reviewed various model updating algorithms using natural frequencies, and concluded that it may not be sufficient to identify system parameters using changes in frequency only [39]. Moller and Friberg adopted an objective function based on modal accuracy criterion (MAC) for updating an industrial structure [40]. Jaishi and Ren built an objective function based on changes in frequency, MAC values and modal flexibility [41]. Farhat and Hemez constructed an objective function using modal dynamic residuals [42]; an iterative least square procedure was developed to expedite computation in the optimization procedure. Sanayei, *et al*. formed an objective function using condensed modal dynamic residuals to the measured degrees of freedom (DOFs) for identifying structural parameters [43, 44]. A comparative study between the objective functions based on modal dynamic residuals and modal property differences was conducted using noisy measurement [45]; it was concluded that the modal dynamic residual approach shows better convergence than modal property difference approach.

Despite previous studies, limitations exist in the frequency-domain FE updating approaches. First, these approaches are limited to the updating of linear dynamical systems. Second, when applied to a high-resolution model of a large structure, most existing algorithms suffer computational challenges and convergence problem. The difficulties come from the fact that most of the existing algorithms operate on an entire structural model which can have very large amount of DOFs.

2.3.2 Time-Domain Approaches

Compared to frequency-domain approaches, time-domain approaches deal with time history data directly, without the requirement for extracting accurate modal properties. In addition, some time-domain approaches are capable of updating nonlinear

structures. Early research started with classical least-squares estimation (LSE) approach [46] and extended Kalman filter (EKF) approach [47] for model updating. In the LSE approach, the traditional equations of motion are re-written in a form where the external input is equated to the product of a sensitivity matrix and a vector of system parameters. To build the sensitivity matrix, the displacement, velocity and acceleration histories of all DOFs are required. However, for practical applications of LSE, velocity and displacement are usually obtained through numerically integration of acceleration data, which can cause a significant numerical drift. The EKF approach forms a new state vector containing the displacement and velocity of all DOFs, as well as system parameters. This new state vector is predicted through state equation and corrected by minimizing the difference between prediction and measurement. Compared to the LSE approach, the EKF approach can work without displacement and velocity measurement and with only partial acceleration measurement. However, the dimension of the updating equation in EKF is much larger than the one in LSE approach. Therefore, the EKF approach more likely suffers computational difficulty.

Efforts have been made to improve convergence rate and identify time-varying parameters for EKF and LSE approaches. For example, forgetting factors were introduced to track the parameters of nonlinear hysteretic systems [48-50]. However, algorithms using forgetting factors are very sensitive to measurement noise, and cause significant oscillations to the updating results. Adaptive tracking techniques were developed afterwards for the EKF approach [51] and for the LSE approach [52]. The adaptive tracking technique shows advantages in convergence and tracking abrupt changes of structural parameters. Some studies also focused on releasing the requirement of recording system input and measurement to make the algorithms work practically [53, 54]. Besides, other estimators were also investigated for model updating, such as H_∞ filter [55], Monte Carlo filter, [56], etc. The formulations of H_∞ filter are quite similar as the formulations of EKF approach, and the difference lies in the way to formulate the

correction matrix. Therefore, the H_∞ filter-based mode updating suffers similar difficulties to the EKF approach. The Monte Carlo technique is a probabilistic approach and is capable of dealing with problems with non Gaussian noise. However, this approach requires large number of samples and suffers long computation time. In recent years, a new approach, referred to as the quadratic sum-square error (QSSE) approach has been developed [57-59]. The QSSE approach doesn't require integration to obtain displacement and velocity, thus eliminate the numerical drift problem. The dimension in the QSSE recursive process is also smaller than other approaches (e.g. EKF, H_∞ filter, Monte Carlo filter, etc), which reduces computational effort. Adaptive tracking technique is adopted in the QSSE approach for fast convergence, although limitations still exist for the QSSE approach. First, this approach may still suffer computational challenges while updating the model of a large structure with very dense measurement locations. Second, this approach may become unstable and may not converge with bad initial guess of structural parameters.

2.3.3 Substructure Model Updating

As previously discussed, both frequency-domain approaches and time-domain approaches suffer significant computational difficulty when being applied to large structures. The reason is that both approaches operate on a complete model for the entire structure. To overcome the computational difficulty, particularly to accommodate data collected at dense measurement locations, substructure-based FE model updating can be pursued. Some research activities have been devoted to substructure model updating in both frequency domain and time domain.

As an example for frequency-domain approaches, a well-known substructure modeling method is the Craig-Bampton theory that partitions a large structure into two parts connected by the interface boundary nodes: the current substructure being analyzed,

and the residual structure that contains the rest of the structure [60, 61]. In the entire structural model that couples the substructure and residual structure, dynamic response of the substructure is described in detail using ordinary finite elements; meanwhile, dynamic response of the residual structure can be described using only a limited number of dominant mode shapes. Such a sub/residual-structure approach for FE model updating was studied in [62], using a laboratory 2D rectangular frame with free boundary conditions. Other studies adopted frequency spectra for substructure model updating, by minimizing difference between simulated and experimental acceleration spectra in certain frequency range [63-65]. In [66], interface force vectors were estimated using multiple sets of measurement; the difference between multiple estimations was minimized with genetic algorithms for substructure model updating.

Among time-domain approaches, Koh *et al*. applied the EKF approach for substructure model updating of a simulated shear building model [67]. Displacement, velocity, and acceleration time histories of the interface DOFs were required, which may not be practical. Later, Koh *et al*. improved the substructure formulation by adopting the "quasi-static displacement" concept, so that only the acceleration time histories of the interface DOFs were required [68]. Trink and Koh followed the formulation in [67], and estimated interface displacement and velocity by numerical integration [69]. Another substructure model updating was proposed by Tee *et al*., in the context of first and second order model identification in conjunction with observer/Kalman filter and eigensystem realization [70]. Yuen and Katafygiotis presented a substructure model updating procedure using Bayes' theorem, without requiring interface measurements or excitation measurements [71]. In addition, the sequential nonlinear least square estimation (SNLSE) method has been explored for substructure model updating [72]. The unknown interface coupling parts were treated as unknown forces, and sequentially updated in each time step with state variables and system parameters. Finally, Hou *et al*. developed a substructure isolation approach based on virtual distortion method; the approach was

validated numerically with a plane frame, and experimentally with a continuous beam [73].

In summary, most of the existing substructure approaches have only been validated with simplistic structural models. Many approaches are reported with convergence problems either due to the bad initial guess of structural parameters or the high nonlinearity of the objective functions. There is a need to continue investigating substructure model updating on the convergence issue and validation on complicated structural models.

CHAPTER 3 HARDWARE AND SOFTWARE DEVELOPMENT OF MOBILE SENSING NODES

A mobile sensing system contains a computer server and multiple mobile sensing nodes (MSNs) that communicate with each other through a wireless network. The computer server sends various commands (such as navigation, data collection, or embedded computing) to the MSNs through wireless communication. Each MSN can be a miniature mobile robot equipped with smart sensors. The MSN explores its surroundings and exchanges information with its peers through wireless communication. The environment is a complex civil structure usually with narrow sections, high abrupt angle changes, inclined elements, and underside surfaces. Such environment requires compact mobile nodes with 3D climbing ability, as well as a high degree of mobility for negotiating obstacles.

In this study, magnet-wheeled robots are identified as a feasible approach for maneuvering upon structures built with ferromagnetic materials. Two MSN prototypes are developed. The first generation has a single-car design, and accelerometers are fixed on the body. As a result, the accelerometer cannot be directly installed on structural surface. The second generation adopts a flexure-based design with a flexible beam connecting two car bodies. The flexure-based design can attach an accelerometer to structural surface during measurement, so that measurement accuracy is improved. This chapter describes in detail the hardware and software development of the MSNs for civil structural applications. This chapter is organized as follows. Section 3.1 describes the design of the single-car MSN. Section 3.2 presents laboratory validation of the single-car prototype. Section 3.3 describes the design of the flexure-based MSN. Section 3.4 presents laboratory and field validation of the flexure-based prototype. Section 3.5 summarizes the MSNs and validation tests described in this chapter.

3.1 Design of the Single-Car MSN

Figure 3.1 shows the picture of the single-car MSN capable of moving on structures built with ferromagnetic materials [74]. Physical components of the MSN include the car body frame, three wheels, two motors, two 9V batteries, a wireless sensing unit [12], and sensors with associated hardware circuits. The MSN maneuvers with two motorized side wheels (shown in Figure 3.1(a)) and one passive middle wheel (shown in Figure 3.1(b)). The perimeters of all three wheels are surrounded with thin magnet pieces that provide enough attraction forces between the wheels and the surface of the underlying ferromagnetic structures. The magnet pieces are magnetized along the thickness direction. Two 9V batteries are placed between the servo motors, one battery powering both motors, and the other battery powering the electronic circuits. An infrared (IR) sensor is installed at each side of the MSN for detecting the boundaries of the underlying structural surface. Two Silicon Designs 2012 accelerometers are attached on the body frame of the MSN. The accelerometer shown in the lower left part of Figure 3.1(b) measures the horizontal vibration, and accelerometer shown in the lower right part of Figure 3.1(b) measures vertical vibration (with respect to the body of the MSN). The width of the MSN is about 6 in, the height 3.6 in, and the length 4.7 in. The total weight of the MSN is slightly over 1 lb, most of which are due to the magnet wheels, motors,

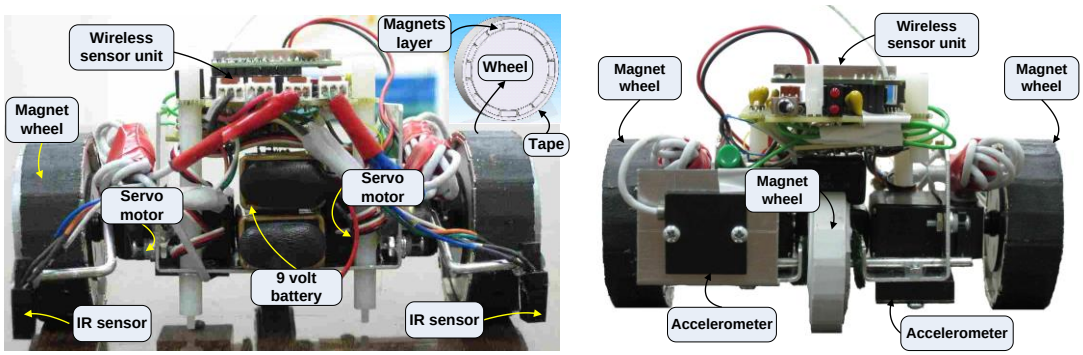

(a) (b)

Figure 3.1. Pictures of a single-car MSN: (a) front view; (b) back view

and batteries.

Figure 3.2 illustrates the functional diagram of the prototype MSN. A previously developed wireless sensing unit is adopted as the key component of this MSN. The wireless sensing unit [12] consists of three functional modules: sensor signal digitization, computational core, and wireless communication.

(i) The sensing interface, which is mainly provided by a 16-bit analog-to-digital (A/D) converter (Texas Instruments ADS8341), converts four channels of analog sensor signals into digital data which is then transferred to the computational core through a high-speed Serial Peripheral Interface (SPI) port. Sources of the sensor signals include the accelerometers and the IR sensors.

(ii) The ATmega128 microcontroller and the external Static Random Access Memory (SRAM) CY62128B together constitute the computational core that performs local data storage and analysis. In addition, each Atmel ATmega128 microcontroller provides eight 10-bit A/D channels. This resolution is lower than the ADS8341 A/D conversion.

(iii) The computational core communicates with a MaxStream wireless

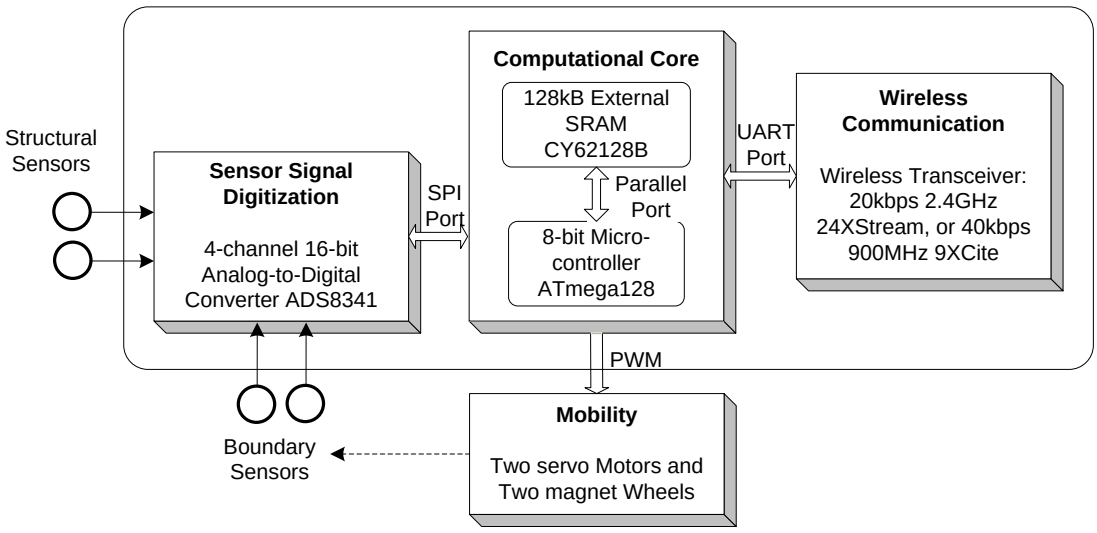

Figure 3.2. Functional diagram of the single-car MSN

transceiver through a Universal Asynchronous Receiver and Transmitter (UART) interface. Using the wireless communication channel, each wireless unit can exchange information with other units, or with the computer server.

Figure 3.2 also shows that the MSN has a mobility module that consists of two servo motors and two magnet wheels. In order to enable mobility, the ATmega128 microcontroller commands two servo motors with pulse-width-modulation (PWM) signals generated through the timer interrupt functions of the microcontroller. The speed and direction of each motor are controlled by the duty cycle of the PWM signal. To allow the MSN move safely on the underlying structural surface, two IR sensors are adopted for surface boundary detection. The IR sensors are placed at the front side of the body frame. In each IR sensor, an emitting diode emits infrared radiation, and a detection diode detects the radiation reflected from the structural surface. When a side wheel of the MSN is moving outside the surface boundary, changes can be captured from the reflected IR signal. Consequently, the microcontroller immediately sends command signals to the motors for speed adjustment, so the two driving wheels collaboratively change heading direction and maintain the MSN within the surface boundaries.

3.2 Laboratory Experiments Using the Single-Car MSN

Laboratory experiments are conducted to validate the performance of the single-car MSN. This section describes the experimental setup, as well as the structural modal analysis using the mobile sensor data.

3.2.1 Experimental Setup

A 2D laboratory steel portal frame structure is constructed for validating the performance of the single-car MSNs (Figure 3.3). The span of the portal frame is 5 ft, and the height is 3 ft. The beam and two column members have the same rectangular

section area of 6 in × 1/8 in. A hinge connection is constructed at the base of each column; the beam and the columns are connected by bolted angle plates.

Figure 3.3 also illustrates the seven configurations for deploying the mobile sensor network with four nodes. In configuration #1, all four mobile nodes are located near the base of the left column; in configuration #2, all four nodes move up to the upper part of the column, and so on. One overlapping location is allocated between every two neighboring configurations, so that the overall structural vibration mode shapes can be assembled using results from the seven configurations. Note that the two mobile sensors at the beam-column joints, i.e. the first MSN in configuration #2 and the last MSN in configuration #3, are close enough to be assumed as overlapping nodes in Figure 3.3. Figure 3.4(a) shows four prototype MSNs deployed in configuration #3, and Figure 3.4(b) shows the nodes deployed in configuration #6.

The width of the structural members is slightly larger than the width of the prototype MSN. In response to the out-of-boundary signals from the IR sensors, speed adjustments to the motors are first refined to make the MSN move safely along the beam or the two columns. Because the magnetic attraction force reduces to the minimum when the wheels move around a beam/column corner, the challenge appeared to be making the

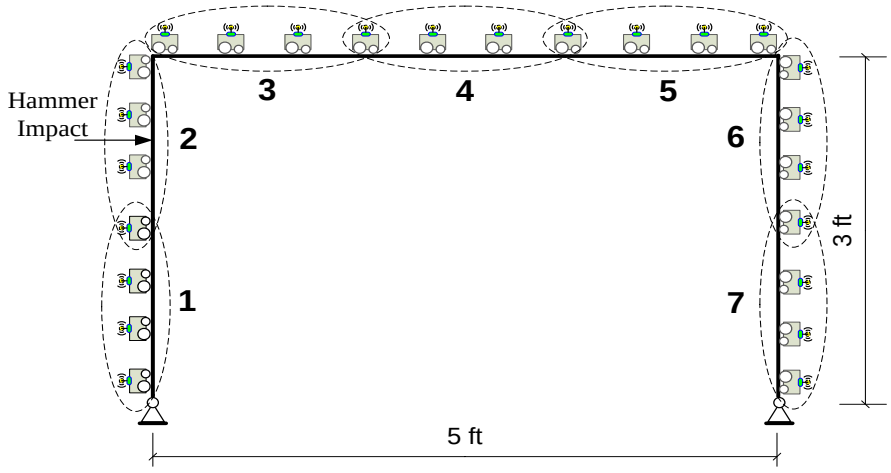

Figure 3.3. 2D steel portal frame for testing MSNs

(a) (b)

Figure 3.4. Two example test configurations from Figure 3.3 (a) configurations #3; (b) configuration #6

(a) (b) (c)

Figure 3.5. A single-car MSN transiting over the beam-column connection of the laboratory steel frame: (a) on the column; (b) at the corner; (c) on the beam

MSN capable of transiting from the columns to the beam, and vice versa. After some iterative improvements to the magnet wheel design, such as size and strength of the magnet pieces, and the associated embedded software, the MSN can reliably climb over the beam-column connections of this steel frame. Figure 3.5 shows the MSN transiting from the left column to the beam.

3.2.2 Measurement Results from MSNs

In this first prototype, the accelerometers are mounted on the car body frame of the MSN, and cannot be attached to the steel structural surface for direct measurement of

structural vibration. Therefore, it is necessary to observe the influence of the body frame vibration from the structural acceleration data. Experiments are conducted to compare the data collected by the MSN and a static sensor (Figure 3.6). In these experiments, the static sensor is mounted at the same location as the MSN. After a hammer impact, data from the MSN and the static sensor are both collected.

Figure 3.7(a) illustrates the comparison between mobile sensor data and static sensor data. A sampling frequency of 500Hz is used for both the mobile and static sensor data collection. The figures show that the mobile sensor data is very close to the static sensor data, especially a few seconds after the hammer impact. The difference is slightly larger immediately after the hammer impact, when the structural vibration contains more higher-frequency components that dissipate quickly. Dynamics of the magnet-wheeled car has little influence to lower-frequency vibration measurements, while may have more influence to higher-frequency measurements. The difference between the mobile and static sensor data in frequency domain is illustrated in Figure 3.7(b). Relatively sharp peaks around the first few natural frequencies are observed for both data sets. It can be seen that in lower frequency domain, there is negligible difference between the mobile sensor data and the static sensor data.

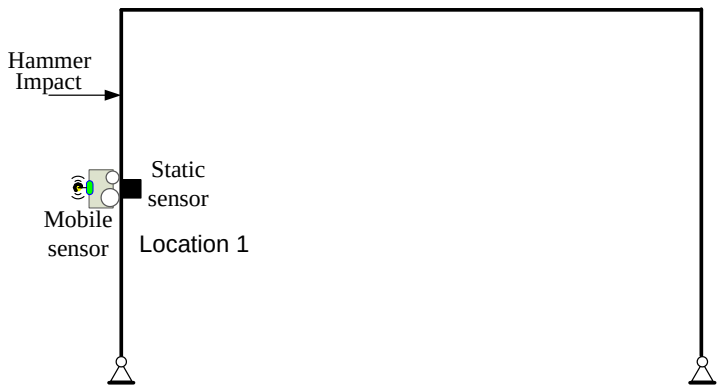

Figure 3.6. Comparison between static and mobile sensor data at two locations

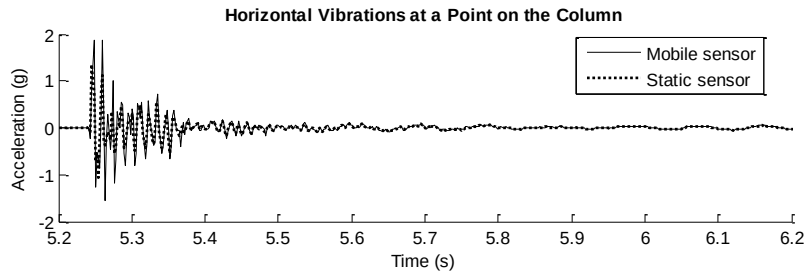

(a)

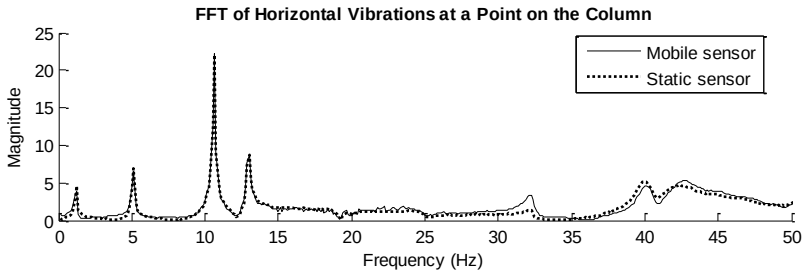

(b)

Figure 3.7. Comparison between data measured by a MSN and a static sensor mounted on the left column: (a) time history data; (b) FFT results

3.2.3 Modal Analysis Using Mobile Sensor Data

Using data collected by the mobile sensor data from hammer impact excitations, modal analysis for the steel frame is conducted. Mode shapes for different configurations are conducted individually, and then the shapes are assembled using the overlapping points between neighboring configurations (Figure 3.3(a)). The first four natural frequencies of the structure are identified as 1.09Hz, 4.75Hz, 10.19Hz, and 13.05Hz. As shown in Figure 3.8, the high spatial resolution offered by MSNs enables extraction of smooth mode shapes. These mode shapes are very close to the results from a high-resolution finite element analysis. Note that in this work, the modal analysis neglects the influence from the mass of the MSNs on the dynamics of the steel frame. Compared with the weight of real-world civil structures, such as steel bridges or wind turbine towers, masse of the MSNs should have much less influence to the structural dynamics.

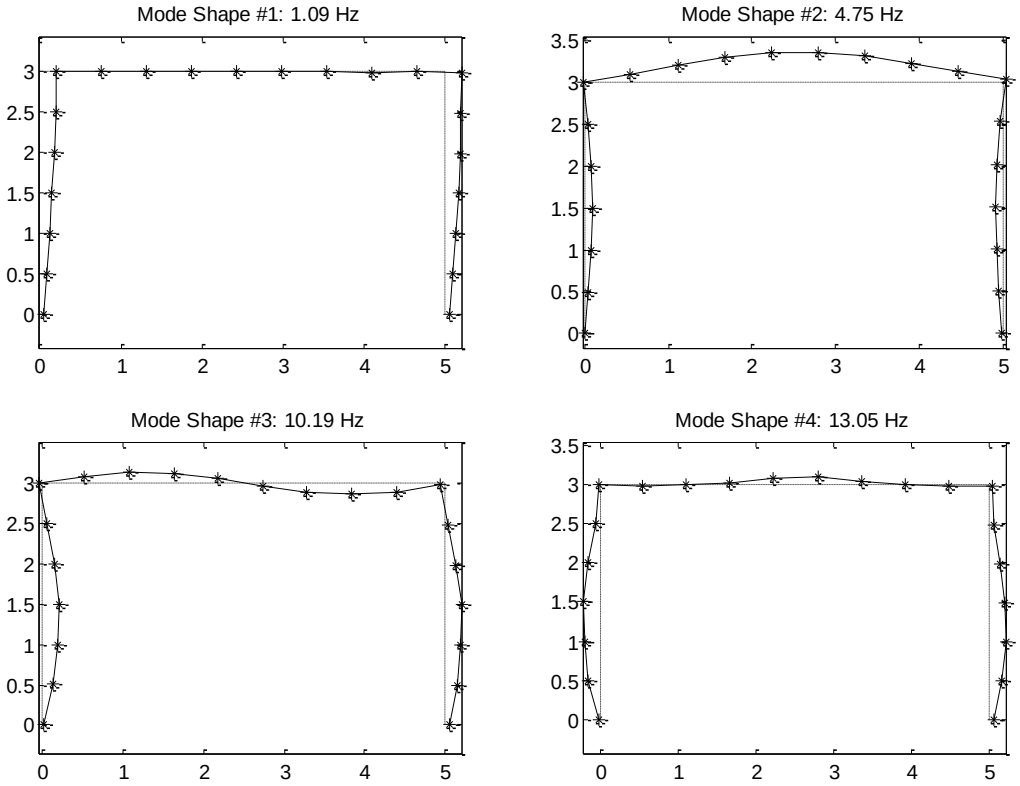

Figure 3.8. First four vibration mode shapes identified using mobile sensor data

3.3 Design of the Flexure-Based MSN

In the first single-car prototype, accelerometers on the MSN cannot be in direct contact with the steel structure for acceleration measurement. Therefore, higher frequency components in the structural vibration cannot be accurately captured for detecting local damage. In order to improve the measurement accuracy, a flexure-based MSN has been developed [75-78]. Figure 3.9 shows the picture of the prototype MSN that consists of three major parts: two 2-wheel cars and a flexible/compliant beam connecting the two cars. Each 2-wheel car contains a body frame, two motors, two 7V lithium batteries, a wireless sensing unit [12], two infrared (IR) sensors, two Hall effect sensors, as well as auxiliary circuits. The compliant connection beam is made of spring steel, with an accelerometer (Silicon Designs 2260-010) mounted in the middle. The

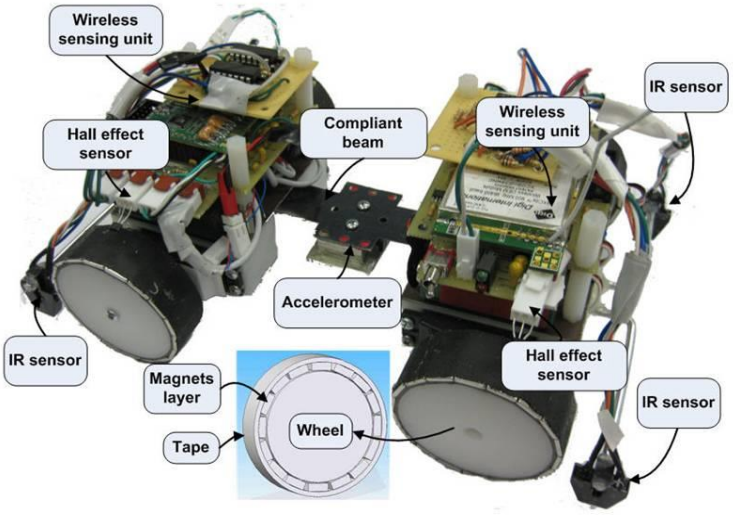

Figure 3.9. Photo of the flexure-based MSN

MSN maneuvers with four motorized wheels, two of which belong to each car. Every wheel is surrounded by thin rectangular magnets (magnetized along the thickness direction) to provide attraction between the wheel and the surface of the underlying ferromagnetic structure. Two 7V lithium batteries are placed on each 2-wheel car, underneath the wireless sensing unit. One battery powers the two motors and the other powers the electronic circuits in the car. Each Hall effect sensor measures the angular velocity of a wheel, while each IR sensor detects the boundary of the underlying structural surface. The width of the MSN is about 0.152m (6 in), and the height is about 0.091m (3.6 in). When the sensor is attached to the structural surface, the length of the MSN is 0.191m (7.5 in). When the sensor is detached, the length of the node is 0.229 m (9 in). The overall weight of the MSN (including two cars) is about 1 kg (2.2 lbs), most of which is contributed by the magnet wheels, motors, and batteries.

Figure 3.10 illustrates the functional diagram of the flexure-based MSN. Each 2-wheel car contains one wireless sensing unit[12], an additional mobility module, and various sensor modules. Same as the design of the single-car MSN, the wireless sensing unit consists of three functional modules: sensor signal digitization, computational core,

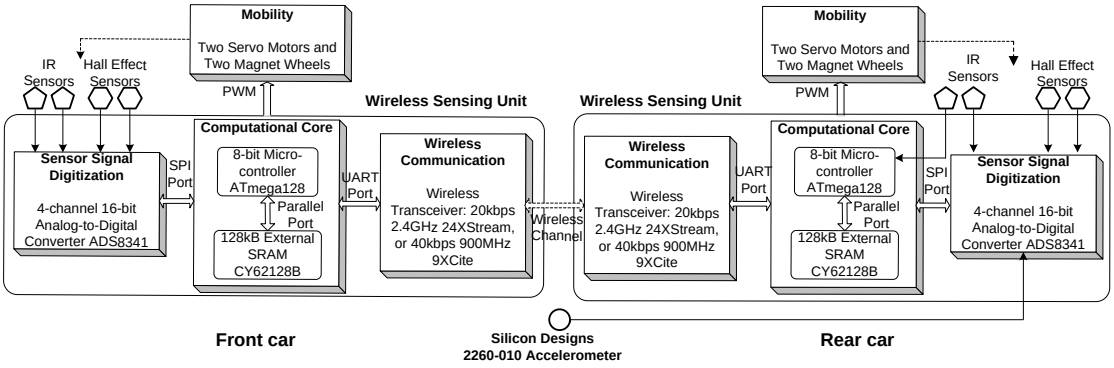

Figure 3.10. Functional diagram of the flexure-based MSN

and wireless communication. The two cars can act independently and collaboratively through wireless communication.

3.3.1 Reliable Mobility

To offer reliable mobility, one important criterion is to make four wheels of the mobile node stay synchronized during movement. In other words, all four wheels should have the same angular velocities during movement, although each wheel is actuated by an individual motor. To accurately orchestrate the wheel angular velocities, real-time feedback control is implemented. A Hall effect sensor, which is capable of measuring the flux of a magnetic field, is placed upon each magnet wheel. In the current prototype, sixteen small-size thin magnets are placed around the wheel with alternating polarities Figure 3.11(a). When the wheel rotates, the alternating polarities cause the magnet flux density measured by the Hall effect sensor to change periodically. Figure 3.11(b) illustrates typical voltage output of the Hall effect sensor when the MSN moves. During each period, two neighboring magnets pass underneath the Hall effect sensor. As a result, the output signal from the Hall effect sensor can be used to estimate the angular velocity of the wheel, so that the velocity data is fed back to the microcontroller in real time for synchronizing the four wheels. The feedback control is conducted through a

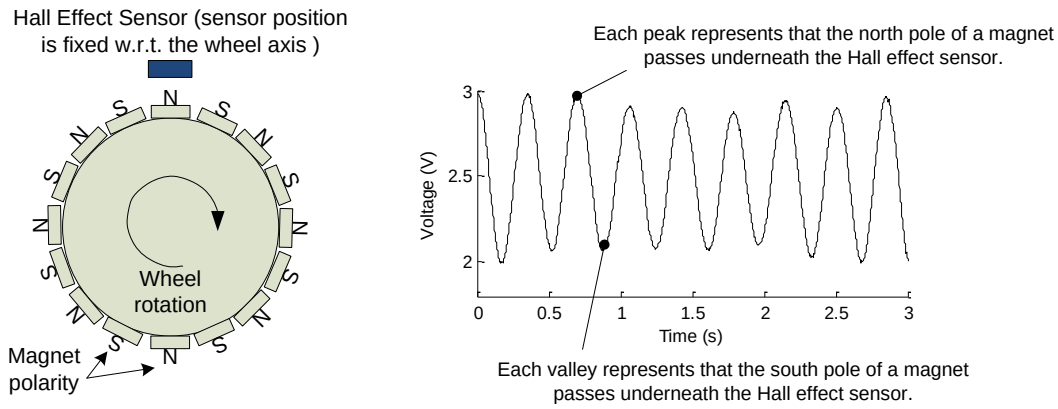

(a) (b)

Figure 3.11. A Hall effect sensor measuring wheel rotation: (a) sensor is placed above a rotating magnet wheel; (b) the output signal of the Hall effect sensor when the magnet wheel rotates

classic proportional–integral–derivative (PID) controller operating at 20Hz sampling rate [79].

To ensure that the MSN moves safely on an underlying structural surface, infrared (IR) sensors are placed at both sides of the front car, as well as both sides of the rear car, for boundary detection. In each IR sensor, an emitting diode emits infrared radiation, and a detection diode detects the radiation reflected from the structural surface. When the sensing node tends to move outside the surface boundary, less IR signal is reflected to the detection diode. To make the MSN stay within the boundaries of the underlying structural surface, both microcontrollers in the mobile node need real-time data from the IR sensors of the front car. For example, when the front car detects that its left wheel is moving out of boundary, the left wheels of both cars are immediately accelerated (or the right wheels of both cars are decelerated) to correct the movement direction. Peer-to-peer communication between the wireless sensing units on the two cars is used for exchanging boundary detection information in real time.

3.3.2 Flexure-Based Design

One distinctive feature of the MSN is the flexure-based design. Different from previous MSN design with one rigid car body, the compliant/flexural beam connecting two car bodies offers advantages for sharp corner negotiation and accurate acceleration measurement by firmly attaching the accelerometer onto the structural surface.

During corner negotiation, if a rigid-body design were adopted with a stiff beam connecting two cars, the distance between front and rear axles has to remain constant. In order to avoid undesired slippage between each wheel and the structural surface, a complicated feedback control scheme would be necessary to precisely control individual wheel speed. On the other hand, using a flexure-based design, the axle distance can change passively and naturally, while the front and rear wheels simply move at a constant speed and do not suffer any slippage. Figure 3.12(a) shows the MSN negotiating over the beam-column corner of a laboratory steel frame, when the front and rear wheels move at the same constant speed.

With the flexure-based design, the MSN can firmly attach the accelerometer onto a structural surface. When acceleration measurement is to be made, the accelerometer can be attached onto the underlying structural surface by bending the center of compliant beam towards the surface (Figure 3.12b); this bending is achieved by commanding the two cars move towards each other. Small-size magnet pieces are arranged around the

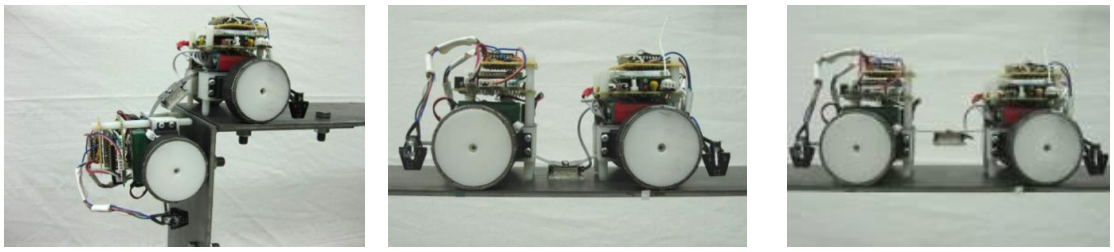

(a) (b) (c)

Figure 3.12. Side view of the magnet-wheeled MSN: (a) transition over a right angle; (b) sensor attachment; (c) sensor detachment

center of the compliant beam, in order to firmly hold down the accelerometer onto the structural surface. The accelerometer can be detached from the surface by straightening the compliant beam after measurement (Figure 3.12c); this straightening is achieved by commanding the two cars to move away from each other. After the accelerometer is detached, the MSN resumes its mobility and can move to next location for another measurement.

3.4 Field Testing of the Flexure-Based MSNs

The testbed bridge (Figure 3.13) for the flexure-based MSNs is located on Georgia Tech campus, connecting the Manufacturing Research Center (MARC) with the Manufacturing Related Disciplines Complex (MRDC). The bridge consists of eleven chord units. Diagonal tension bars are deployed in two vertical side planes and the top horizontal planes, and each floor unit contains a diagonal bracing square tube. Hinge connections are designed at the supports on the MRDC side, and roller connections at the MARC side. Key dimensions of the bridge are listed in TABLE 3.1 [80].

Figure 3.13. Photo of the space frame bridge on Georgia Tech campus

TABLE 3.1. Dimensions of the steel bridge

Dimension		Value
Length		11 × 2.74m = 30.2m (99 ft)
Width		2.13m (7 ft)
Height		2.74m (9 ft)
Concrete floor slab thickness		0.139 m (5.5 in)
Cross section and thickness of square tubes	Top-plane longitudinal	0.152 m × 0.152 m × 0.0080 m (6 in × 6 in × 5/16 in)
	Bottom-plane longitudinal	0.152 m × 0.152 m × 0.0095 m (6 in × 6 in × 3/8 in)
	Others	0.152 m × 0.152 m × 0.0064 m (6 in × 6 in × 1/4 in)

3.4.1 Test Configuration

In the field testing, four flexure-based MSNs are deployed for navigating on the top plane of the frame. It is first verified that each MSN can travel through the bridge span of 30.2m (99 ft) in about five minutes, without stop. Onboard lithium-ion batteries can sustain the MSN operation for about four hours. A total of five measurement configurations are adopted. As shown in Figure 3.14(a), each configuration consists of four measurement locations. Locations at south side of the frame are marked with letter 'S', and locations at north side are marked with letter 'N'. The measurement configurations for the MSNs do not contain locations 4S and 4N, where static wireless sensing nodes are mounted as reference nodes for assembling the mode shapes of the entire bridge. Wirelessly controlled by a laptop server located on the floor level at one side of the bridge (Figure 3.14b), the MSNs start from the inclined members at one side of the bridge, and then move to the 1st measurement configuration (Figure 3.14c). After finishing the measurement at the 1st configuration, the MSNs move to the 2nd configuration, and so on, until they finish measurement at the 5th configuration. At each measurement configuration, each MSN attaches an accelerometer (Silicon Designs 2260-010) onto the structural surface, and measures structural vibrations along the vertical

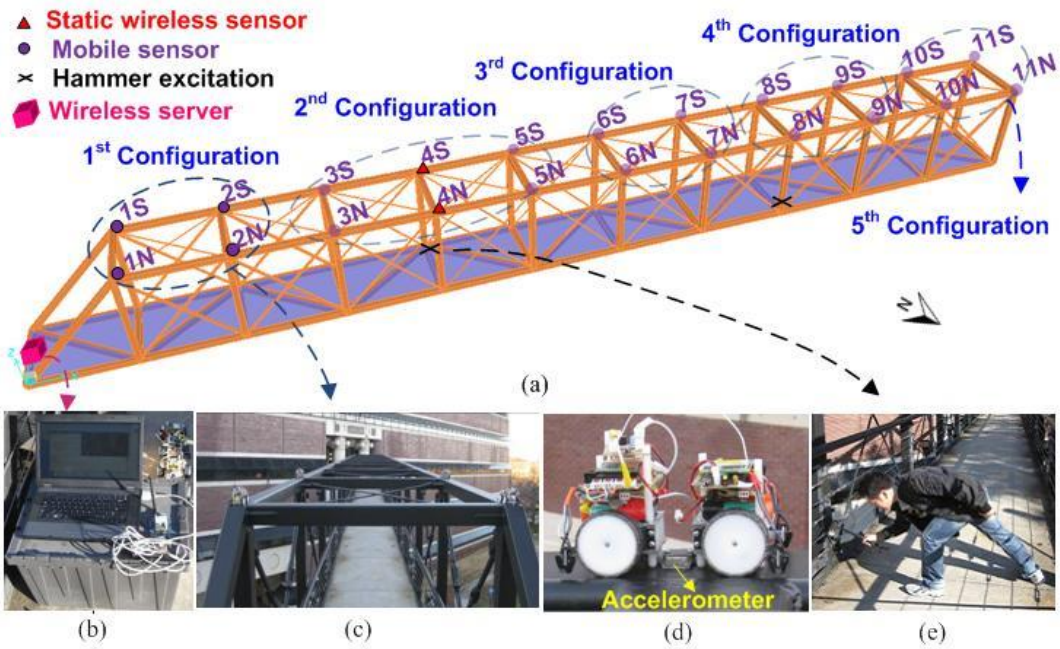

Figure 3.14. Experimental setup for mobile sensor testing: (a) 3D illustration of five measurement configurations for the MSNs; (b) a laptop as the wireless server; (c) four MSNs deployed at the 1st configuration; (d) an MSN attaches an accelerometer onto the structural surface; (e) a hammer impact is being applied

direction (Figure 3.14d). Hammer impact is first applied at the floor below 4S for data collection, and then another impact is applied below 8N (Figure 3.14e). The impact hammer is a 3-lb hammer manufactured by PCB Piezotronics. During testing, each MSN carries a signal conditioning module [81] for filtering and amplifying the accelerometer signal. The cutoff frequency and amplification gain are set to 25Hz and ×20, respectively. Sampling rate is set to 200Hz.

For comparison, another set of instrumentation is conducted entirely with static wireless sensors. Static sensors are installed at the measurement locations on the top plane of the bridge frame (Figure 3.15). Narada wireless sensing units, developed by researchers at the University of Michigan [82-84], are used in the static sensor instrumentation. The reliable performance of the Narada system has been validated in a

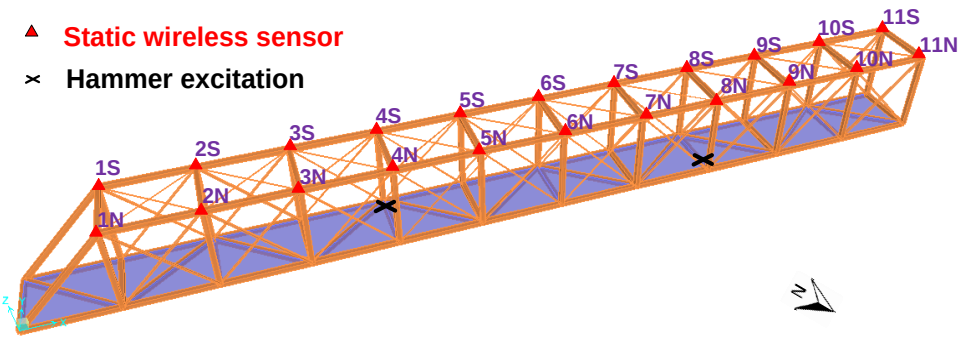

Figure 3.15. Experimental setup for the testing with static wireless sensors

number of previous studies. Modal analysis results using the static sensor data serve as a baseline for the mobile sensor data. The same Silicon Designs 2260-010 accelerometers are used in the static sensor instrumentation for measuring vertical vibrations.

3.4.2 Test Results and Modal Analysis

Figure 3.16 presents example acceleration data recorded by MSNs at locations 7N and 9N, as well as the corresponding frequency spectra when the hammer impact is

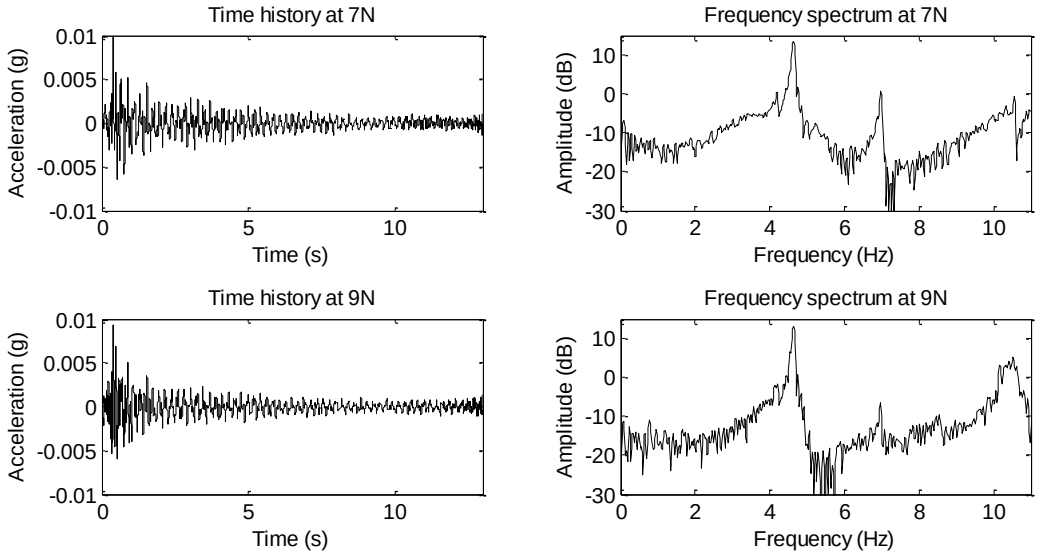

Figure 3.16. Example vibration records and corresponding frequency spectra recorded by mobile sensors when hammer impact is applied on the floor below location 8N

applied on the floor below location 8N. Figure 3.17 presents the acceleration data and frequency spectra recorded by static wireless sensors at the same measurement and hammer impact locations. Similar wave forms are observed between the time history plots in Figure 3.16 and Figure 3.17, for both pairs of measurement locations. Furthermore, similar peaks are observed between frequency spectra of the mobile sensor data and static wireless sensor data. The comparison confirms the reliable quality of the mobile sensor data.

The eigensystem realization algorithm (ERA) [85] is applied to the impulse response functions obtained from mobile sensing data, for extracting modal properties at each configuration. In order to eliminate noise effect, structural vibration data with hammer impact under 4S are used to extract modal properties of configurations 1~2, while data with hammer impact under 8N are used for configurations 3~5. Mode shapes of the entire bridge are then assembled through the reference nodes with two static wireless sensors shown in Figure 3.14(a). Figure 3.18 shows the first three assembled mode shapes. Because the MSNs measure vertical bridge accelerations, only vertical

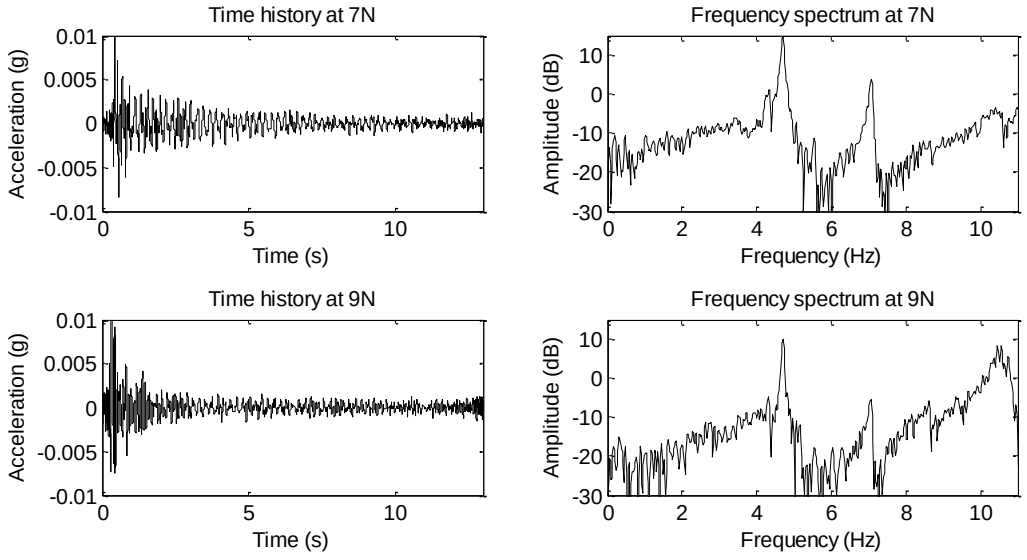

Figure 3.17. Example vibration records and corresponding frequency spectra recorded by static sensors when hammer impact is applied on the floor below location 8N

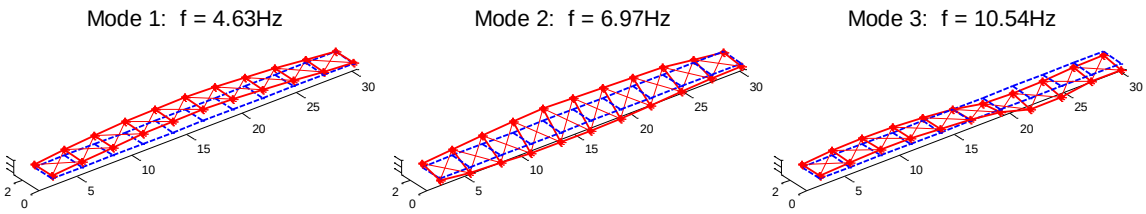

Figure 3.18. First three mode shapes of the bridge extracted from mobile sensing data with hammer impact excitation

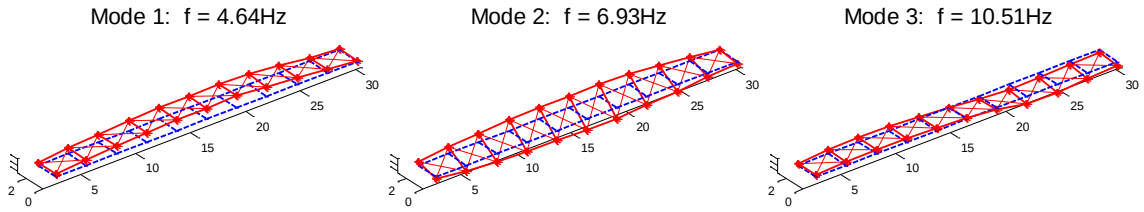

Figure 3.19. First three mode shapes of the bridge extracted from static sensor data with hammer impact excitation

components of each mode shape can be extracted. Similarly, the ERA is also applied to the impulse response functions obtained from static wireless sensor data. Modal properties are extracted and shown in Figure 3.19. Comparison between Figure 3.18 and Figure 3.19 shows that the natural frequencies and mode shapes extracted from mobile sensing data and static wireless sensor data are very close. Therefore, it can be concluded that the four-node mobile sensor network provides adequately high-precision measurement and spatial resolution with very little human effort.

3.4.3 Preliminary Model Updating Using Mobile Sensor Data

A FE model of the bridge is built in OpenSees (Open System for Earthquake Engineering Simulation [86]) platform (Figure 3.20). All steel frame members are modeled as elastic beam-column elements, and steel tension bars on the side and top planes are modeled as 3D truss elements. The concrete slab in this structure is connected with the bottom-plane frame members by sheer studs, through which bending moment

can be transferred. Therefore, for accurate dynamic modeling, the concrete floor slab is modeled as shell elements that share FE nodes with the bottom-plane frame members.

Important parameters of the bridge model are selected for FE model updating (TABLE 3.2). The parameters typically include material properties and support conditions [87, 88]. For support conditions, ideal hinges or rollers are usually used in structural design and analysis, but they do not exist in reality. To describe realistic support conditions, the hinge support at MRDC side is replaced by a rigid link in longitudinal direction, and springs in transverse and vertical directions. Meanwhile, the roller support at MARC side is replaced by springs in transverse and vertical directions (Figure 3.20). Note that each of the material property parameters (e.g. concrete stiffness) applies to structural components spread out on the entire bridge. No spatial variation of

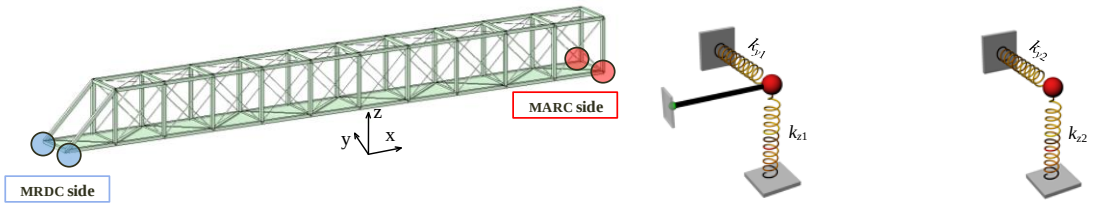

(a) (b) (c)

Figure 3.20. FE model for the steel bridge: (a) 3D view of the bridge model; (b) support condition at MRDC side for model updating; (c) support condition at MARC side for model updating

TABLE 3.2. Selected parameters for model updating

	Updating parameters		Initial value	Optimal value
Concrete slab	Density (kg/m^3)		2.48×10^3	2.58×10^3
	Elastic modulus (N/m^2)		2.07×10^{10}	1.44×10^{10}
Steel	Density (kg/m^3)		7.86×10^3	—
	Elastic modulus (N/m^2)	Frame tubes	2.00×10^{11}	2.00×10^{11}
		Tension bars	2.00×10^{11}	1.87×10^{11}
Support	Transverse k_{y1} (kN/m)		3.50×10^4	2.45×10^4
	Vertical k_{z1} (kN/m)		8.76×10^4	9.81×10^4
	Transverse k_{y2} (kN/m)		3.50×10^4	2.45×10^4
	Vertical k_{z2} (kN/m)		8.76×10^4	9.81×10^4

these parameters at different portions of the bridge is considered in this preliminary work. As a result, changes in these parameters mostly lead to changes in natural frequencies, instead of changes in mode shapes that mainly reflect relative ratios among different portions of the structure. The density of steel members is assumed to be accurately known, thus it is not among the updating variables in the optimization process (the optimal value is marked with "—" in TABLE 3.2).

Due to the insensitivity of bridge mode shapes against the updating parameters listed in TABLE 3.2, only natural frequencies are considered in the optimization objective. The formulation minimizes the difference between the three experimental natural frequencies extracted from mobile sensing data (Figure 3.18) and corresponding frequencies provided by FE model:

$$\text{minimize} \quad \sum_{i=1}^{3} \left(\frac{f_{FE,i} - f_{M,i}}{f_{M,i}} \right)^2 \tag{3.1}$$

where $f_{FE,i}$ denotes the i-th natural frequency provided by the FE model, and $f_{M,i}$ denotes the frequency extracted from mobile sensing data. Note that the weight of each mode is set to be same for simplicity. A nonlinear least-square optimization solver, `'fmincon'` in MATLAB optimization toolbox [89], is adopted to solve the optimization problem. The solver seeks a minimum of the objective function through the interior-point algorithm. The final updated optimal values are shown in TABLE 3.2.

Using the updated parameter values, first five natural frequencies and mode shapes from the FE model are shown in Figure 3.21. For each mode, the left plot is the mode shape of the bridge model in 3D view. The right plot illustrates only the vertical components of the mode shapes at the top-plane nodes, for direct comparison with experimental results. The Z/Y ratio equals the maximum Z-direction component in the mode shape vector divided by the maximum Y-direction component. Mode shapes with large and moderate Z/Y ratios have relatively strong vertical direction components, which

make them easily captured by the single-axis accelerometer used in the MSNs (for measuring vertical vibration). It can be seen that the Vertical-1 mode from the FE model corresponds to Mode-1 extracted from experimental data, the Torsional-1 mode corresponds to Mode-2, and Vertical-2 corresponds to Mode-3. On the contrary, mode shapes with small Z/Y ratios (i.e. Lateral-1 and Lateral-2) have trivial vertical direction components. These two mode shapes are not reliably captured by the MSNs measurements during the modal testing.

TABLE 3.3 shows modal properties extracted from the mobile sensing data, as compared with these from FE model. The largest frequency difference is 8.66% for the initial FE model, and reduces to 4.94% for the updated FE model. The modal assurance criterion (MAC) values are calculated to compare the experimental mode shapes with

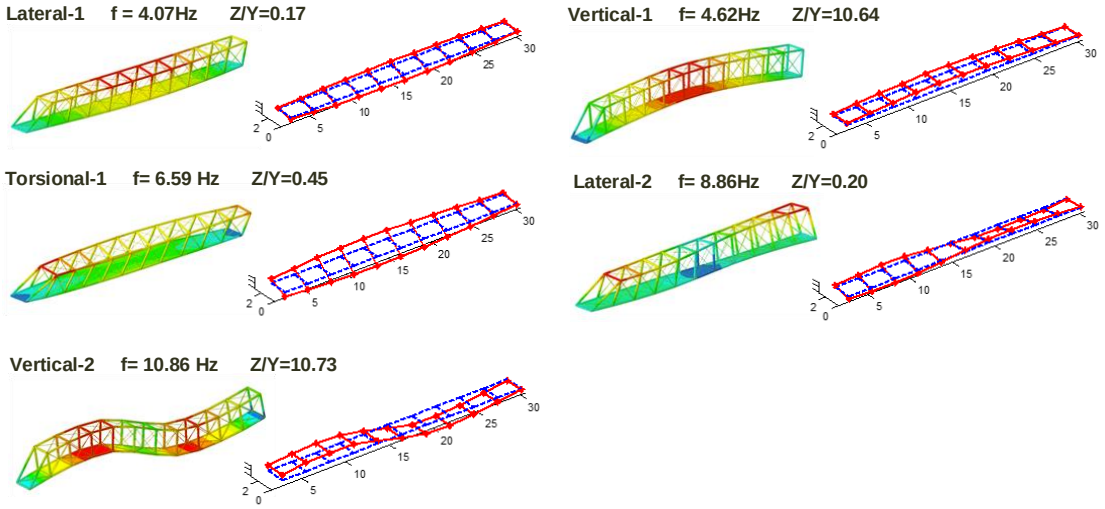

Figure 3.21. First five mode shapes of the FE model

TABLE 3.3. Comparison of modal properties extracted from mobile sensing data and FE model

Mode No.	*Experiment*	*Initial FE Model*			*Updated FE Model*		
	Freq. (Hz)	*Freq. (Hz)*	*Difference*	*MAC value*	*Freq. (Hz)*	*Difference*	*MAC value*
1	4.63	4.85	4.53%	0.99	4.62	0.02%	0.99
2	6.97	6.78	2.17%	0.96	6.59	4.94%	0.97
3	10.53	11.42	8.66%	0.79	10.86	3.35%	0.81

these of both initial and updated FE models. The value is close to 1 for Mode-1 and Mode-2, and the value is 0.81 for Mode-3. Besides, the MAC values are almost the same for the initial and updated FE models, which confirms that mode shapes are not sensitive to the updating parameters. In summary, both the natural frequencies and mode shapes of the updated FE model are fairly close to experimental results from mobile sensor data.

3.5 Summary

In this study, two MSN prototypes are developed for SHM purpose. The first generation adopts a single-car design, and accelerometers are fixed on the car body. As a result, the accelerometers cannot be attached to structural surface for direct measurement of structural vibration. A mobile sensor network containing four single-car MSNs is validated through laboratory experiment on a steel portal frame, and its modal properties are successfully extracted though mobile sensor data.

The second generation improves the sensing accuracy by adopting a flexure-based design, so that the accelerometer can be firmly attached to structural surface during measurement. More complicated control scheme is considered to ensure that the flexure-based MSN can maneuver on structural surface reliably. The flexure-based MSNs are validated through a field experiment on a space frame bridge. A four-node mobile sensor network is employed to navigate on the top plane of the bridge and measure structural vibrations with high spatial resolution. Using data collected by four MSNs, detailed modal properties of the bridge are identified and validated with reference static sensors. An FE model for the bridge is built according to the structural drawings and updated based on the modal properties extracted from the mobile sensing data. The updated FE model provides modal properties that are close to these extracted from mobile sensing data.

CHAPTER 4 DECENTRALIZED STRUCTURAL DAMAGE DETECTION USING MOBILE SENSOR DATA THROUGH TRANSMISSIBILITY ANALYSIS

To further validate the mobile sensing system, transmissibility analysis is applied on mobile sensing data for structural damage detection. Transmissibility function analysis attracts considerable interest due to its effectiveness in damage identification, and independency to the magnitude and waveform of the excitation records. Based on these features, a decentralized structural damage detection procedure is proposed herein for the mobile sensing nodes (MSNs). The decentralized procedure only requires measurements in one small neighborhood at a time, and thus, is ideal for adoption by a small group of MSNs that take measurements in one area at a time and automatically scan through a structure. Laboratory experiments are conducted on a steel portal frame where various simulated structure damage scenarios are introduced. Besides experiments with MSNs, this study also investigates the nature of transmissibility functions for damage detection in an analytical manner based on a general multi-DOF spring-mass-damper system. The analytical derivation is validated through numerical simulation and laboratory experiments using MSNs. Note that the MSN adopted in this chapter is the flexure-based MSN presented in Section 3.3.

This chapter is organized as follows. Section 4.1 introduces basic formulation of transmissibility function analysis. Section 4.2 describes decentralized damage detection using mobile sensor data. Section 4.3 presents analytical studies on damage sensitivity of the decentralized transmissibility functions on a multi-DOF spring-mass-damper system. Section 4.4 describes the simulation and experiment validation of the analytical analysis. Section 4.5 summarizes the study in this chapter.

4.1 Introduction to Transmissibility Function Analysis

The equations of motion for an n-degree-of-freedom (n-DOF) linear structure can be formulated as:

$$\mathbf{M}\ddot{\mathbf{x}}(t) + \mathbf{C}\dot{\mathbf{x}}(t) + \mathbf{K}\mathbf{x}(t) = \mathbf{f}(t) \tag{4.1}$$

where $\mathbf{x}(t)$ is the $n \times 1$ displacement vector, $\mathbf{M}$ is the $n \times n$ mass matrix, $\mathbf{C}$ is the $n \times n$ viscous damping matrix, $\mathbf{K}$ is the $n \times n$ stiffness matrix, and $\mathbf{f}(t)$ is the $n \times 1$ excitation force vector. If the excitation force is only applied to the k-th DOF, then $\mathbf{f}(t)$ has only one non-zero entry:

$$\mathbf{f}(t) = \left\{0_1, \cdots, f_k(t), \cdots, 0_n\right\}^{\mathrm{T}} \tag{4.2}$$

Applying Laplace transform (assuming the structure is initially at rest), Equation (4.1) can be represented in frequency domain with complex argument s as:

$$\mathbf{X}(s) = \mathbf{H}(s)\mathbf{F}(s) \tag{4.3}$$

where $\mathbf{H}(s) = \left(\mathbf{K} + s^2\mathbf{M} + s\mathbf{C}\right)^{-1}$ is the $n \times n$ frequency response function (FRF) matrix. Assuming the excitation force is only applied to the k-th DOF, the excitation force vector in frequency domain is determined as:

$$\mathbf{F}(s) = \left\{0_1, \cdots, F_k(s), \cdots, 0_n\right\}^{\mathrm{T}} \tag{4.4}$$

The acceleration vector in the frequency domain can be formulated as:

$$\mathbf{A}(s) = s^2\mathbf{H}(s)\mathbf{F}(s) \tag{4.5}$$

The transmissibility function $T_{ij}(s)$ between the output DOF i and reference-output DOF j is defined as the ratio between two frequency spectra $A_i(s)$ and $A_j(s)$. Letting $\mathbf{h}_i(s)$ be the i-th row of $\mathbf{H}(s)$ and $\mathbf{h}_j(s)$ be the j-th row, the transmissibility function $T_{ij}(s)$ can be calculated as:

$$T_{ij}(s) = \frac{A_i(s)}{A_j(s)} = \frac{-\omega^2\mathbf{h}_i(s)\mathbf{F}(s)}{-\omega^2\mathbf{h}_j(s)\mathbf{F}(s)} = \frac{\mathbf{h}_i(s)\mathbf{F}(s)}{\mathbf{h}_j(s)\mathbf{F}(s)} \tag{4.6}$$

If the excitation force is only applied to the k-th DOF, as shown in Equation (4.2), $T_{ij}(s)$ is further simplified by substituting Equation (4.4) into Equation (4.6):

$$T_{ij}(s) = \frac{H_{ik}(s)}{H_{jk}(s)} \tag{4.7}$$

where $H_{ik}(s)$, $H_{jk}(s)$ are entries of the FRF matrix. Therefore, the transmissibility function is determined by the inherent structural property, and can be independent from the magnitude and waveform of the excitation force $f_k(t)$. In addition, for calculating the transmissibility function $T_{ij}(s)$, only the acceleration measurements at DOF *i* and DOF *j* are needed to perform the division between two frequency spectra (Equation (4.7)). In other words, during practical implementation, the excitation force measurement is not required for determining $T_{ij}(s)$. This independency from excitation magnitude and waveform provides great convenience in practice.

Based upon the transmissibility function $T_{ij}(s)$, where the Laplace variable s = jω and j is the imaginary unit, an integral damage indicator (*DI*) between the DOF *i* and DOF *j* is defined as:

$$DI_{ij} = \frac{\int_{\omega_1}^{\omega_2} \left| \ln \left| T_{ij}^{U}(s) \right| - \ln \left| T_{ij}^{D}(s) \right| \right| d\omega}{\int_{\omega_1}^{\omega_2} \left| \ln \left| T_{ij}^{U}(s) \right| \right| d\omega} \tag{4.8}$$

where superscript *U* and *D* represent the undamaged structure and the damaged structure, respectively. Accordingly, T_{ij}^{U} and T_{ij}^{D} represent the transmissibility function of the undamaged structure and the damaged structure, respectively; ω_1 and ω_2 are the lower and upper boundaries of the frequency span of interest; If the damage indicators between two DOFs are large, it is likely that structural damage has occurred near these two DOFs.

In order to reduce the effect of practical uncertainties, such as sensor noise and location uncertainty, the measurement at each configuration is usually repeated for multiple times, with either the undamaged or the damaged structure. If there are *N* repeating measurements, the averaged transmissibility functions are calculated for computing the damage indicator:

$$T_{ij}^{U} = \frac{1}{N}\sum_{k=1}^{N}(T_{ij}^{U})_k \qquad T_{ij}^{D} = \frac{1}{N}\sum_{k=1}^{N}(T_{ij}^{D})_k \tag{4.9}$$

where the subscript *k* represents the *k*-th repeating test.

To validate the algorithm, an experimental repeatability check can be performed to ensure that experimental uncertainties, including sensor noise and the application of external excitation, have negligible influence to the damage detection results. Again, for either an undamaged or a damaged structure, assume that the experiment is repeated for *N* times at each pair of DOFs. The *N* data sets are then separated into two groups of *N*/2 data sets. The separation can be simply made according to the sequence numbers of each data set, e.g. data sets with odd sequence numbers constitute one group, and data sets with even sequence numbers constitute another group. Taking the undamaged structure as an example, the averaged transmissibility function of each data group is calculated as:

$$T_{ij}^{U\_odd} = \frac{2}{N}\sum_{k=1}^{N/2}(T_{ij}^{U})_{2k-1} \qquad T_{ij}^{U\_even} = \frac{2}{N}\sum_{k=1}^{N/2}(T_{ij}^{U})_{2k} \tag{4.10}$$

The repeatability indicator (*RI*) is then defined in a similar form to the damage indicator. From the experiments with the undamaged structure, the repeatability indicator of the DOF pair *i* and *j* is defined as:

$$RI_{ij}^{U} = \frac{\int_{\omega_1}^{\omega_2}\left|\ln\left|T_{ij}^{U\_odd}\right| - \ln\left|T_{ij}^{U\_even}\right|\right| d\omega}{\int_{\omega_1}^{\omega_2}\left|\ln\left|T_{ij}^{U\_odd}\right|\right| d\omega} \tag{4.11}$$

As a result, a smaller repeatability indicator *RI* represents a higher level of repeatability. This is noted because in contrary, a larger damage indicator *DI* (Equation (4.8)) indicates a higher level of damage. Similar to *RI* for undamaged structure, from the experiments with the damaged structure, the averaged transmissibility functions of two data groups can be calculated as $T_{ij}^{D\_odd}$ and $T_{ij}^{D\_even}$. The repeatability indicator from experiments with the damaged structure, RI_{ij}^{D}, can be calculated likewise.

4.2 Decentralized Damage Detection Using Mobile Sensor Data

Laboratory experiments on a steel portal frame are conducted to validate the performance of MSNs for damage detection. In the experiments, a decentralized structural damage detection procedure is designed for a mobile sensor network containing two MSNs [77, 90]. This section first describes the laboratory structure and the dynamic testing scheme. Transmissibility function analysis is first conducted to the undamaged structure. Next, three damage scenarios are investigated: the first scenario emulated with an extra mass block, the second scenario with loosened bolts, and the third scenario with loss of section area. Damage detection and localization are conducted for each scenario.

4.2.1 Experimental Setup

The 2D laboratory steel portal frame described in Section 3.2.1 is adopted for investigating structural damage detection using mobile sensing nodes (Figure 4.1a). For the undamaged structure, the torque of all bolts for connecting the beam and columns is originally set at 13.56Nm (120 lbs-in).

Three acceleration measurement locations are assigned on the left column (A1 to

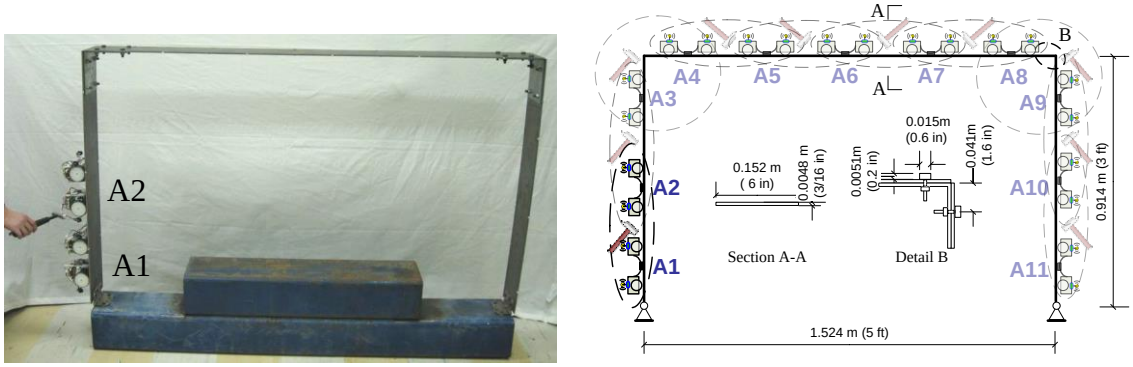

(a) (b)

Figure 4.1. Laboratory steel portal frame for damage detection using mobile sensing nodes: (a) photo of the portal frame with two mobile nodes at locations A1 and A2; (b) schematic of sensor and impact locations, where undimmed area shows hammer impact being applied between A1 and A2

A3) and three on the right columns (A9 to A11), respectively. Five acceleration measurement locations (A4 to A8) are uniformly assigned on the beam (Figure 4.1b). Two mobile sensing nodes are used in the experiments. Each mobile sensing node carries a Silicon Designs 2260-010 accelerometer that has a nominal bandwidth of 0 ~ 1000Hz. On the structure, the two mobile sensing nodes move to each of the ten location pairs (e.g. A1-A2, A2-A3, …, A10-A11) to take acceleration measurements. When the two mobile sensing nodes arrive at one pair of measurement locations, the accelerometer is attached onto the structural surface; then a hammer impact is applied at the middle of these two adjacent measurement locations. The acceleration measurement direction is perpendicular to the beam or column surface where the accelerometer is attached. The sampling rate for the acceleration measurement is set to 2,500 Hz. Time synchronization between two mobile nodes is achieved through a wireless beacon broadcasted by the server. The synchronization accuracy is about 20μs at the beginning of the measurement [12].

Figure 4.2(a) plots the acceleration data at location A1 and Figure 4.2(b) plots the acceleration data at location A2; both data sets are simultaneously collected when an impact hammer hits between A1 and A2. Figure 4.3 shows the magnitude of the two frequency spectra, i.e. the discrete Fourier transform (DFT) results of the acceleration time history. Eight-times zero padding is performed to the time history, in order to

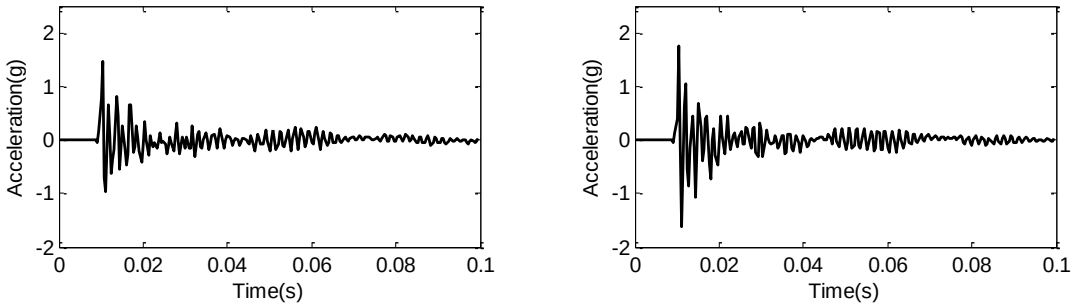

(a) (b)

Figure 4.2. Acceleration data recorded by mobile sensing nodes: (a) location A1; (b) location A2. Hammer impact is applied between A1 and A2 (as shown in Figure 4.1b)

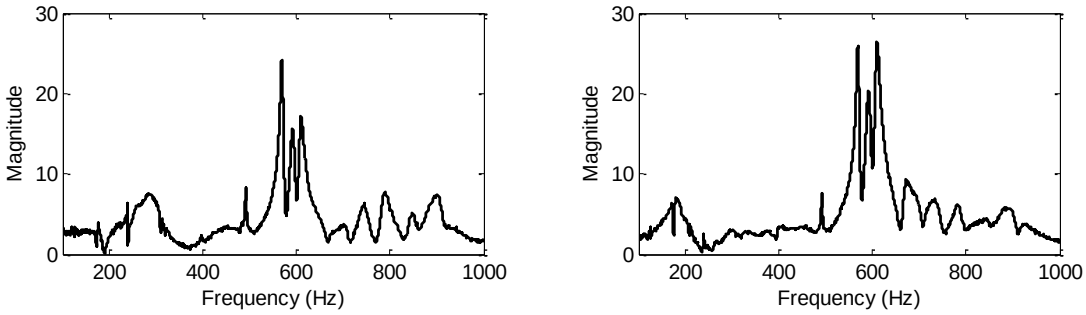

Figure 4.3. Frequency spectra of the mobile sensing data in Figure 4.2: (a) location A1; (b) location A2

achieve a frequency resolution of 0.125 Hz in the spectra. The 0 ~ 100 Hz range of the frequency spectra contains many low valleys that are susceptible to sensor noise. According to the definition, transmissibility function is calculated by the ratio between the two frequency spectra (Equation (4.6)). If small numerical values exist near the valleys of the denominator spectrum, the division process results in random peaks in the calculated transmissibility function. These random peaks, in turn, cause the damage indicators to be unreliable. To reduce sensor noise effect, the 0 ~ 100 Hz range of the frequency spectra is not used for calculating the transmissibility function. Instead, the 100 ~ 1,000 Hz frequency range is used, i.e. ω_1 is set to 100 Hz and ω_2 is set to 1,000 Hz in Equation (4.8).

In order to reduce the effect of experimental uncertainties, hammer impact experiments for each location pair are repeatedly conducted for 20 times, i.e. $N = 20$ in Equation (4.9). The repeatability of the experiments is verified by comparing among the 20 data sets collected from the undamaged structure. The 20 acceleration data sets collected for each pair of locations are separated into two groups of 10 data sets. The separation is simply made according to the sequence numbers of each data set, i.e. data sets with odd sequence numbers constitute one group, and data sets with even sequence numbers constitute another group. Following Equation (4.10), $T_{ij}^{U\_odd}$ and $T_{ij}^{U\_even}$ are calculated for $i = 1, \ldots 10$ and $j = i + 1$. The magnitude results are plotted in Figure 4.4.

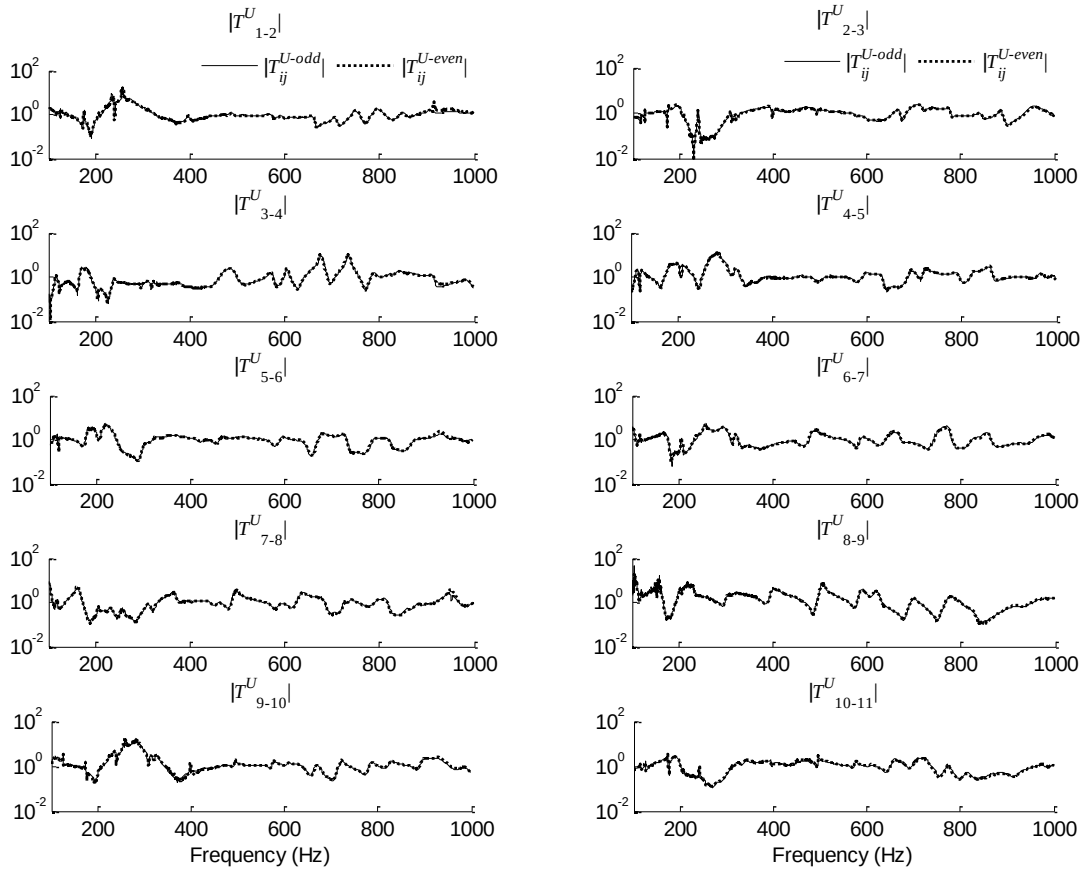

Figure 4.4. Repeatability of transmissibility functions among data sets for undamaged structure

Due to the random nature of laboratory experiments, minor differences exist between the transmissibility functions calculated from the two groups of data sets. Nevertheless, the $T_{ij}^{U\_odd}$ plots generally match closely with the $T_{ij}^{U\_even}$ plots for all location pairs, which demonstrate reasonable repeatability of the experiments.

4.2.2 Damage Scenario I –Mass Change

Similar to stiffness loss, mass change causes variations in vibration modal properties of the structure. Such variations are to be detected through instrumentation and analysis. Thus, for convenience, researchers often start experimental validation of a damage detection technique with reversible mass change. In Damage Scenario I, a steel

mass block of 0.575 kg (1.27 lbs) is bonded to the left column for emulating a reversible damage. In contrast, the mass of the left column is 4.985 kg (10.99 lbs). The bonding location is at 0.229 m (9 in) above the column base, which is between locations A1 and A2 (Figure 4.5). With the mass block bonded at this position, the two mobile sensing nodes sequentially conduct measurements at location pairs A1-A2, A2-A3, and so on. Same as the measurement scheme for the undamaged structure, at each location pair, the hammer impact experiments are repeated for 20 times. The experimental repeatability is verified by separating the 20 data sets at each location pair into an odd-sequence group and an even-sequence group, so that $T_{ij}^{D\_odd}$ and $T_{ij}^{D\_even}$ are calculated. For each location pair, the results demonstrate similar agreement as shown in the repeatability check for the undamaged structure, i.e. the $T_{ij}^{U\_odd}$ and $T_{ij}^{U\_even}$ plots in Figure 4.4.

With all the experimental data sets for both the undamaged and damaged structures, according to Equation (4.9), the averaged transmissibility functions T_{ij}^{U} and T_{ij}^{D} are computed for $i = 1, \ldots 10$ and $j = i + 1$. Figure 4.6 presents the magnitude of the averaged transmissibility functions of both the undamaged structure and the damaged structure (i.e. with the extra mass block). It is shown that the extra mass block changes the amplitude and peak frequencies of the transmissibility functions. In particular, larger

Figure 4.5. Damage Scenario I – an extra mass block and two mobile sensing nodes, one node allocated at location A1, and the other node at A2 (locations A1 and A2 are as shown in Figure 4.1b)

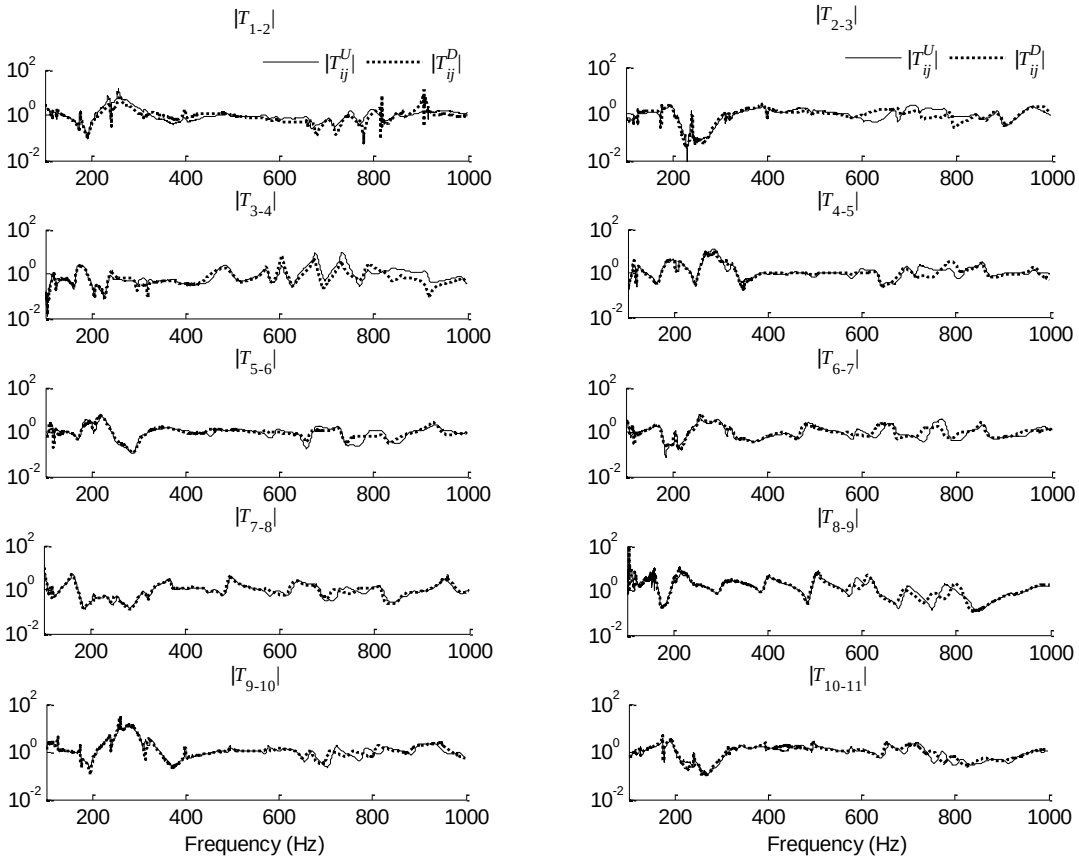

Figure 4.6. Damage Scenario I – comparison of transmissibility functions between data sets of the undamaged and damaged structures

difference in the transmissibility functions (e.g. $T_{1\text{-}2}$ and $T_{2\text{-}3}$) is observed for location pairs close to the damage location, i.e. the mass block position between A1 and A2. Transmissibility functions (e.g. $T_{8\text{-}9}$ and $T_{9\text{-}10}$) at locations far away from the damage generally demonstrate very little change between the undamaged and damaged structures. Furthermore, the comparison between Figure 4.4 and Figure 4.6 shows that difference among $T_{ij}^{U\_odd}$ and $T_{ij}^{U\_even}$ (in Figure 4.4) is much less than the difference between T_{ij}^{U} and T_{ij}^{D} (Figure 4.6). This again confirms that the experimental uncertainties are within an acceptable level.

Based upon the averaged transmissibility functions T_{ij}^{U} and T_{ij}^{D}, damage indicators are calculated following Equation (4.8). The damage indicators basically measure the level of difference between the averaged transmissibility functions of the

undamaged structure and of the damaged structure, at each location pair. As presented in Figure 4.7, the largest damage indicator is $DI_{1\text{-}2}$ = 0.73, which agrees with the correct damage location. In general, lower damage indicators are observed for location pairs far away from the damage location. Following Equation (4.11), repeatability indicators are also calculated for the experiments with the undamaged structure, as well as the experiments with the damaged structure. Again, note that a smaller repeatability indicator *RI* represents a higher level of repeatability. Figure 4.7 shows that among all the pairs of measurement locations, the largest repeatability indicator for the data sets of the undamaged structure is RI^{U}_{1-2} = 0.12. Among all the pairs of measurement locations, the largest repeatability indicator for the damaged structure is RI^{D}_{5-6} = 0.14. Compared with the damage indicators *DI*, the small values of repeatability indicators RI^{U} and RI^{D} demonstrate that the experimental results are repeatable, and the experimental uncertainties have limited effects on the damage detection.

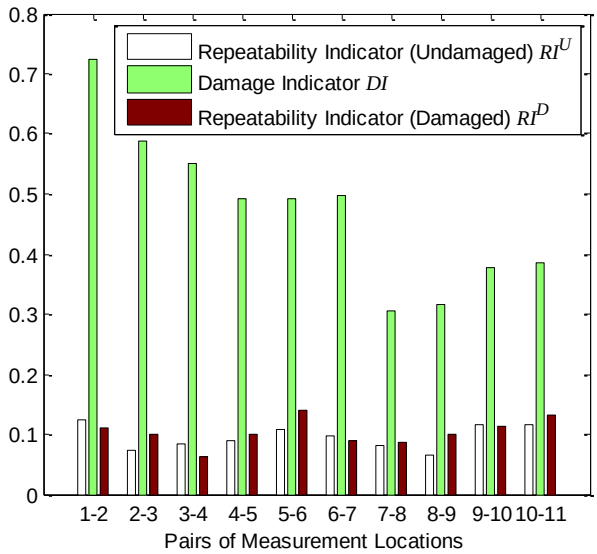

Figure 4.7. Damage Scenario I – the damage indicators and repeatability indicators for ten pairs of measurement locations

4.2.3 Damage Scenario II – Loosened Bolts

In Damage Scenario II, four bolts at the upper left corner of the steel frame are loosened (Figure 4.8). The bolts connect the left end of the beam with the angle plate, which is between locations A3 and A4. The torque of every bolt is reduced from 13.56N-m (120 lbs-in) to 0.565N-m (5lbs-in).

At each location pair, the hammer impact experiments are again repeated for 20 times. Figure 4.9 compares the magnitude of the averaged transmissibility functions between the undamaged structure and the damaged structure. The transmissibility function at location pair A3-A4 ($T_{3\text{-}4}$) shows the largest difference between the damaged and undamaged structures, which corresponds to the correct damage location. Figure 4.10 shows the damage indicators as well as repeatability indicators of both undamaged and damaged structures. The largest damage indicator is $DI_{3\text{-}4}$ = 0.56, and the location pair A3-A4 is the correct damage location where bolts are loosened. In general, lower damage indicators are observed for location pairs far away from the damage location. In addition, all repeatability indicators of the experiments for the undamaged and damaged structures are close to 0.1. These small repeatability indicators again verify that the experimental uncertainties have limited effects on damage detection.

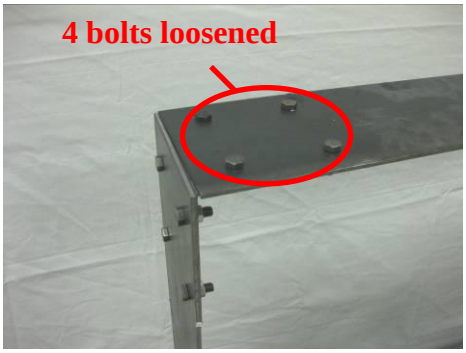

Figure 4.8. Damage Scenario II – the torque of each of the four bolts is reduced from 13.56Nm (120 lbs-in) to 0.565Nm (5lbs-in). The bolts are between locations A3 and A4 shown in Figure 4.1(b)

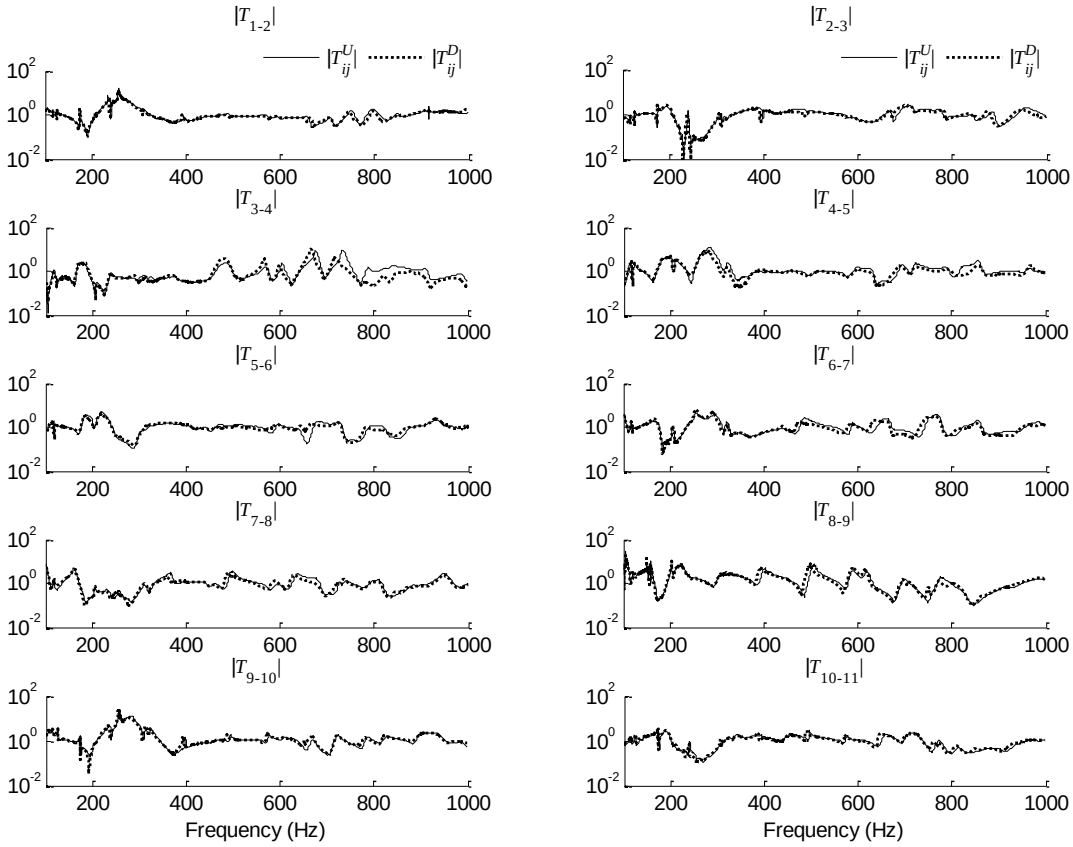

Figure 4.9. Damage Scenario II – comparison of transmissibility functions between data sets of the undamaged and damaged structures

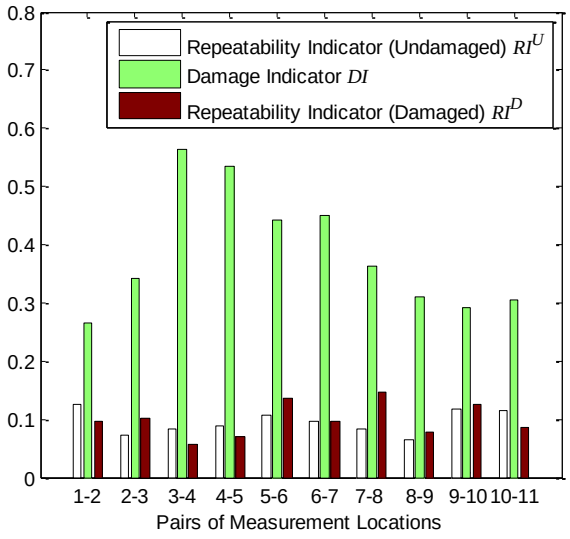

Figure 4.10. Damage Scenario II – the damage indicators and repeatability indicators for ten pairs of measurement locations

4.2.4 Damage Scenario III – Section Loss

In Damage Scenario III, reduction in section area is introduced to the left column (Figure 4.11). The width of the section loss is 0.006 m (0.25 in), and the total length of the loss is 0.0075 + 0.0075 = 0.015 m (0.6 in), about one tenth of the column width. The location of the section loss is at 0.533 m (21 in) above the column base, which is between locations A2 and A3. The two mobile sensing nodes again sequentially take measurement at every pair of locations (A1-A2, A2-A3, …, A10-A11), and measurement at each location pair is repeatedly taken for 20 times.

Figure 4.12 compares the magnitude of the averaged transmissibility functions of the undamaged structure and the damaged structure. The transmissibility function at location pair A2-A3 ($T_{2\text{-}3}$) shows the largest difference between the damaged and undamaged structures, which corresponds to the correct damage location. The damage indicators and repeatability indicators for Damage Scenario III are shown in Figure 4.13. The largest damage indicator is $DI_{2\text{-}3}$ = 0.49, and the location pair A2 and A3 is the correct damage location where the notches are introduced. In general, lower damage indicators are observed for location pairs far away from the damage location. In addition, the small repeatability indicators shown in Figure 4.13 again demonstrate that experimental uncertainties have limited effects on damage detection.

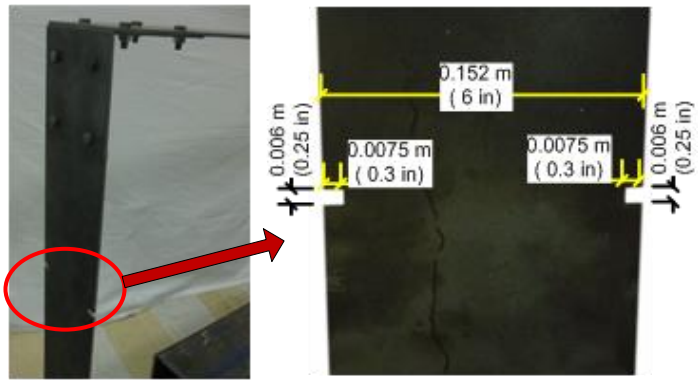

Figure 4.11. Damage Scenario III – loss in section area is introduced to the left column between locations A2 and A3 shown in Figure 4.1(b)

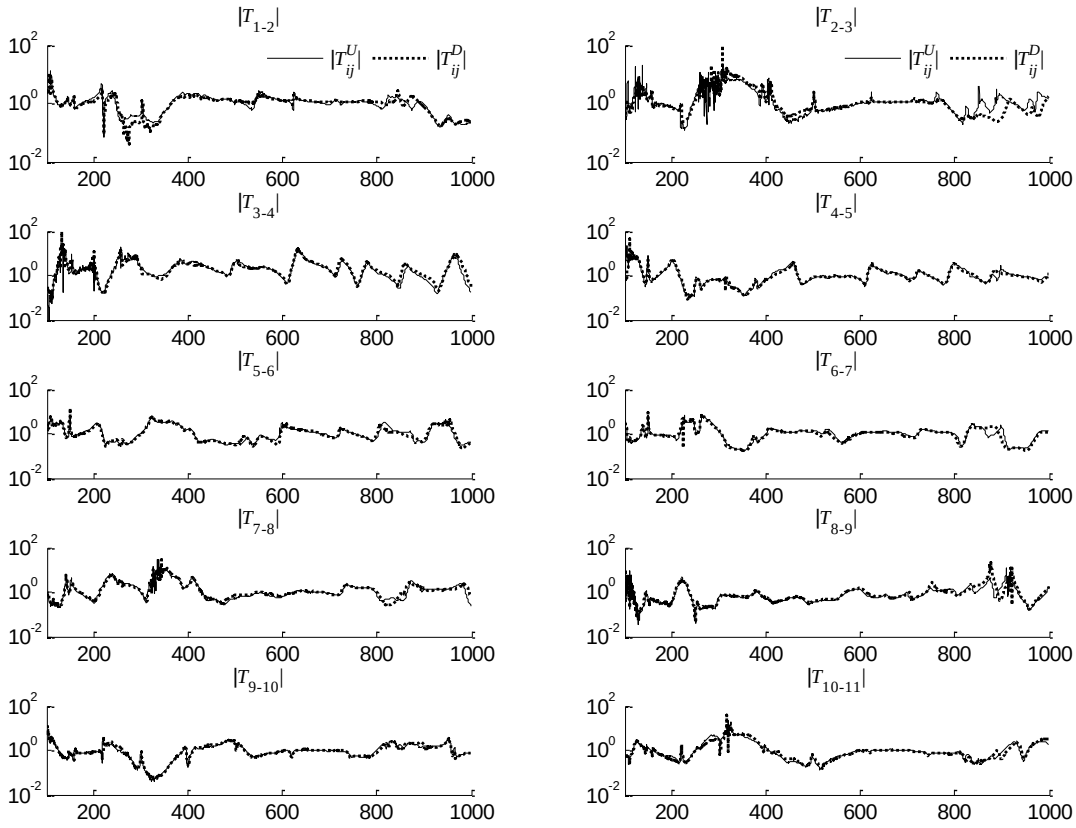

Figure 4.12. Damage Scenario III – comparison of transmissibility functions between data sets of the undamaged and damaged structures

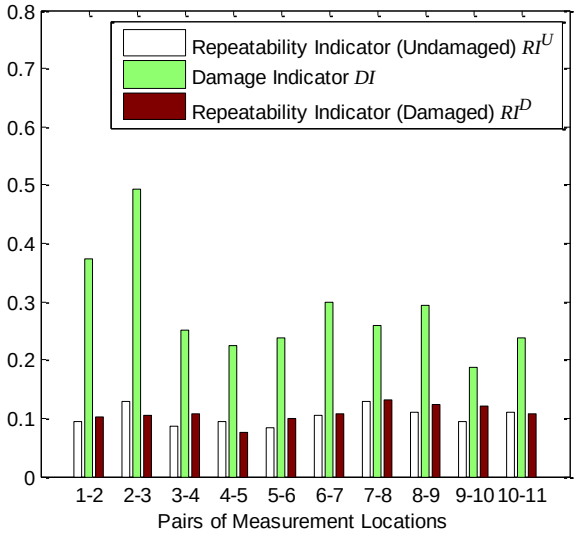

Figure 4.13. Damage Scenario III – the damage indicators and repeatability indicators for ten pairs of measurement locations

4.3 Damage Sensitivity Study of Decentralized Transmissibility Functions

Although transmissibility functions have been validated by many experimental studies, little research has been devoted to analytically investigating its performance for damage detection. This section explores the performance nature of transmissibility functions for damage detection in an analytical manner. The analysis is performed with a general multi-DOF spring-mass-damper system [91].

4.3.1 Transmissibility Function for A Multi-DOF Spring-Mass-Damper System

For a multi-DOF spring-mass-damper system (Figure 4.14), the structural matrices can be formulated as:

$$\mathbf{M} = \mathrm{Diag}\left\{m_1, m_2, \cdots, m_N\right\} \tag{4.12}$$

$$\mathbf{K} = \begin{bmatrix} k_1+k_2 & -k_2 & 0 & 0 & \cdots & 0 \\ & k_2+k_3 & -k_3 & 0 & \cdots & 0 \\ & & \ddots & \ddots & \ddots & \vdots \\ & & & k_{N-2}+k_{N-1} & -k_{N-1} & 0 \\ & \text{Symm.} & & & k_{N-1}+k_N & -k_N \\ & & & & & k_N+k_{N+1} \end{bmatrix} \tag{4.13}$$

$$\mathbf{C} = \begin{bmatrix} c_1+c_2 & -c_2 & 0 & 0 & \cdots & 0 \\ & c_2+c_3 & -c_3 & 0 & \cdots & 0 \\ & & \ddots & \ddots & \ddots & \vdots \\ & & & c_{N-2}+c_{N-1} & -c_{N-1} & 0 \\ & \text{Symm.} & & & c_{N-1}+c_N & -c_N \\ & & & & & c_N+c_{N+1} \end{bmatrix} \tag{4.14}$$

Here "Diag" denotes a diagonal matrix, and "Sym." denotes the symmetric part.

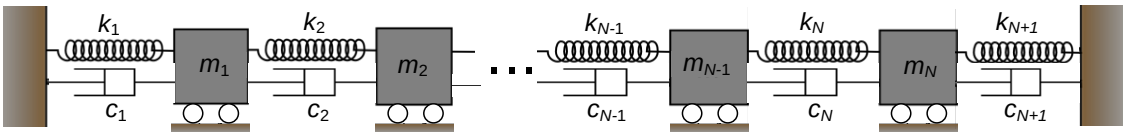

Figure 4.14. A multi-DOF spring-mass-damper system

Following the general equations for linear dynamic systems (Equations (4.1)~(4.7)), the transmissibility function $T_{ij}(s)$ for only one external excitation $f_k(t)$, applied to the k-th DOF (Equation (4.7)), will be analytically derived herein. To start, it is well known that the transfer matrix **H**(s) is equal to the inverse of matrix **B**(s), where

$$\mathbf{B}(s) = s^2\mathbf{M} + s\mathbf{C} + \mathbf{K} = \begin{bmatrix} m_1s^2+(c_1+c_2)s+k_1+k_2 & -c_2s-k_2 & 0 & \cdots & 0 \\ & m_2s^2+(c_2+c_3)s+k_2+k_3 & -c_3s-k_3 & \cdots & 0 \\ & & \ddots & \ddots & \vdots \\ & \text{Symm.} & & \ddots & -c_Ns-k_N \\ & & & & m_Ns^2+(c_N+c_{N+1})s+k_N+k_{N+1} \end{bmatrix} \tag{4.15}$$

Note that matrix **B** is a symmetric tridiagonal matrix. As a result, according to [92], the entries of **H**(s) can be expressed in a recursive form, where "(s)" is neglected to lighten the notation:

$$H_{ij} = \begin{cases} U_i \cdots U_{j-1} H_{jj} & i < j \\ H_{ji} & i > j \\ [B_{ii} - X_i - Y_i]^{-1} & i = j \end{cases} \tag{4.16}$$

where the intermediate variables U_i, X_i, Y_i are recursively computed based on entries in matrix **B(*s*)**:

$$\begin{aligned} U_i &= -[B_{ii} - Y_i]^{-1} B_{i(i+1)} && (i = 1, \cdots, N-1) \\ Y_i &= \begin{cases} 0 & (i = 1) \\ B_{i(i-1)}^2 \, [B_{(i-1)(i-1)} - Y_{i-1}]^{-1} & (i = 2, \cdots, N) \end{cases} \\ X_i &= \begin{cases} 0 & (i = N) \\ B_{i(i+1)}^2 \, [B_{(i+1)(i+1)} - X_{i+1}]^{-1} & (i = 1, \cdots, N-1) \end{cases} \end{aligned} \tag{4.17}$$

From Equation (4.17), the recursive relationship between U_i and U_{i-1} can be derived as:

$$U_i = \frac{-B_{i(i+1)}}{B_{ii} + B_{i(i-1)} U_{i-1}} \qquad (i = 2, \cdots, N\text{-}1) \tag{4.18}$$

As demonstrated in Section 4.2, this research proposes to consider a decentralized damage detection approach in which acceleration measurements are taken at one pair of neighboring DOFs at a time, following the DOF sequences of 1-2, 2-3, …, and (N-1)-N.

The sensor location scheme is similar to that illustrated in Figure 4.1(b). However, to obtain each pair of acceleration measurements, it is proposed that an external excitation is applied at the latter DOF in the pair. For example, the measurement is taken at DOF pair 2-3, when the external excitation is applied at DOF-3.

Following the decentralized measurement and excitation scheme, according to Equations (4.7) and (4.16), the transmissibility functions between every two neighboring DOFs can be expressed as:

$$T_{i(i+1)} = \frac{H_{i(i+1)}}{H_{(i+1)(i+1)}} = \frac{U_i H_{(i+1)(i+1)}}{H_{(i+1)(i+1)}} = U_i \ , \quad i = 1, \cdots, N-1 \tag{4.19}$$

From Equation (4.18), when s is large enough, U_1 can be simplified as

$$U_1 = \frac{-B_{12}}{B_{11}} = \frac{c_2 s + k_2}{m_1 s^2 + (c_1 + c_2)s + k_1 + k_2} \approx \frac{c_2 s + k_2}{m_1 s^2} \tag{4.20}$$

Substituting Equation (4.20) into Equation (4.18), when s is large enough, U_2 can be simplified as

$$U_2 = \frac{-B_{23}}{B_{22} + B_{12}U_1} \approx \frac{c_3 s + k_3}{m_2 s^2 + (c_2 + c_3)s + k_2 + k_3 + (-c_2 s - k_2)\dfrac{c_2 s + k_2}{m_1 s^2}} \approx \frac{c_3 s + k_3}{m_2 s^2} \tag{4.21}$$

Similarly, by iteratively applying Equation (4.18), the denominator and the numerator of U_i are dominated by the term with the highest power of s, and U_i can be approximately expressed as

$$U_i \approx \frac{c_{i+1} s + k_{i+1}}{m_i s^2} \tag{4.22}$$

The above equation gives good approximation if s has a large magnitude, such that

$$\left| m_i s^2 \right| >> \left| (c_i + c_{i+1}) s \right| \text{ and } \left| m_i s^2 \right| >> k_i + k_{i+1} \ , \quad \text{for } \forall i \tag{4.23}$$

To use transmissibility functions as damage indicator, the difference between the transmissibility functions of the undamaged structure and the damaged structure, ε_i, is used.

$$\varepsilon_i = T^D_{i(i+1)} - T_{i(i+1)} = U^D_i - U_i \tag{4.24}$$

where the superscript "D" refers to the damaged structure.

A damage indicator can be defined as the sum of the absolute value of ε_i over certain frequency range of ω:

$$DI_i = \sum_k \left| \varepsilon_i \left(s_k \right) \right| \tag{4.25}$$

where $s_k = j\omega_k$ and j is the imaginary unit.

4.3.2 Damage Scenario I – Mass Change

In scenario I, suppose that damage occurs at DOF n, and is emulated with the mass m_n changed to m^D_n. The simple scenario is studied first because in laboratory damage detection experiment, a mass change, which affects structural dynamics properties, is often used to conveniently emulate a reversible damage. According to Equation (4.15), only one diagonal entry B_{nn} in **B** matrix will change due to the damage, and all other entries remain unchanged. Let B^D_{nn} denote the corresponding entry in **B** matrix with the changed mass. Equation (4.18) indicates that after the damage, U_i will remain unchanged for $i < n$, and will change to U^D_i for $i \geqslant n$.

The difference in transmissibility functions between damaged and undamaged structures, ε_i, can be studied in three different cases categorized by measurement locations (Figure 4.15), and further simplified when s is large enough (i.e. when the inequalities in Equation (4.23) holds).

Case I (a) $i < n$

As shown in Figure 4.15(a) with $i < n$, acceleration measurements are taken at two neighboring DOFs i and $j = i+1$, while the external excitation is applied at DOF $j = i+1$. Equation (4.18) indicates U_i will remain unchanged after damage, for $i < n$. From

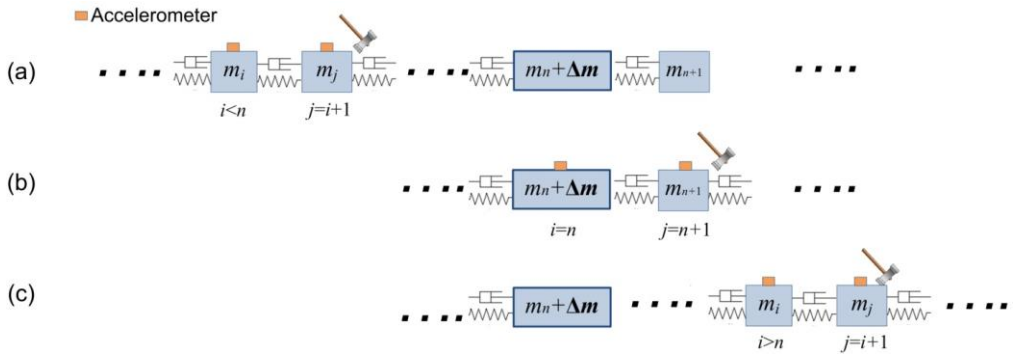

Figure 4.15. Damage scenario I: mass change at DOF *n*, while measurements are taken at DOFs *i* and *j*=*i*+1. The external excitation is applied at DOF *i*+1: (a) *i* < *n*; (b) *i* = *n*; (c) *i* > *n*

Equation (4.24), the transmissibility function difference ε_i equals zero in this case, i.e. the mass change at DOF *n* does not cause change to transmissibility function T_{ij} ($i < n$).

Case I (b) $i = n$

As shown in Figure 4.15(b) with $i = n$, the measurements are taken at two neighboring DOFs $i = n$ and $j = n+1$, while the external excitation is applied at DOF $j = n+1$. In Equation (4.18), B_{nn} is the only term that changes (to B_{nn}^D) due to the damage, and U_{n-1} will remain unchanged after damage. Substituting Equation (4.18) into Equation (4.24), the transmissibility function difference $\varepsilon_i = \varepsilon_n$ can be derived as:

$$\begin{aligned}\varepsilon_n = U_n^D - U_n &= \frac{-B_{n(n+1)}}{B_{nn}^D + B_{n(n-1)}U_{n-1}} - \frac{-B_{n(n+1)}}{B_{nn} + B_{n(n-1)}U_{n-1}} \\ &= \frac{B_{n(n+1)}\left(B_{nn}^D - B_{nn}\right)}{\left(B_{nn}^D + B_{n(n-1)}U_{n-1}\right)\left(B_{nn} + B_{n(n-1)}U_{n-1}\right)}\end{aligned} \tag{4.26}$$

Substituting Equation (4.22) into the above, when *s* is large enough (satisfying inequalities in Equation (4.23)), ε_n can be simplified by neglecting low order terms:

$$\varepsilon_n \approx \frac{-\left(c_{n+1}s + k_{n+1}\right)\left(m_n^D - m_n\right)}{m_n^D m_n s^2} \tag{4.27}$$

This means that unlike Case I(a), the mass change at DOF n causes change in transmissibility function $T_{n(n+1)}$.

Case I (c) $i > n$

As shown in Figure 4.15(c) with $i > n$, acceleration measurements are taken at two neighboring DOFs i and $j = i+1$, while the external excitation is applied at DOF $j = i+1$. In Equation (4.18), the B_{**} terms remain unchanged due to damage; only the U_{i-1} term changes to U_{i-1}^{D}. Substituting Equation (4.18) into Equation (4.24), the transmissibility function difference ε_i can be derived as:

$$\begin{aligned}\varepsilon_i = U_i^D - U_i &= \frac{-B_{i(i+1)}}{B_{ii} + B_{i(i-1)}U_{i-1}^D} - \frac{-B_{i(i+1)}}{B_{ii} + B_{i(i-1)}U_{i-1}} \\ &= \frac{B_{i(i+1)}B_{i(i-1)}\varepsilon_{i-1}}{\left(B_{ii} + B_{i(i-1)}U_{i-1}^D\right)\left(B_{ii} + B_{i(i-1)}U_{i-1}\right)}\end{aligned} \tag{4.28}$$

Substituting Equation (4.22) into the above, when s is large enough (satisfying inequalities in Equation (4.23)), ε_i can be simplified as:

$$\varepsilon_i \approx \frac{\left(c_i s + k_i\right)\left(c_{i+1}s + k_{i+1}\right)}{m_i^2 s^4}\varepsilon_{i-1} \tag{4.29}$$

According to the assumption in Equation (4.23), it is easy to prove that $m_i^2 s^4 >> \left|\left(c_i s + k_i\right)\left(c_{i+1}s + k_{i+1}\right)\right|$. As a result $|\varepsilon_i| << |\varepsilon_{i-1}|$. This means that when the measurement locations move further away from the mass change, the transmissibility function difference caused by damage reduces at a very fast rate.

To summarize all three cases for mass change, when transmissibility function T_{ij} is taken at locations before damage, as in Case I(a) with $i < n$, the function shows no difference between damaged and undamaged structures, i.e. $\varepsilon_i = 0$. When the transmissibility function T_{ij} is taken at locations past damage, as in Case I(c) with $i > n$, the difference between transmissibility functions of damaged and undamaged structures,

ε_i, is not zero but reduces very fast. Furthermore, when the transmissibility function T_{ij} is taken right at the damage, as in Case I(b) with $i = n$, the difference between transmissibility functions of damaged and undamaged structures, ε_n, is significantly larger than the previous two cases. As a result, the damage indicator, DI_i, as defined in Equation (4.25) and calculated for a relatively high frequency range, should be the largest when the excitation and measurements are next to the damage (Figure 4.15(b)). This means the damage indicator not only detects damage, but also accurately locates damage.

4.3.3 Damage Scenario II – Stiffness Change

In damage scenario II, suppose that damage occurs between DOFs n-1 and n as stiffness reduces from k_n to k_n^D. According to Equation (4.15), only entries $B_{(n-1)(n-1)}$, $B_{(n-1)n}$, $B_{n(n-1)}$ and B_{nn} in **B** matrix will change due to the damage; all other entries remain unchanged. Let $B^D_{(n-1)(n-1)}$, $B^D_{(n-1)n}$, $B^D_{n(n-1)}$ and B^D_{nn} denote the corresponding entries in **B** matrix with stiffness loss between DOFs n-1 and n. Equation (4.18) again indicates that after the damage, U_i will remain the same for $i<n$-1, and will change to U_i^D for $i \geqslant n$-1.

The difference in transmissibility functions, ε_i, can be studied in four different cases categorized by measurement locations (Figure 4.16), and further simplified when s is large enough (i.e. when the inequalities in Equation (4.23) hold).

Case II (a) $i < n$-1

As shown in Figure 4.16(a) with $i < n$-1, acceleration measurements are taken at two neighboring DOFs i and $j = i$+1, while the external excitation is applied at DOF $j = i$+1, with $i < n$-1. Equation (4.18) indicates U_i will remain unchanged after damage, for $i < n$-1. From Equation (4.24), the transmissibility function difference ε_i equals zero in this case, i.e. the stiffness loss between DOFs n-1 and n does not cause change to transmissibility function T_{ij} ($i < n$).

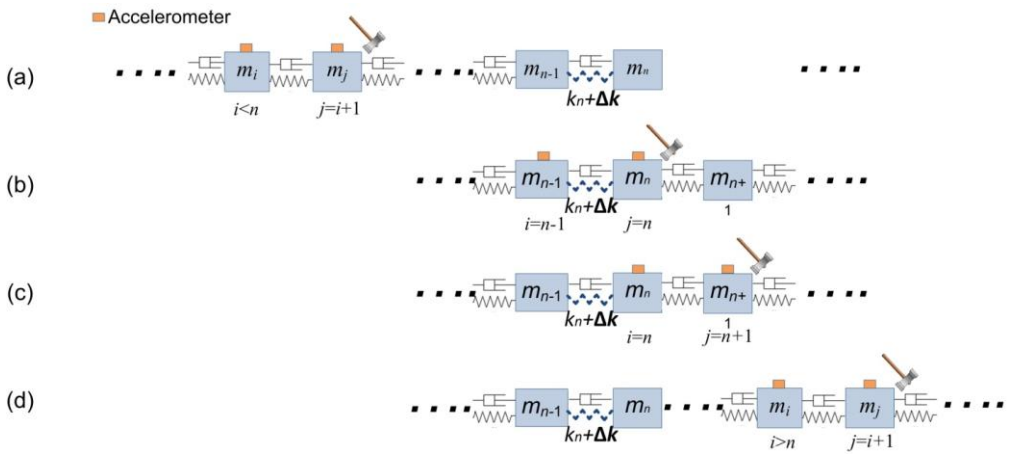

Figure 4.16. Damage scenario II: stiffness loss between DOFs *n*-1 and *n*, while measurements are taken at DOFs *i* and *j* = *i*+1. An external excitation is applied at DOF *i*+1: (a) *i* < *n*-1; (b) *i* = *n*-1; (c) *i* = *n*; (d) *i* > *n*

Case II (b) $i = n-1$

As shown in Figure 4.16(b) with $i = n-1$, the measurement is taken at two neighboring DOFs *n*-1 and *n*, while the external excitation is applied at DOF *n*. In Equation (4.18), $B_{(n-1)(n-1)}$ and $B_{(n-1)n}$ are the only terms that change (to $B^D_{(n-1)(n-1)}$ and $B^D_{(n-1)n}$, respectively) due to the damage, and U_{n-2} will remain unchanged after damage. Substituting Equation (4.18) into Equation (4.24), the transmissibility function difference ε_{n-1} can be derived as:

$$\begin{aligned}\varepsilon_{n-1} &= U^D_{n-1} - U_{n-1} = \frac{-B^D_{(n-1)n}}{B^D_{(n-1)(n-1)} + B_{(n-1)(n-2)}U_{n-2}} - \frac{-B_{(n-1)n}}{B_{(n-1)(n-1)} + B_{(n-1)(n-2)}U_{n-2}} \\ &= \frac{B_{(n-1)n}B^D_{(n-1)(n-1)} - B^D_{(n-1)n}B_{(n-1)(n-1)} + \left(B_{(n-1)n} - B^D_{(n-1)n}\right)B_{(n-1)(n-2)}U_{n-2}}{\left(B^D_{(n-1)(n-1)} + B_{(n-1)(n-2)}U_{n-2}\right)\left(B_{(n-1)(n-1)} + B_{(n-1)(n-2)}U_{n-2}\right)}\end{aligned} \tag{4.30}$$

Substituting Equation (4.22) into the above, and neglecting lower order terms when *s* is large enough, ε_{n-1} can be simplified as:

$$\varepsilon_{n-1} \approx \frac{(k_n^D - k_n)}{m_{n-1} s^2} \tag{4.31}$$

This means that unlike Case II(a), the stiffness change between DOFs *n*-1 and *n* in Case II(b) causes change in transmissibility function $T_{(n\text{-}1)n}$.

Case II (c) $i = n$

As shown in Figure 4.16(c) with $i = n$, acceleration measurements are taken at two neighboring DOFs *n* and *n*+1, while the external excitation is applied at DOF *n*+1. In Equation (4.18), B_{nn}, $B_{n(n\text{-}1)}$ and $U_{n\text{-}1}$ are the terms that change (to B_{nn}^D, $B_{(n-1)n}^D$, and U_{n-1}^D respectively) due to the damage. Substituting Equation (4.18) into Equation (4.24), the transmissibility function difference ε_n can be derived as:

$$\begin{aligned} \varepsilon_n = U_n^D - U_n &= \frac{-B_{n(n+1)}}{B_{nn}^D + B_{n(n-1)}^D U_{n-1}^D} - \frac{-B_{n(n+1)}}{B_{nn} + B_{n(n-1)} U_{n-1}} \\ &= \frac{B_{n(n+1)} \left(B_{nn}^D - B_{nn} + B_{n(n-1)}^D U_{n-1}^D - B_{n(n-1)} U_{n-1} \right)}{\left(B_{nn}^D + B_{n(n-1)}^D U_{n-1}^D \right) \left(B_{nn} + B_{n(n-1)} U_{n-1} \right)} \end{aligned} \tag{4.32}$$

Substituting Equation (4.22) into the above, and neglecting lower order terms when *s* is large enough, ε_n can be simplified as:

$$\varepsilon_n \approx \frac{-\left(c_{n+1} s + k_{n+1} \right) \left(k_n^D - k_n \right)}{m_n^2 s^4} \tag{4.33}$$

Comparing Equations (4.32) and (4.33), the relationship between transmissibility function differences for Case II (b) and Case II (c) can be derived as

$$\varepsilon_n \approx \frac{-\left(c_{n+1} s + k_{n+1} \right) m_{n-1}}{m_n^2 s^2} \varepsilon_{n-1} \tag{4.34}$$

Besides the assumption in Equation (4.23), if it is assumed that the system has relatively uniform mass distribution, it is easy to prove that $|\varepsilon_n| << |\varepsilon_{n-1}|$. This means that compared with Case II(b) involving ε_{n-1}, i.e. change in transmissibility function $T_{(n\text{-}1)n}$, Case II(c) observes less change in transfer function $T_{n(n+1)}$ when *s* is large enough.

Case II (d) $i > n$

As shown in Figure 4.16(d) with $i > n$, acceleration measurements are taken at two neighboring DOFs i and $j = i+1$, while the external excitation is applied at DOF $j = i+1$. In Equation (4.18), the B_{**} terms remain unchanged due to damage, and only U_{i-1} term changes to U_{i-1}^{D}. This situation is the same as in Case I (c) with mass change. The transmissibility function difference ε_i can be derived and simplified in Equations (4.28) and (4.29). As a result, this also means that when the measurement locations move further away from the stiffness change, the transmissibility function difference caused by damage reduces at a very fast rate.

To summarize all four cases for stiffness change, when transmissibility function T_{ij} is taken at locations before damage, as in Case II(a) with $i < n-1$, the function shows no difference between damaged and undamaged structures, i.e. $\varepsilon_i = 0$. When the transmissibility function T_{ij} is taken at locations past damage, as in Case II(d) with $i > n$, the difference between transmissibility functions of damaged and undamaged structures, ε_i, is not zero but reduces very fast. Furthermore, when the transmissibility function T_{ij} is taken right next to the damage, as in Case II(b) with $i = n-1$ and Case II(c) with $i = n$, the difference between transmissibility functions of damaged and undamaged structures is significantly larger than the previous two cases. Among Case II(b) and Case II(c), the former gives larger difference between transmissibility functions of damaged and undamaged structures, i.e. $|\varepsilon_{n-1}| >> |\varepsilon_n|$ at higher-frequency domain ($s = j\omega$ has a large magnitude) as shown by Equation (4.34). Overall, the damage indicator, DI_i, as defined in Equation (4.25) and calculated for a relatively high frequency range, should be the largest when the excitation and measurement are next to the damage. This means for scenarios with stiffness change, the damage indicator can also accurately locate the damage.

4.4 Numerical and Experimental Validation to Decentralized Transmissibility Analysis

To validate the analytical studies in Section 4.3, numerical and experimental studies are described in this section. The two damage scenarios discussed in Section 4.3, i.e. mass change and stiffness loss, are considered.

4.4.1 Numerical Validation

A 10-DOF spring-mass-damper model is built in MATLAB. TABLE 4.1 summarizes the model properties of the undamaged 10-DOF spring-mass-damper model. To obtaining transmissibility functions at neighboring DOFs, the decentralized local excitation and measurement scheme described in Section 4.3 is strictly followed. Acceleration measurements are taken sequentially at pairs of DOFs (1-2, 2-3…, 9-10), while for each pair of measurements, an ideal impact excitation is applied at the larger DOF number. For example, acceleration measurements are taken at the 2nd and 3rd DOFs, when the excitation is applied at the 3rd DOF. The sampling rate is set to 1,000 Hz, and each measurement duration is set to 50 seconds. Using data from the undamaged structures, transmissibility functions $T_{i(i+1)}$ (i = 1, ..., 9) are calculated.

4.4.1.1 Damage Scenario I – Mass Change

In damage scenario I, damage is emulated by introducing mass increase at the 6th DOF by 10%. Same as the measurement scheme of the undamaged structure, for each pair of DOFs, an ideal impact is applied at the larger DOF, and acceleration records are sequentially obtained. The transmissibility functions T_{12}^{D}, T_{23}^{D}, …, T_{9-10}^{D} for the damaged

TABLE 4.1. Model properties of the 10-DOF spring-mass-damper model

DOFs	*Mass*	*Stiffness*	*Damping*
1~10	5.4kg (11.9 lbs)	3.44×10^{4} N/m (196.67 lbs/in)	2.98 N·s/m (0.017 lbs·s/in)

structure are calculated. Figure 4.17 presents the magnitude of the transmissibility functions of both the undamaged and damaged structures. It is shown at higher frequency range, e.g. 30~40Hz, $\left|T_{67}\right|$ (of undamaged structure) and $\left|T_{67}^{\mathrm{D}}\right|$(of damaged structure) have obviously the largest difference. This agrees with the conclusions from the analytical formulation in Section 4.3.2.

To quantify the difference between transmissibility functions of damaged and undamaged structures, damage indicators DI_{i} are calculated based on the transmissibility function difference in frequency range 30~40Hz (Equation (4.25)), and shown in Figure 4.18. The largest damage indicator occurs at DOFs 6-7, and other damage indicators are much smaller. This again agrees with conclusions from Section 4.3.2, i.e. the largest damage indicator occurs next to the mass change location. The damage indicators at other pairs of measurement locations are much smaller.

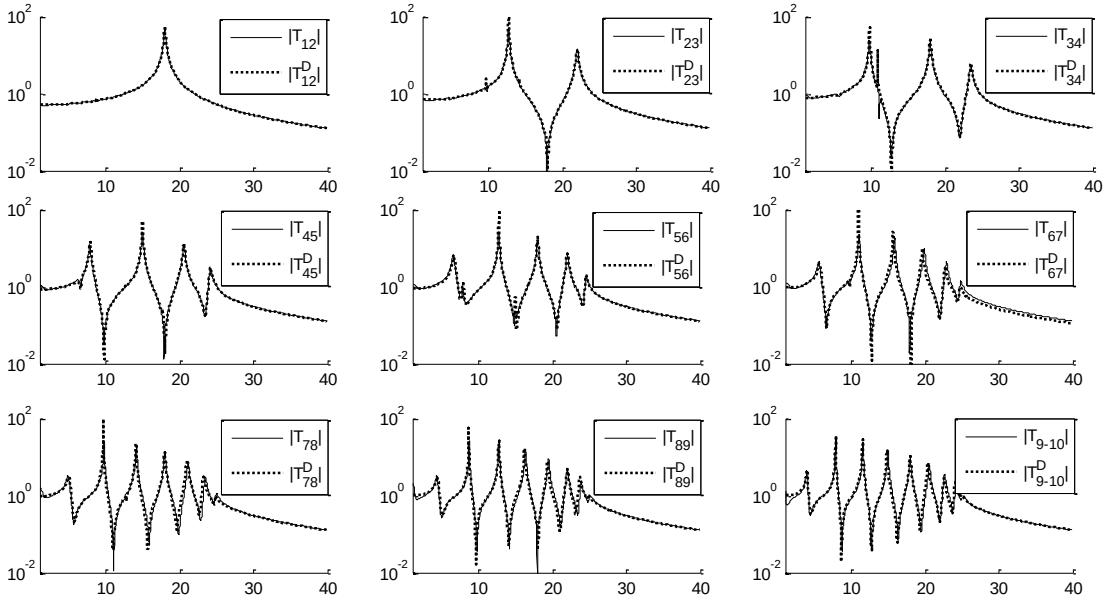

Figure 4.17. Comparison of transmissibility functions between undamaged structure and damaged structure with mass change

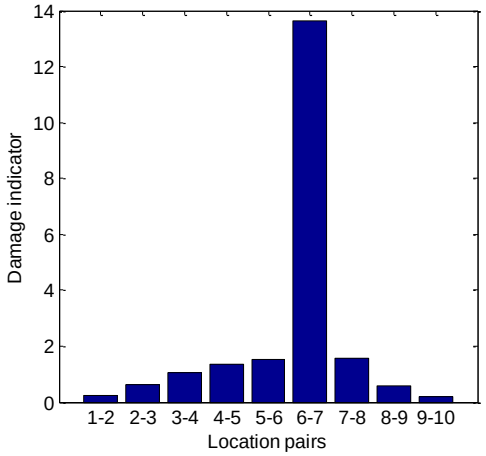

Figure 4.18. Damage scenario I - the damage indicators of the nine measurement pairs

4.4.1.2 Damage Scenario II – Stiffness Loss

In damage scenario II, damage is introduced by reducing the stiffness between the 6th and 7th DOFs by 10%. Again, for each pair of DOFs, an ideal impact is applied at the larger DOF, and acceleration records are sequentially obtained. The transmissibility functions T_{12}^{D}, T_{23}^{D}, …, T_{9-10}^{D} for the damaged structure are calculated. Figure 4.19 presents the magnitude of the transmissibility functions of both the undamaged and damaged structures. It is shown at higher frequency range, e.g. 30~40Hz, $|T_{67}|$ (of undamaged structure) and $|T_{67}^{D}|$ (of damaged structure) have the largest difference. This agrees with the conclusions from the analytical formulation in Section 4.3.3.

To quantify the difference between transmissibility functions of damaged and undamaged structures, Figure 4.20 shows damage indicators for frequency range 30~40Hz. The largest damage indicator occurs at DOFs 6 and 7, and the other damage indicators are much smaller, which again demonstrates that the largest damage indicator occurs near the damage location.

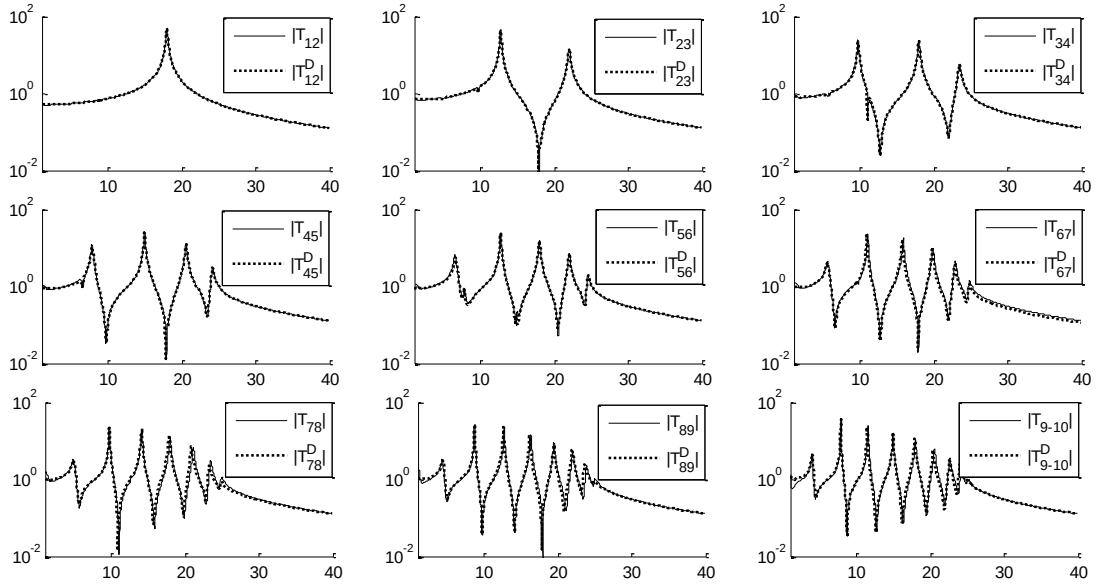

Figure 4.19. Comparison of transmissibility functions between undamaged structure and damaged structure with stiffness loss

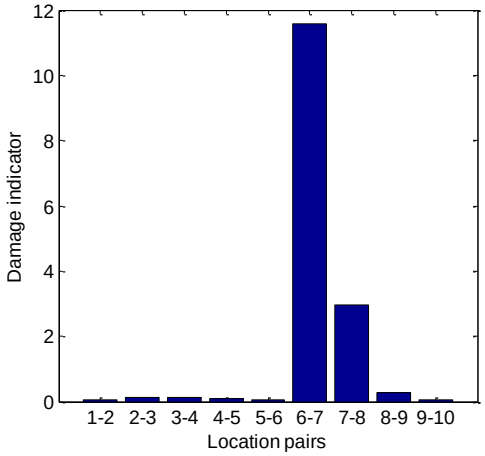

Figure 4.20. Damage scenario II - the damage indicators of the nine measurement pairs

4.4.2 Experimental Validation

To further validate the analytical studies in Section 4.3, a five-story shear-building structure is built, and abstracted as a 5-DOF spring-mass-damper system.

4.4.2.1 Experimental Setup

Figure 4.21 shows the five-story shear-building structure. The columns are steel and the floors are aluminum. The dimension of each floor is identical: 0.41m (16 in.) long, 0.305m (12 in.) wide and 0.013m (0.5 in.) thick. The two columns have the same rectangular section (0.15m (6 in.) × 0.002m (0.08 in.)). The total height of the building is 1.524m (60 in.), with 0.305m (12 in.) per story. Each floor is connected with the columns through rigid constraints. Fixed boundary condition is adopted at the base of the two columns. This five-story shear-building structure is equivalent to a 5-DOF spring-mass-damper system, because floor stiffness is much larger than stiffness of the columns. The first five natural frequencies are summarized in Figure 4.21.

Tetherless mobile sensing nodes, which are capable of moving on the steel structure as well as attaching/detaching an accelerometer (Silicon Designs 2260-010) onto/from structural surface, are used in the experiments. To follow the measurement scheme described in Section 4.3, two MSNs are adopted to sequentially take measurement at each pair of floors, i.e. 1-2, 2-3, 3-4, and 4-5, as shown in Figure 4.22. In the experiments, when the two MSNs arrive at one pair of measurement locations, the

Figure 4.21. A five-story shear-building structure

TABLE 4.2. First five natural frequencies for undamaged five-story shear building

Mode number	1	2	3	4	5
Frequency (Hz)	2.4	7.2	11.8	15.65	18.35

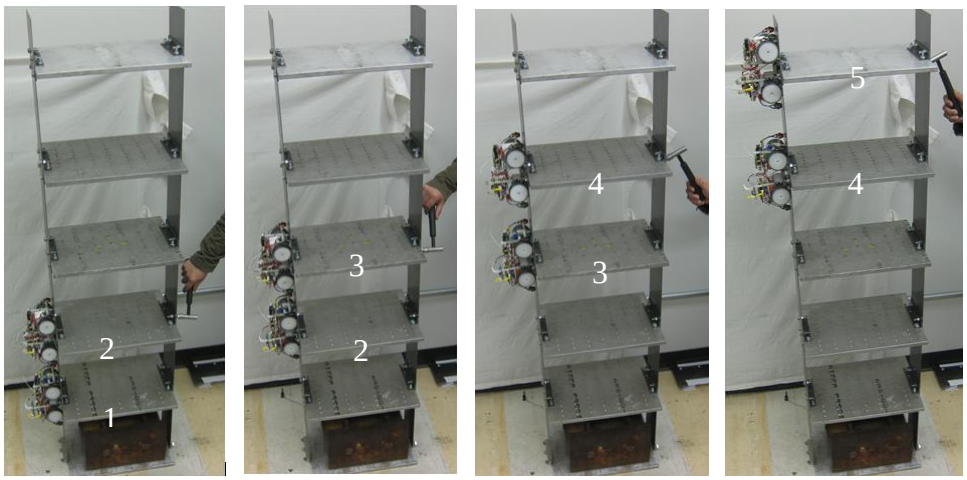

(a) Config.1 (b) Config.2 (c) Config.3 (d) Config. 4

Figure 4.22. Test configurations with MSNs

accelerometer is attached onto the structural surface; then a hammer impact is manually applied at the higher one of the location pair to excite the structure for acceleration measurement. After the measurement, these two MSNs detach accelerometers from structural surface, and move to next pair of measurement locations. In order to reduce the effect of experimental uncertainties, measurement at each location pair is repeatedly taken for 10 times. The sampling rate for the acceleration measurement is set to 1,000 Hz.

Figure 4.23 plots the example acceleration data at the 2nd and 3rd floors when the hammer impact is applied at the 3rd floor of the undamaged structure. Figure 4.24 shows the magnitude of the two frequency spectra, i.e. the discrete Fourier transform (DFT)

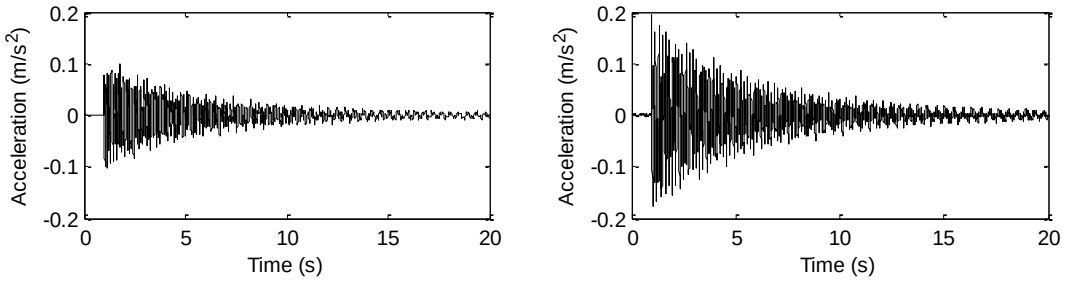

(a) (b)

Figure 4.23. Example acceleration time histories when the hammer impact is applied at the 3rd floor: (a) acceleration at the 2nd floor; (b) acceleration at the 3rd floor

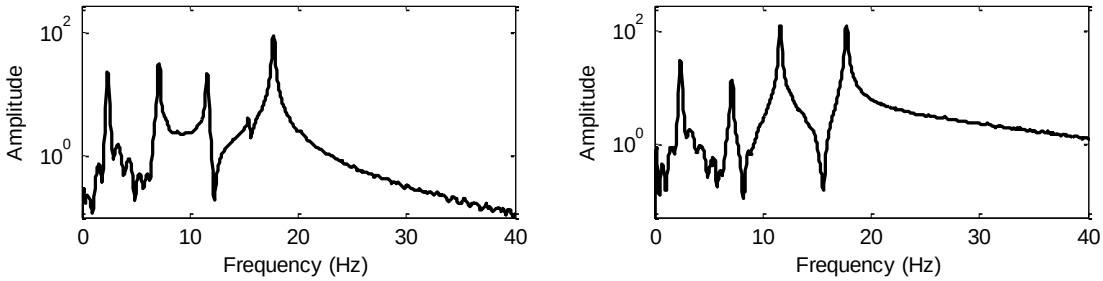

Figure 4.24. Example acceleration spectra when the hammer impact is applied at the 3rd floor: (a) acceleration spectra at the 2nd floor; (b) acceleration spectra at the 3rd floor

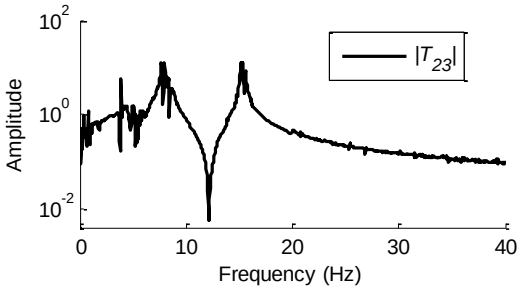

Figure 4.25. Transmissibility function T_{23} calculated using the example acceleration data

results of the acceleration time history. Transmissibility function T_{23} is calculated as the ratio between the two frequency spectra, as shown in Figure 4.25.

4.4.2.2 Damage scenario I – mass change

In damage scenario I, a mass block of 0.5kg (1.1 lbs) is attached on the 2nd floor (Figure 4.26). In contrast, the weight of the floor is about 5.025kg (11.08 lbs). With the mass block attached, acceleration measurements follow the same schemes for undamaged structure.

After obtaining all the acceleration records, the transmissibility functions for the damaged structures are calculated. To reduce the effect of experimental noise, averaged transmissibility functions are obtained from ten groups of measurement data at each floor

Figure 4.26. Damage scenario I – a 0.5kg additional mass is attached on the 2nd floor

pair. Figure 4.27 presents the magnitude of the averaged transmissibility functions of both the undamaged and damaged structures. At higher frequency range, e.g. 30~40Hz, $|T_{23}|$ (of undamaged structure) and $|T_{23}^{D}|$ (of damaged structure) have the largest difference. This agrees with the conclusion from the analytical formulation in Section 4.3.2. Figure 4.28 shows damage indicators for frequency range 30~40Hz. The largest damage indicator is $DI_{2\text{-}3}$, and all other damage indicators are much smaller. The experimental results also demonstrate the effectiveness of the proposed decentralized transmissibility approach in locating damage.

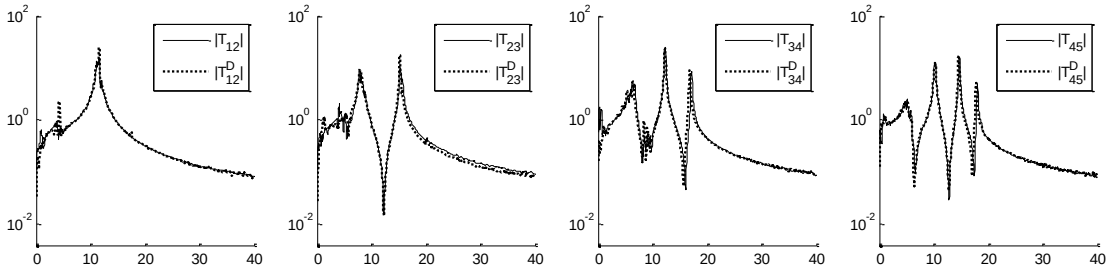

Figure 4.27. Comparison of averaged transmissibility functions between undamaged structure and damaged structure (with additional mass)

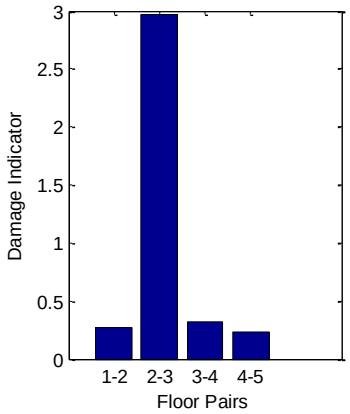

Figure 4.28. Damage scenario I - the damage indicators at four measurement pairs

4.4.2.3 Damage Scenario II – Stiffness Loss

In damage scenario II, a 20% stiffness loss is introduced to the left column, between the 2nd and 3rd floors (Figure 4.29), by decreasing the section width by 20%. After the stiffness loss, acceleration measurements follow the same schemes.

Figure 4.30 presents the magnitude of the averaged transmissibility functions of both the undamaged and damaged structures. At higher frequency range, e.g. 30~40Hz, $|T_{23}|$ (of undamaged structure) and $|T_{23}^{D}|$ (of damaged structure) have the largest

Figure 4.29. Damage scenario II - 20% stiffness loss is introduced to the section of one column between 2nd and 3rd floors

difference. This also agrees with the conclusions from the analytical formulation in Section 4.3. The damage indicators are calculated based on the transmissibility function difference in frequency range 30~40Hz (Equation (4.25)), and shown in Figure 4.31. The largest damage indicator is $DI_{2\text{-}3}$, and the other damage indicators are much smaller, which again agrees with analytical conclusions made in Section 4.3.3.

4.5 Summary

This chapter explores MSNs for structural damage detection, in which transmissibility analysis is applied on mobile sensor data. A decentralized structural damage detection procedure is proposed for the MSNs. Laboratory experiments are conducted with a two-node mobile sensor network. The MSNs only measure a small part

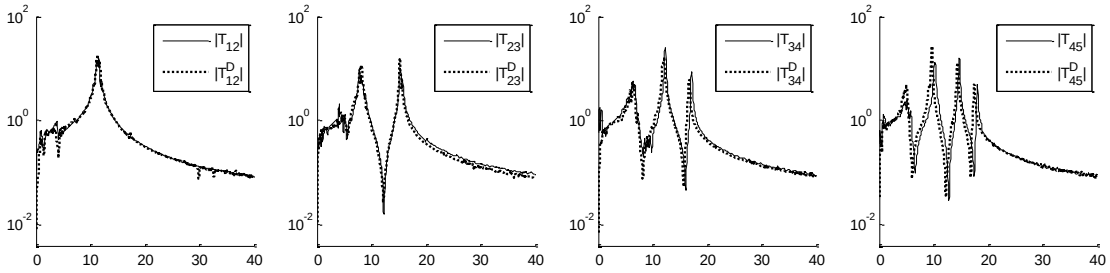

Figure 4.30. Comparison of averaged transmissibility functions between undamaged structure and damaged structure (with stiffness loss)

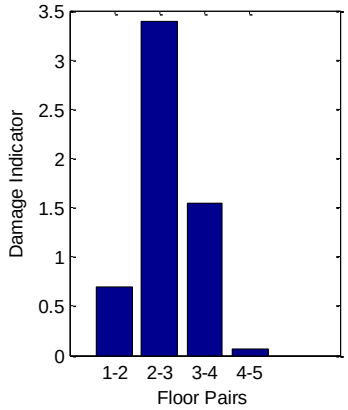

Figure 4.31. Damage scenario II - the damage indicators at four measurement pairs

of the structure at a time, in order to generate damage signature (transmissibility function) for those measured locations. After measurement, the small number of MSNs move to next configuration, and repeat the procedure till the entire structure is scanned. Various damage scenarios are studied and the damage locations are successfully identified using mobile sensor data.

Besides experimental validation with MSNs, this study also investigates the analytical nature of transmissibility functions for damage detection, based on a general multi-DOF spring-mass-damper system. Analytical derivations show that the difference in transmissibility functions between undamaged and damaged structures is sensitive to various damage scenarios and the largest damage indicator should occur near a damage location. The analytical derivations are validated through numerical simulations and laboratory experiments on a 5-story shear-building structure using MSNs. Damage identification results using both simulation and experimental data agree with the conclusion from the theoretical analysis.

CHAPTER 5 DECENTRALIZED SYSTEM MODEL UPDATING THROUGH MINIMIZATION OF MODAL DYNAMIC RESIDUALS

Although wireless and mobile sensors further reduce system instrumentation time and cost for a large-scale structure, there is still a large gap between the number of DOFs on the actual structure and the number of DOFs that can be measured. In addition, when operating on an entire structural model with very large amount of DOFs, most of the existing algorithms suffer computational challenges and convergence difficulties. One potential solution is to focus the sensor instrumentation channels on one part of the structure, named a substructure, to achieve dense instrumentation in the substructure. Subsequently, model updating can be performed to the substructure model with much less DOFs, so that computational efficiency and convergence can be improved.

This chapter explores substructure model updating using frequency domain data. The entire structural model is divided into the substructure (currently being instrumented and to be updated) and the residual structure. The Craig-Bampton transform is adopted to condense the residual structure using a limited number of dominant modal coordinates, while the substructure model remains at high resolution. To update the condensed structural model, physical parameters in the substructure and modal parameters of the residual structure are chosen as optimization variables; minimization of the modal dynamic residuals from the eigenvalue equations in structural dynamics is chosen as the optimization objective. An iterative linearization procedure is adopted for efficiently solving the optimization problem.

This chapter is organized as follows. Section 5.1 presents the formulation of substructure modeling. Section 5.2 describes substructure updating through the optimization procedure of iteratively minimizing modal dynamic residuals. Section 5.3 shows a number of numerical examples for validating the proposed approach. Section 5.4

discusses key issues, i.e. performance comparison with model updating of entire structure, and investigation on substructure location and size. Section 5.5 summarizes the study in this chapter.

5.1 Substructure Modeling

This section presents the basic formulation for substructure modeling. Subsection 5.1.1 describes the condensation strategy following the Craig-Bampton transform. Subsection 5.1.2 describes the formulations of the sensitivity matrices for model updating variables.

5.1.1 Structural Model Condensation

Figure 5.1 illustrates the substructure modeling strategy following the Craig-Bampton transform [60, 61]. Subscripts *s*, *i*, and *r* are used to denote DOFs associated with the substructure being analyzed, the interface nodes, and the residual structure, respectively. The block-bidiagonal structural stiffness and mass matrices, **K** and **M**, can be assembled using original DOFs $\mathbf{x} = \begin{bmatrix} \mathbf{x}_s & \mathbf{x}_i & \mathbf{x}_r \end{bmatrix}^{\mathrm{T}}$.

$$\mathbf{K} = \begin{bmatrix} \begin{bmatrix} \mathbf{K}_S \end{bmatrix} & \mathbf{0} \\ \mathbf{0} & \mathbf{0} \end{bmatrix} + \begin{bmatrix} \mathbf{0} & \mathbf{0} & \mathbf{0} \\ \mathbf{0} & \begin{bmatrix} \mathbf{K}_R \end{bmatrix} \end{bmatrix} = \begin{bmatrix} \begin{bmatrix} \mathbf{K}_{ss} & \mathbf{K}_{si} \\ \mathbf{K}_{is} & \mathbf{K}_{ii}^S \end{bmatrix} & \mathbf{0} \\ \mathbf{0} & \mathbf{0} \end{bmatrix} + \begin{bmatrix} \mathbf{0} & \mathbf{0} & \mathbf{0} \\ \mathbf{0} & \begin{bmatrix} \mathbf{K}_{ii}^R & \mathbf{K}_{ir} \\ \mathbf{K}_{ri} & \mathbf{K}_{rr} \end{bmatrix} \end{bmatrix} \tag{5.1}$$

$$\mathbf{M} = \begin{bmatrix} \begin{bmatrix} \mathbf{M}_S \end{bmatrix} & \mathbf{0} \\ \mathbf{0} & \mathbf{0} \end{bmatrix} + \begin{bmatrix} \mathbf{0} & \mathbf{0} & \mathbf{0} \\ \mathbf{0} & \begin{bmatrix} \mathbf{M}_R \end{bmatrix} \end{bmatrix} = \begin{bmatrix} \begin{bmatrix} \mathbf{M}_{ss} & \mathbf{M}_{si} \\ \mathbf{M}_{is} & \mathbf{M}_{ii}^S \end{bmatrix} & \mathbf{0} \\ \mathbf{0} & \mathbf{0} \end{bmatrix} + \begin{bmatrix} \mathbf{0} & \mathbf{0} & \mathbf{0} \\ \mathbf{0} & \begin{bmatrix} \mathbf{M}_{ii}^R & \mathbf{M}_{ir} \\ \mathbf{M}_{ri} & \mathbf{M}_{rr} \end{bmatrix} \end{bmatrix} \tag{5.2}$$

Here $\mathbf{K}_S$ and $\mathbf{M}_S$ denote entries of the stiffness and mass matrices corresponding to the substructure; $\mathbf{K}_R$ and $\mathbf{M}_R$ denote entries corresponding to the residual structure; $\mathbf{K}_{ii}^S$ and $\mathbf{M}_{ii}^S$ denote the entries at the interface DOFs and contributed by the substructure; $\mathbf{K}_{ii}^R$ and $\mathbf{M}_{ii}^R$ denote entries at the interface DOFs and contributed by the residual structure.

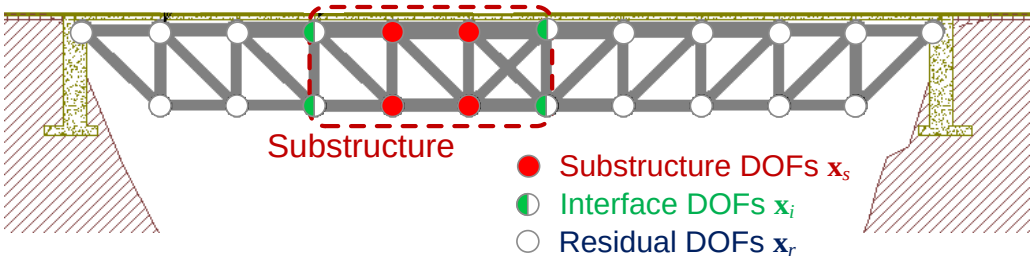

Figure 5.1. Illustration of substructure modeling strategy

The dynamic behavior of the residual structure can be approximated using the Craig-Bampton formulation [60, 61]. The DOFs of the residual structure, $\mathbf{x}_r \in \mathbb{R}^{n_r}$, are approximated by a linear combination of interface DOFs, $\mathbf{x}_i \in \mathbb{R}^{n_i}$, and modal coordinates of the residual structure, $\mathbf{q}_r \in \mathbb{R}^{n_q}$.

$$\mathbf{x}_r \approx \mathbf{T}\mathbf{x}_i + \mathbf{\Phi}_r \mathbf{q}_r \tag{5.3}$$

Here $\mathbf{T} = -\mathbf{K}_{rr}^{-1}\mathbf{K}_{ri}$ is the Guyan static condensation matrix; $\mathbf{\Phi}_r = \left[\boldsymbol{\varphi}_1, ..., \boldsymbol{\varphi}_{n_q}\right]$ represents the mode shapes of the residual structure with interface DOFs fixed. The eigenvalue equation for structural dynamics, providing the mode shapes $\mathbf{\Phi}_r$ and modal frequencies ω_r, can be written as

$$\left(-\omega_{r,j}{}^2\mathbf{M}_{rr} + \mathbf{K}_{rr}\right)\boldsymbol{\varphi}_j = 0, \qquad j = 1, ..., n_q \tag{5.4}$$

Although the size of the residual structure may be large, the number of modal coordinates, n_q, can be chosen as relatively small to reflect the first few dominant mode shapes only (i.e. $n_q << n_r$). The coordinate transformation is rewritten in vector form as:

$$\begin{bmatrix}\mathbf{x}_i \\ \mathbf{x}_r\end{bmatrix} \approx \mathbf{\Gamma}\begin{bmatrix}\mathbf{x}_i \\ \mathbf{q}_r\end{bmatrix}, \text{ where } \quad \mathbf{\Gamma} = \begin{bmatrix}\mathbf{I} & \\ \mathbf{T} & \mathbf{\Phi}_r\end{bmatrix} \tag{5.5}$$

Suppose $\tilde{\mathbf{K}}_R$ and $\tilde{\mathbf{M}}_R$ denote the new stiffness and mass matrices of the residual structure after transformation:

$$\tilde{\mathbf{K}}_R = \boldsymbol{\Gamma}^{\mathrm{T}}\mathbf{K}_R\boldsymbol{\Gamma} = \begin{bmatrix} \tilde{\mathbf{K}}_{ii} & \\ & \boldsymbol{\gamma} \end{bmatrix} = \begin{bmatrix} \mathbf{K}_{ii}^R + \mathbf{T}^{\mathrm{T}}\mathbf{K}_{ri} & \\ & \boldsymbol{\Phi}_r^{\mathrm{T}}\mathbf{K}_{rr}\boldsymbol{\Phi}_r \end{bmatrix} \tag{5.6}$$

$$\begin{aligned} \tilde{\mathbf{M}}_R &= \boldsymbol{\Gamma}^{\mathrm{T}}\mathbf{M}_R\boldsymbol{\Gamma} = \begin{bmatrix} \tilde{\mathbf{M}}_{ii} & \tilde{\mathbf{M}}_{iq} \\ \tilde{\mathbf{M}}_{qi} & \boldsymbol{\mu} \end{bmatrix} \\ &= \begin{bmatrix} \mathbf{M}_{ii}^R + \mathbf{T}^{\mathrm{T}}\mathbf{M}_{ri} + \mathbf{M}_{ir}\mathbf{T} + \mathbf{T}^{\mathrm{T}}\mathbf{M}_{rr}\mathbf{T} & (\mathbf{M}_{ir} + \mathbf{T}^{\mathrm{T}}\mathbf{M}_{rr})\boldsymbol{\Phi}_r \\ \boldsymbol{\Phi}_r^{\mathrm{T}}(\mathbf{M}_{ri} + \mathbf{M}_{rr}\mathbf{T}) & \boldsymbol{\Phi}_r^{\mathrm{T}}\mathbf{M}_{rr}\boldsymbol{\Phi}_r \end{bmatrix} \end{aligned} \tag{5.7}$$

where $\boldsymbol{\gamma} = \mathrm{diag}(\gamma_1, \cdots, \gamma_{n_q})$ and $\boldsymbol{\mu} = \mathrm{diag}(\mu_1, \cdots, \mu_{n_q})$ are diagonal modal stiffness and modal mass matrices of the residual structure fixed at the interface. Note that due to the static condensation process in this transformation, the off-diagonal block entries of $\tilde{\mathbf{K}}_R$ are zero.

Under transformation to the residual structure, a new set of stiffness matrix $\tilde{\mathbf{K}}$ and structural mass matrix $\tilde{\mathbf{M}}$ of the entire structure can be assembled, while contribution from the substructure, $\mathbf{K}_S$ and $\mathbf{M}_S$ (Equations (5.1) and (5.2)), remains unchanged. Dimension of $\tilde{\mathbf{K}}_R$ and $\tilde{\mathbf{M}}_R$ is $(n_i + n_q) \times (n_i + n_q)$. Because only a few dominant modal coordinates of the residual structure are adopted (i.e. $n_q << n_r$), dimension of $\tilde{\mathbf{K}}$ and $\tilde{\mathbf{M}}$ (both are $n_s + n_i + n_q$) is condensed to be much smaller than original matrices **K** and **M**.

$$\tilde{\mathbf{K}} = \begin{bmatrix} \begin{bmatrix} \mathbf{K}_S & & \end{bmatrix} & \mathbf{0} \\ \mathbf{0} \quad \mathbf{0} \quad \mathbf{0} & \mathbf{0} \end{bmatrix} + \begin{bmatrix} \mathbf{0} & \mathbf{0} \quad \mathbf{0} \\ \mathbf{0} & \begin{bmatrix} \tilde{\mathbf{K}}_R & \end{bmatrix} \\ \mathbf{0} & \end{bmatrix} = \begin{bmatrix} \mathbf{K}_{ss} & \mathbf{K}_{si} & \mathbf{0} \\ \mathbf{K}_{is} & \mathbf{K}_{ii}^S + \tilde{\mathbf{K}}_{ii} & \mathbf{0} \\ \mathbf{0} & \mathbf{0} & \boldsymbol{\gamma} \end{bmatrix} \tag{5.8}$$

$$\tilde{\mathbf{M}} = \begin{bmatrix} \begin{bmatrix} \mathbf{M}_S & & \end{bmatrix} & \mathbf{0} \\ \mathbf{0} \quad \mathbf{0} \quad \mathbf{0} & \mathbf{0} \end{bmatrix} + \begin{bmatrix} \mathbf{0} & \mathbf{0} \quad \mathbf{0} \\ \mathbf{0} & \begin{bmatrix} \tilde{\mathbf{M}}_R & \end{bmatrix} \\ \mathbf{0} & \end{bmatrix} = \begin{bmatrix} \mathbf{M}_{ss} & \mathbf{M}_{si} & \mathbf{0} \\ \mathbf{M}_{is} & \mathbf{M}_{ii}^S + \tilde{\mathbf{M}}_{ii} & \tilde{\mathbf{M}}_{iq} \\ \mathbf{0} & \tilde{\mathbf{M}}_{qi} & \boldsymbol{\mu} \end{bmatrix} \tag{5.9}$$

5.1.2 Sensitivities of Model Updating Variables

The updating variable for the substructure can be physical parameters, such as elastic modulus and density of each substructure element. Assuming the updating parameters are independent, the substructure matrices can be updated as

$$\mathbf{K}_S = \mathbf{K}_{S0} + \sum_{j=1}^{n_\alpha} \alpha_j \mathbf{K}_{S0,j} \qquad \mathbf{M}_S = \mathbf{M}_{S0} + \sum_{j=1}^{n_\beta} \beta_j \mathbf{M}_{S0,j} \tag{5.10}$$

where $\mathbf{K}_{S0}$ and $\mathbf{M}_{S0}$ are the stiffness and mass matrices of the substructure and used as initial starting point in the model updating; α_j and β_j correspond to physical system parameters to be updated; n_α and n_β represent the total number of corresponding parameters to be updated; $\mathbf{K}_{S0,j}$ and $\mathbf{M}_{S0,j}$ are constant matrices determined by the type and location of these parameters. Subscript "0" will be used hereinafter to denote variables associated with the initial structural model, which serves as the starting point for model updating.

Link described a model updating method for the condensed residual structure matrices [62]. The matrices of the condensed residual structural model, $\tilde{\mathbf{K}}_R$ and $\tilde{\mathbf{M}}_R$ in Equations (5.6) and (5.7), contains $(n_i + n_q) \times (n_i + n_q)$ number of entries. Assuming that physical changes in the original residual structure do not significantly alter the generalized eigenvectors of $\tilde{\mathbf{K}}_R$ and $\tilde{\mathbf{M}}_R$, only $(n_i + n_q)$ number of modal parameters are selected as updating parameters for each condensed matrix of the residual structural model :

$$\tilde{\mathbf{K}}_R = \tilde{\mathbf{K}}_{R0} + \sum_{j=1}^{n_i+n_q} \zeta_j \tilde{\mathbf{K}}_{R0,j} \qquad \tilde{\mathbf{M}}_R = \tilde{\mathbf{M}}_{R0} + \sum_{j=1}^{n_i+n_q} \eta_j \tilde{\mathbf{M}}_{R0,j} \tag{5.11}$$

where ζ_j and η_j are the modal parameters to be updated; $\tilde{\mathbf{K}}_{R0}$ and $\tilde{\mathbf{M}}_{R0}$ are the initial stiffness and mass matrices of the condensed residual structure model; $\tilde{\mathbf{K}}_{R0,j}$ and $\tilde{\mathbf{M}}_{R0,j}$ represent the constant correction matrices formulated using modal back-transform:

$$\tilde{\mathbf{K}}_{R0,j} = \boldsymbol{\varphi}_{R0,j}^{l} \omega_{R0,j}^2 \boldsymbol{\varphi}_{R0,j}^{l,\mathrm{T}} \qquad \tilde{\mathbf{M}}_{R0,j} = \boldsymbol{\varphi}_{R0,j}^{l} \boldsymbol{\varphi}_{R0,j}^{l,\mathrm{T}} \tag{5.12}$$

where

$$\begin{bmatrix} \boldsymbol{\varphi}_{R0,1}^{l} & \cdots & \boldsymbol{\varphi}_{R0,n_i+n_q}^{l} \end{bmatrix} = \boldsymbol{\Phi}_{R0}^{-\mathrm{T}} = \begin{bmatrix} \boldsymbol{\varphi}_{R0,1} & \cdots & \boldsymbol{\varphi}_{R0,n_i+n_q} \end{bmatrix}^{-\mathrm{T}} \tag{5.13}$$

$\omega_{R0,j}$ and $\boldsymbol{\varphi}_{R0,j}$ are the *j*-th generalized eigenvalue and mass-normalized eigenvector of the initial transformed residual structural model with free interface:

$$\boldsymbol{\Phi}_{R0}^{\mathrm{T}}\tilde{\mathbf{M}}_{R0}\boldsymbol{\Phi}_{R0}=\mathbf{I} \qquad \boldsymbol{\Phi}_{R0}^{\mathrm{T}}\tilde{\mathbf{K}}_{R0}\boldsymbol{\Phi}_{R0}=\mathrm{diag}(\omega_{R0,1}^2,\cdots,\omega_{R0,(n_q+n_i)}^2) \tag{5.14}$$

Using all model matrices to be updated, i.e. Equation (5.10) for substructure and Equation (5.11) for residual structure, the condensed entire structural model with reduced DOFs, $\begin{bmatrix}\mathbf{x}_s & \mathbf{x}_i & \mathbf{q}_r\end{bmatrix}^{\mathrm{T}}$, can be updated with variables α_j, β_j, ζ_j and η_j.

$$\begin{aligned}\tilde{\mathbf{K}} &= \tilde{\mathbf{K}}_0+\sum_{j=1}^{n_\alpha}\alpha_j\begin{bmatrix}\begin{bmatrix}\mathbf{K}_{S0,j}\end{bmatrix} & \mathbf{0}\\ \mathbf{0} & \mathbf{0}\end{bmatrix}+\sum_{j=1}^{n_i+n_q}\zeta_j\begin{bmatrix}\mathbf{0} & \mathbf{0}\\ \mathbf{0} & \begin{bmatrix}\tilde{\mathbf{K}}_{R0,j}\end{bmatrix}\end{bmatrix}\\ &= \tilde{\mathbf{K}}_0+\sum_{j=1}^{n_\alpha}\alpha_j\mathbf{S}_{\alpha,j}+\sum_{j=1}^{n_i+n_q}\zeta_j\mathbf{S}_{\zeta,j}\end{aligned} \tag{5.15}$$

$$\begin{aligned}\tilde{\mathbf{M}} &= \tilde{\mathbf{M}}_0+\sum_{j=1}^{n_\beta}\beta_j\begin{bmatrix}\begin{bmatrix}\mathbf{M}_{S0,j}\end{bmatrix} & \mathbf{0}\\ \mathbf{0} & \mathbf{0}\end{bmatrix}+\sum_{j=1}^{n_i+n_q}\eta_j\begin{bmatrix}\mathbf{0} & \mathbf{0}\\ \mathbf{0} & \begin{bmatrix}\tilde{\mathbf{M}}_{R0,j}\end{bmatrix}\end{bmatrix}\\ &= \tilde{\mathbf{M}}_0+\sum_{j=1}^{n_\alpha}\beta_j\mathbf{S}_{\beta,j}+\sum_{j=1}^{n_i+n_q}\eta_j\mathbf{S}_{\eta,j}\end{aligned} \tag{5.16}$$

where $\mathbf{S}_{\alpha,j}$, $\mathbf{S}_{\beta,j}$, $\mathbf{S}_{\zeta,j}$ and $\mathbf{S}_{\eta,j}$ represent the constant sensitivity matrices corresponding to variables α_j, β_j, ζ_j and η_j, respectively. For brevity, these variables will be referred to in vector form as $\boldsymbol{\alpha}\in\mathbb{R}^{n_\alpha}$, $\boldsymbol{\beta}\in\mathbb{R}^{n_\beta}$, $\boldsymbol{\zeta}\in\mathbb{R}^{n_i+n_q}$ and $\boldsymbol{\eta}\in\mathbb{R}^{n_i+n_q}$.

5.2 Substructure Updating

To update the condensed structural model, a modal dynamic residual approach is proposed in this study. For comparison purpose, a conventional modal property difference approach is also considered in this study. For both approaches, it is assumed that sensors are deployed on the substructure and interface DOFs at high density, so that mode shapes in the substructure area can be identified from experimental data. Sensor

instrumentation at the residual DOFs is not required. Subsections 5.2.1 and 5.2.2 describe the two updating approaches, respectively.

5.2.1 Modal Dynamic Residual Approach

The proposed model updating approach attempts to minimize modal dynamic residuals of the generalized eigenvalue equation for the condensed structural model :

$$\begin{aligned} &\underset{\boldsymbol{\alpha},\boldsymbol{\beta},\boldsymbol{\zeta},\boldsymbol{\eta},\boldsymbol{\psi}_{\mathrm{u}}}{\text{minimize}} \quad && \sum_{j=1}^{n_{\mathrm{m}}} \left\| \left[\tilde{\mathbf{K}}(\boldsymbol{\alpha},\boldsymbol{\zeta}) - \omega_j^2 \tilde{\mathbf{M}}(\boldsymbol{\beta},\boldsymbol{\eta}) \right] \begin{Bmatrix} \boldsymbol{\psi}_{\mathrm{m},j} \\ \boldsymbol{\psi}_{\mathrm{u},j} \end{Bmatrix} \right\|^2 \\ &\text{subject to} \quad && \boldsymbol{\alpha}_L \le \boldsymbol{\alpha} \le \boldsymbol{\alpha}_U ; \quad \boldsymbol{\beta}_L \le \boldsymbol{\beta} \le \boldsymbol{\beta}_U ; \quad \boldsymbol{\zeta}_L \le \boldsymbol{\zeta} \le \boldsymbol{\zeta}_U ; \quad \boldsymbol{\eta}_L \le \boldsymbol{\eta} \le \boldsymbol{\eta}_U \end{aligned} \tag{5.17}$$

where $\|\bullet\|$ denotes any vector norm; n_{m} denotes the number of measured modes from experiments; ω_j denotes the *j*-th modal frequency extracted from experimental data; $\boldsymbol{\psi}_{\mathrm{m},j}$ denotes the entries in the *j*-th mode shape that correspond to measured (instrumented) DOFs; $\boldsymbol{\psi}_{\mathrm{u},j}$ correspond to unmeasured DOFs; $\boldsymbol{\alpha}$, $\boldsymbol{\beta}$, $\boldsymbol{\zeta}$ and $\boldsymbol{\eta}$ are the system parameters to be updated (see Equations (5.15) and (5.16)). Constants $\boldsymbol{\alpha}_L$, $\boldsymbol{\beta}_L$, $\boldsymbol{\zeta}_L$ and $\boldsymbol{\eta}_L$ denote the lower bounds for vectors $\boldsymbol{\alpha}$, $\boldsymbol{\beta}$, $\boldsymbol{\zeta}$ and $\boldsymbol{\eta}$, respectively; $\boldsymbol{\alpha}_U$, $\boldsymbol{\beta}_U$, $\boldsymbol{\zeta}_U$ and $\boldsymbol{\eta}_U$ denote the upper bounds for vectors $\boldsymbol{\alpha}$, $\boldsymbol{\beta}$, $\boldsymbol{\zeta}$ and $\boldsymbol{\eta}$, respectively. Note that the sign "$\leqslant$" in Equation (5.17) is overloaded to represent element-wise inequality.

In summary, ω_j and $\boldsymbol{\psi}_{\mathrm{m},j}$ are extracted using experimental data from the sensors deployed on the substructure and interface DOFs at high density, and thus, are constant in the optimization problem. The optimization variables are $\boldsymbol{\alpha}$, $\boldsymbol{\beta}$, $\boldsymbol{\zeta}$, $\boldsymbol{\eta}$ and $\boldsymbol{\psi}_{\mathrm{u}}$. Equation (5.17) leads to a non-convex optimization problem that is generally difficult to solve. However, if mode shapes at unmeasured DOFs, $\boldsymbol{\psi}_{\mathrm{u}}$, were known, Equation (5.17) becomes a convex optimization problem. This is because given $\boldsymbol{\psi}_{\mathrm{u},j}$ is constant, the expression $\left[\tilde{\mathbf{K}}(\boldsymbol{\alpha},\boldsymbol{\zeta}) - \omega_j^2 \tilde{\mathbf{M}}(\boldsymbol{\beta},\boldsymbol{\eta}) \right] \begin{Bmatrix} \boldsymbol{\psi}_{\mathrm{m},j} \\ \boldsymbol{\psi}_{\mathrm{u},j} \end{Bmatrix}$ is an affine function on variables $\boldsymbol{\alpha}$, $\boldsymbol{\beta}$, $\boldsymbol{\zeta}$ and

$\boldsymbol{\eta}$. In addition, the composition of a norm function and an affine function remains convex. Therefore, the objective function in Equation (5.17), which is the summation of convex functions, remains convex [93, 94]. Besides, the lower and upper bound constraints on entries of $\boldsymbol{\alpha}$, $\boldsymbol{\beta}$, $\boldsymbol{\zeta}$ and $\boldsymbol{\eta}$ provide a convex set. When minimizing a convex objective function over a convex set, the optimization problem in Equation (5.17) becomes convex.

Likewise, if system parameters ($\boldsymbol{\alpha}$, $\boldsymbol{\beta}$, $\boldsymbol{\zeta}$ and $\boldsymbol{\eta}$) were known, Equation (5.17) also becomes a convex optimization problem with variable $\boldsymbol{\psi}_u$. Therefore, an iterative linearization procedure for efficiently solving the optimization problem is adopted in this study, similar to [42]. Figure 5.2 shows the pseudo code of the procedure. Each iteration step involves two operations, modal expansion and parameter updating.

(i) Modal expansion

At each iteration step, the operation (i) is essentially modal expansion for unmeasured DOFs, where system parameters ($\boldsymbol{\alpha}$, $\boldsymbol{\beta}$, $\boldsymbol{\zeta}$ and $\boldsymbol{\eta}$) are treated as constant. At the first iteration step, these parameter values are based on initial estimation. At later iteration steps, the parameter values are obtained from model updating results in the previous step. When model parameters are held constant, $\boldsymbol{\psi}_u$ becomes the only optimization variable in Equation (5.17). Arbitrary vector norm functions can be adopted, and the optimization problem can be conveniently coded and efficiently solved using off-the-shelf solvers such as CVX [95]. When Euclidean norm (2-norm) is adopted, the optimization problem without constraints is equivalent to a least square problem. The unknown part of the j-th experimental mode shape vector, $\boldsymbol{\psi}_{u,j}$, can be obtained from following least-square solution.

```
start with α, β, ζ and η = 0 (meaning M and K start with M0 and K0 );
REPEAT {
  (i)  hold α, β, ζ and η as constant and minimize over variable ψu;
  (ii) hold ψu as constant and minimize over variables α, β, ζ and η ;
} UNTIL convergence ;
```

Figure 5.2. Pseudo code of the iterative linearization procedure

$$\begin{bmatrix} \mathbf{D}_{j,\mathrm{mu}} \\ \mathbf{D}_{j,\mathrm{uu}} \end{bmatrix} \boldsymbol{\psi}_{\mathrm{u},j} = -\begin{bmatrix} \mathbf{D}_{j,\mathrm{mm}} \\ \mathbf{D}_{j,\mathrm{um}} \end{bmatrix} \boldsymbol{\psi}_{\mathrm{m},j} \tag{5.18}$$

where definition for $\mathbf{D}_j$ comes from the generalized eigenvalue problem.

$$\begin{bmatrix} \mathbf{D}_{j,\mathrm{mm}} & \mathbf{D}_{j,\mathrm{mu}} \\ \mathbf{D}_{j,\mathrm{um}} & \mathbf{D}_{j,\mathrm{uu}} \end{bmatrix} = \left[\mathbf{D}_j\right] = \tilde{\mathbf{K}}(\boldsymbol{\alpha},\boldsymbol{\zeta}) - \omega_j^2 \tilde{\mathbf{M}}(\boldsymbol{\beta},\boldsymbol{\eta}) \tag{5.19}$$

Here $\tilde{\mathbf{K}}$ and $\tilde{\mathbf{M}}$ are matrices assembled according to Equations (5.15) and (5.16). In operation (i), the matrices are constant because system parameters ($\boldsymbol{\alpha}$, $\boldsymbol{\beta}$, $\boldsymbol{\zeta}$ and $\boldsymbol{\eta}$) are held constant.

(ii) Parameter updating

The operation (ii) at each iteration step is the updating of model parameters ($\boldsymbol{\alpha}$, $\boldsymbol{\beta}$, $\boldsymbol{\zeta}$ and $\boldsymbol{\eta}$) using the expanded complete mode shapes. Thus, $\boldsymbol{\psi}_{\mathrm{u}}$ is held as constant in operation (ii). Again, the optimization problem with $\boldsymbol{\alpha}$, $\boldsymbol{\beta}$, $\boldsymbol{\zeta}$ and $\boldsymbol{\eta}$ as optimization variables can be efficiently solved for an arbitrary vector norm function in Equation (5.17). When 2-norm is adopted, the problem without constraints is equivalent to a least square form shown below.

$$\begin{bmatrix} \mathbf{P}_\alpha & \mathbf{P}_\beta & \mathbf{P}_\zeta & \mathbf{P}_\eta \end{bmatrix} \begin{Bmatrix} \boldsymbol{\alpha} \\ \boldsymbol{\beta} \\ \boldsymbol{\zeta} \\ \boldsymbol{\eta} \end{Bmatrix} = \begin{Bmatrix} \left(\omega_1^2 \tilde{\mathbf{M}}_0 - \tilde{\mathbf{K}}_0\right)\boldsymbol{\psi}_1 \\ \vdots \\ \left(\omega_{n_\mathrm{m}}^2 \tilde{\mathbf{M}}_0 - \tilde{\mathbf{K}}_0\right)\boldsymbol{\psi}_{n_\mathrm{m}} \end{Bmatrix} \tag{5.20}$$

where the matrices $\mathbf{P}_\alpha$, $\mathbf{P}_\beta$, $\mathbf{P}_\zeta$ and $\mathbf{P}_\eta$ are formulated as

$$\mathbf{P}_\alpha = \begin{bmatrix} \mathbf{S}_{\alpha,1}\boldsymbol{\psi}_1 & \cdots & \mathbf{S}_{\alpha,n_\alpha}\boldsymbol{\psi}_1 \\ \mathbf{S}_{\alpha,1}\boldsymbol{\psi}_2 & \cdots & \mathbf{S}_{\alpha,n_\alpha}\boldsymbol{\psi}_2 \\ \vdots & \vdots & \vdots \\ \mathbf{S}_{\alpha,1}\boldsymbol{\psi}_{n_m} & \cdots & \mathbf{S}_{\alpha,n_\alpha}\boldsymbol{\psi}_{n_m} \end{bmatrix} \tag{5.21(a))}$$

$$\mathbf{P}_\zeta = \begin{bmatrix} \mathbf{S}_{\zeta,1}\boldsymbol{\psi}_1 & \cdots & \mathbf{S}_{\zeta,n_i+n_q}\boldsymbol{\psi}_1 \\ \mathbf{S}_{\zeta,1}\boldsymbol{\psi}_2 & \cdots & \mathbf{S}_{\zeta,n_i+n_q}\boldsymbol{\psi}_2 \\ \vdots & \vdots & \vdots \\ \mathbf{S}_{\zeta,1}\boldsymbol{\psi}_{n_m} & \cdots & \mathbf{S}_{\zeta,n_i+n_q}\boldsymbol{\psi}_{n_m} \end{bmatrix} \tag{5.21(b))}$$

$$\mathbf{P}_{\beta} = \begin{bmatrix} -\omega_1^2 \mathbf{S}_{\beta,1}\boldsymbol{\psi}_1 & \cdots & -\omega_1^2 \mathbf{S}_{\beta,n_\beta}\boldsymbol{\psi}_1 \\ -\omega_2^2 \mathbf{S}_{\beta,1}\boldsymbol{\psi}_2 & \cdots & -\omega_2^2 \mathbf{S}_{\beta,n_\beta}\boldsymbol{\psi}_2 \\ \vdots & \vdots & \vdots \\ -\omega_{n_m}^2 \mathbf{S}_{\beta,1}\boldsymbol{\psi}_{n_m} & \cdots & -\omega_{n_m}^2 \mathbf{S}_{\beta,n_\beta}\boldsymbol{\psi}_{n_m} \end{bmatrix} \tag{5.21(c)}$$

$$\mathbf{P}_{\eta} = \begin{bmatrix} -\omega_1^2 \mathbf{S}_{\eta,1}\boldsymbol{\psi}_1 & \cdots & -\omega_1^2 \mathbf{S}_{\eta,n_i+n_q}\boldsymbol{\psi}_1 \\ -\omega_2^2 \mathbf{S}_{\eta,1}\boldsymbol{\psi}_2 & \cdots & -\omega_2^2 \mathbf{S}_{\eta,n_i+n_q}\boldsymbol{\psi}_2 \\ \vdots & \vdots & \vdots \\ -\omega_{n_m}^2 \mathbf{S}_{\eta,1}\boldsymbol{\psi}_{n_m} & \cdots & -\omega_{n_m}^2 \mathbf{S}_{\eta,n_i+n_q}\boldsymbol{\psi}_{n_m} \end{bmatrix} \tag{5.21(d)}$$

Here $\mathbf{S}_{\alpha,j}$, $\mathbf{S}_{\beta,j}$, $\mathbf{S}_{\zeta,j}$ and $\mathbf{S}_{\eta,j}$ represent the constant sensitivity matrices from Equations (5.15) and (5.16). $\boldsymbol{\psi}_j$ is the *j*-th expanded mode containing both measured and unmeasured DOFs.

$$\boldsymbol{\psi}_j = \begin{Bmatrix} \boldsymbol{\psi}_{\mathrm{m},j} \\ \boldsymbol{\psi}_{\mathrm{u},j} \end{Bmatrix} \tag{5.22}$$

5.2.2 Modal Property Difference Approach

For comparison, substructure model updating is also performed through a widely used conventional approach that minimizes experimental and simulated modal property differences [62]. The conventional model updating formulation aims to minimize the difference between experimental and simulated natural frequencies, as well as the difference between experimental and simulated mode shapes of the substructure.

$$\underset{\boldsymbol{\alpha},\boldsymbol{\beta},\boldsymbol{\zeta},\boldsymbol{\eta}}{\text{minimize}} \quad \sum_{j=1}^{n_\mathrm{m}} \left\{ \left(\frac{\omega_j^{\mathrm{FE}} - \omega_j}{\omega_j} \right)^2 + \left(\frac{1-\sqrt{\mathrm{MAC}_j}}{\sqrt{\mathrm{MAC}_j}} \right)^2 \right\} \tag{5.23}$$

where ω_j^{FE} and ω_j represent the *j*-th simulated (from the condensed model in Equations (5.15) and (5.16)) and experimentally extracted frequencies, respectively; MAC_j represents the modal assurance criterion evaluating the difference between the *j*-th simulated and experimental mode shapes. Note that only mode shape entries

corresponding to measured DOFs are compared (i.e. between $\boldsymbol{\psi}_{m,j}^{FE}$ and $\boldsymbol{\psi}_{m,j}$). The optimization variables are $\boldsymbol{\alpha}$, $\boldsymbol{\beta}$, $\boldsymbol{\zeta}$, $\boldsymbol{\eta}$. The mode shapes at unmeasured DOFs, $\boldsymbol{\psi}_{u,j}$, are not among the optimization variables for modal property difference approach, because MAC_j only compares the mode shapes at measured DOFs. A nonlinear least-square optimization solver, `'lsqnonlin'` in MATLAB optimization toolbox [89], is adopted to numerically solve the optimization problem minimizing modal property differences. The optimization solver seeks a minimum through Levenberg-Marquardt algorithm, which adopts a search direction interpolated between the Gauss-Newton direction and the steepest descent direction [96].

5.3 Numerical Validation

To validate the proposed modal dynamic residual approach for substructure model updating, numerical simulations are described in this section [97, 98]. In each simulation example, the modal dynamic residual approach and modal property difference approach are compared. For each approach, the updating is performed assuming different numbers of measured modes are available (i.e. modes corresponding to the 3~6 lowest natural frequencies). Section 5.3.1 describes substructure model updating on a lumped spring-mass model. Section 5.3.2 describes a plane truss model. Section 5.3.3 describes a plane frame model and Section 5.3.5 describes a space frame model.

5.3.1 Lumped Spring-Mass Model

Figure 5.3 shows a 200-DOF spring-mass model for validating the proposed substructure updating approach. In the initial model (as starting point of model updating), all the mass and spring stiffness values are set identically as 6kg and 35kN/m, respectively. To construct the actual model as updating goal, damage is introduced to this model by reducing 10% of spring stiffness at k_{20}, k_{30}, k_{45}, k_{50}, k_{60}, k_{62}, k_{82}, k_{100}, k_{120}, and

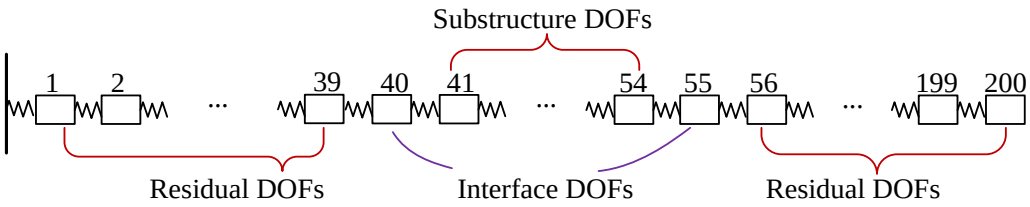

Figure 5.3. Illustration of substructure selection (10% stiffness reduction is introduced to k_{20}, k_{30}, k_{45}, k_{50}, k_{60}, k_{62}, k_{82}, k_{100}, k_{120}, and k_{150} as damage)

k_{150}. A substructure with DOFs from 41 to 54 ($\mathbf{x}_s \in \mathbb{R}^{14\times1}$) is selected for model updating. As a result, DOFs 40 and 55 are interface DOFs ($\mathbf{x}_i \in \mathbb{R}^{2\times1}$). All other DOFs belong to the residual structure. The initial stiffness, actual stiffness, and expected model updating changes are listed in TABLE 5.1. Note that two springs with stiffness loss, k_{45} and k_{50}, are contained in the substructure. It is assumed all substructure and interface DOFs are instrumented with sensors for experimentally capturing substructure vibration modes. No measurement is required on the residual structure.

For modeling, dynamic response of the residual structure is approximated using twenty modal coordinates, i.e. $n_q = 20$ (Equation (5.3)). With $\mathbf{x}_s \in \mathbb{R}^{14\times1}$ and $\mathbf{x}_i \in \mathbb{R}^{2\times1}$, the entire structural model is therefore condensed to 36 DOFs. Without loss of generality, accurate structural mass matrix is assumed to be known, so mass parameters $\boldsymbol{\beta}$ (Equation (5.16)) is not among the updating parameters. The selected updating parameters are the stiffness parameters $\boldsymbol{\alpha}$ (k_{41}, k_{42}, ..., and k_{55} in the substructure), and modal parameters of the residual structural with free interface (ζ_2, ζ_3, ..., ζ_{22} and η_1, η_2, ..., η_{22}). Note that n_q+n_i

TABLE 5.1. Structural properties in the selected substructure

Updating parameter	k_{41}	k_{42}	k_{43}	k_{44}	k_{45}	k_{46}	k_{47}	k_{48}	k_{49}	k_{50}	k_{51}	k_{52}	k_{53}	k_{54}	k_{55}
Initial value (kN/m)	35	35	35	35	35	35	35	35	35	35	35	35	35	35	35
Actual value (kN/m)	35	35	35	35	31.5	35	35	35	35	31.5	35	35	35	35	35
Change (%)	0	0	0	0	-10	0	0	0	0	-10	0	0	0	0	0

= 22 and that the modal parameter ζ_1 is not included, because the first resonance frequency of the residual structure with free interface is zero (corresponding to free-body movement). As a result, the first modal correction matrix $\tilde{\mathbf{K}}_{R0,1}$ in Equation (5.15) is a zero matrix, and so is the corresponding sensitivity matrix $\mathbf{S}_{\zeta,1}$. Using modal frequencies and substructure mode shapes of the structure with damage (ω_j and $\boldsymbol{\psi}_{\mathrm{m},j}$) as "experimental data", both the proposed modal dynamic residual approach and the conventional modal property difference approach are applied for substructure model updating.

TABLE 5.2 summarizes the updating results using the proposed modal dynamic residual approach for substructure model updating. With different numbers of available modes, the updated values for k_{45} and k_{50} are exactly -10.0% and -10.0%. The updated values for all other k_i are exactly zero, which implies no change in all other stiffness values in the substructure. Therefore, the updating results achieve the goal (shown in

TABLE 5.2. Updated parameter changes (%) for substructure elements on the lumped spring-mass model by minimization of modal dynamic residuals

Available modes	k_{41}	k_{42}	k_{43}	k_{44}	k_{45}	k_{46}	k_{47}	k_{48}	k_{49}	k_{50}	k_{51}	k_{52}	k_{53}	k_{54}	k_{55}
3 modes	0.00	0.00	0.00	0.00	-10.00	0.00	0.00	0.00	0.00	-10.00	0.00	0.00	0.00	0.00	0.00
4 modes	0.00	0.00	0.00	0.00	-10.00	0.00	0.00	0.00	0.00	-10.00	0.00	0.00	0.00	0.00	0.00
5 modes	0.00	0.00	0.00	0.00	-10.00	0.00	0.00	0.00	0.00	-10.00	0.00	0.00	0.00	0.00	0.00
6 modes	0.00	0.00	0.00	0.00	-10.00	0.00	0.00	0.00	0.00	-10.00	0.00	0.00	0.00	0.00	0.00

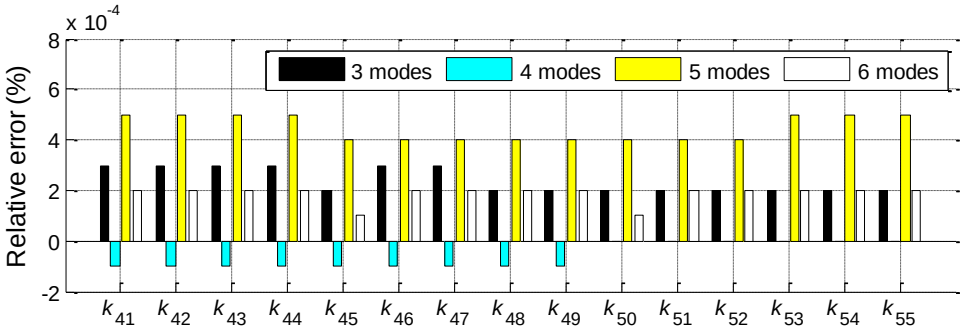

Figure 5.4. Relative errors of the updated parameters on the lumped spring-mass model by minimization of modal dynamic residuals

TABLE 5.1) and correctly identify the damage locations and severities. Figure 5.4 plots the relative errors of the updating results, i.e. deviation of updated stiffness values from the actual values, for different numbers of available modes. The figure also shows that the updating results accurately identify all substructure properties, because all the updating errors are less than 0.0005%.

Similarly, TABLE 5.3 summarizes the updating results using the conventional modal property difference approach. The overall damage detection performance is obviously worse than the modal dynamic residual approach. Figure 5.5 shows the relative errors of the updating results, as compared to the actual values. The maximum relative error for conventional modal property difference approach is 3.3% for parameter k_{45} (with three available modes). Therefore, the conventional approach shows worse performance than the proposed modal dynamic residual approach.

TABLE 5.3. Updated parameter changes (%) for substructure elements on the lumped spring-mass model by minimization of modal property differences

Available modes	k_{41}	k_{42}	k_{43}	k_{44}	k_{45}	k_{46}	k_{47}	k_{48}	k_{49}	k_{50}	k_{51}	k_{52}	k_{53}	k_{54}	k_{55}
3 modes	-0.10	0.03	-0.37	-1.93	-6.69	-1.84	-0.30	-0.28	-1.82	-6.83	-1.91	-0.33	0.09	0.09	-0.15
4 modes	0.25	0.32	0.37	-0.16	-9.50	-0.11	0.31	0.26	0.02	-9.73	0.05	0.23	0.14	0.17	0.14
5 modes	0.57	0.91	0.76	-0.64	-7.89	-0.56	0.89	0.88	-0.62	-7.70	-0.70	0.78	1.04	0.95	0.07
6 modes	0.61	1.32	1.35	1.33	-8.77	1.37	1.42	1.44	1.44	-8.66	1.47	1.54	1.50	1.54	1.73

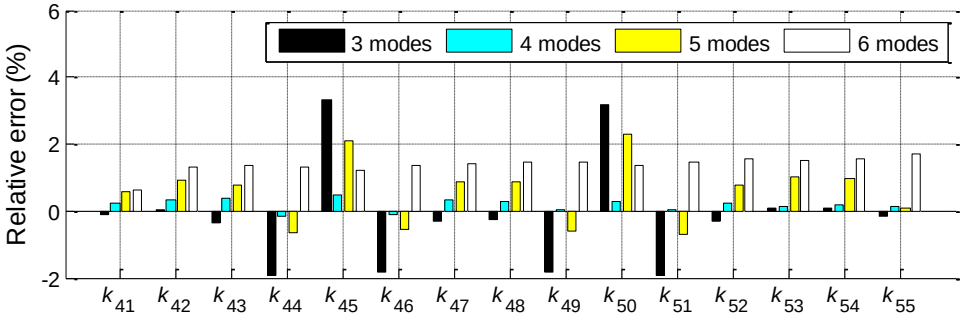

Figure 5.5. Relative errors of the updated parameters on the lumped spring-mass model by minimization of modal property differences

5.3.2 Plane Truss Model

Figure 5.6 shows the plane truss model for validating the proposed substructure updating approach. The truss model has 26 nodes, and each node has two translational DOFs. Horizontal and vertical springs (k_{x1} and k_{y1}) are allocated at the left support to simulate a non-ideal hinge, while a vertical spring (k_{y2}) is allocated at the right support to simulate a non-ideal roller. TABLE 5.4 summarizes the structural properties of the model, including elastic modulus E_1 of top-level truss bars, modulus E_2 of diagonal and vertical bars, modulus E_3 of bottom bars, and three spring stiffness numbers. The table provides initial nominal values for all parameters, as starting point for model updating. The table also lists actual values, which ideally are to be identified. The relative changes from initial to actual values are also listed.

A substructure containing first three truss units from left is selected for model updating (Figure 5.6). The selected substructure contains six substructure nodes and two interface nodes. Each node includes two translational DOFs. The substructure DOF vector is $\mathbf{x}_s \in \mathbb{R}^{12\times1}$ and the interface DOF vector is $\mathbf{x}_i \in \mathbb{R}^{4\times1}$. It is assumed all substructure and interface DOFs are instrumented with sensors for experimentally capturing substructure vibration modes. No measurement is required on the residual

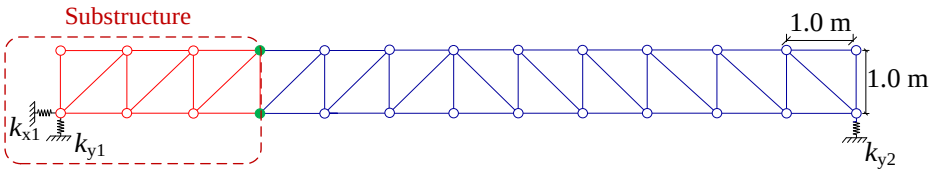

Figure 5.6. Illustration of substructure selection of a plane truss

TABLE 5.4. Structural properties of the plane truss

Updating parameter	Steel elastic modulus (10^{11} N/m^2)			k_{x1} (10^6 N/m)	k_{y1} (10^6 N/m)	k_{y2} (10^6 N/m)
	Top (E_1)	Diag. & Vert. (E_2)	Bottom (E_3)			
Initial value	2	2	2	5	5	5
Actual value	2.2	2.1	1.9	2	7	7
Change (%)	10	5	-5	-60	40	40

structure. For modeling, dynamic response of the residual structure is approximated using ten modal coordinates, i.e. $n_q = 10$ in Equation (5.3). As a result, the entire structural model is condensed to $n_s+n_i+n_q=26$ DOFs (from 52 DOFs in the original structure). Without loss of generality, accurate structural mass matrix is assumed to be known, so mass parameters ($\boldsymbol{\beta}$ in Equation (5.16)) are not among the updating parameters. The substructure stiffness parameters $\boldsymbol{\alpha}$ (being updated) include the three elastic moduli in the substructure (E_1, E_2, and E_3), as well as the spring stiffness values at the left support (k_{x1} and k_{y1}). Because the spring stiffness at the right support, k_{y2}, only contributes to residual structure, k_{y2} cannot be updated. Instead, the residual structure is updated through modal parameters of the residual structure with free interface (ζ_2, ζ_3, ..., ζ_{14} and η_1, η_2, ..., η_{14}). Note that $n_i+n_q = 14$ and that the modal parameters ζ_1 is not included, because the first resonance frequency of the residual structure with free interface is zero, similar as in Section 5.3.1. Again, using modal frequencies and substructure mode shapes (ω_j and $\boldsymbol{\psi}_{m,j}$) of the simulated actual structure as "experimental data", both the proposed modal dynamic residual approach and the conventional modal property difference approach are applied for substructure model updating.

TABLE 5.5 summarizes the updating results using the proposed modal dynamic residual approach for substructure model updating. The results are presented in terms of relative change percentages from initial values. For every available number of modes, the updating parameter changes are close to the ideal percentages listed in TABLE 5.4.

TABLE 5.5. Updated parameter changes (%) for substructure elements on the plane truss model by minimization of modal dynamic residuals

Available modes	Steel elastic modulus change (%)			Change in k_{x1} (%)	Change in k_{y1} (%)
	Top (E_1)	Diag. & Vert. (E_2)	Bottom (E_3)		
3 modes	10.08	5.03	-5.02	-60.00	40.04
4 modes	9.99	5.00	-5.00	-60.00	40.00
5 modes	9.99	4.99	-4.98	-60.00	39.99
6 modes	10.04	4.99	-4.98	-60.00	39.99

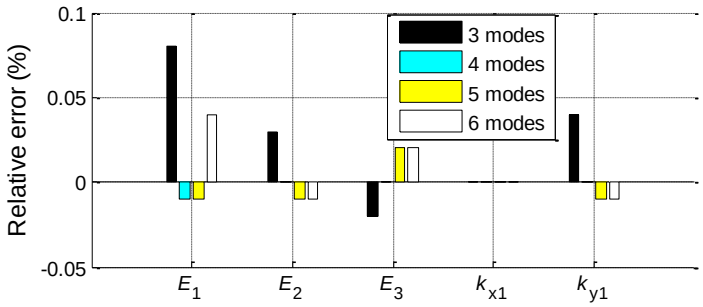

Figure 5.7. Relative errors of the updated parameters on the plane truss model by minimization of modal dynamic residuals

Figure 5.7 plots the relative errors of the updating results, i.e. deviation of updated stiffness values from the actual values, for different numbers of available modes. The figure shows that the updating results accurately identify all substructure properties, and the maximum updating error is a negligible 0.08% for parameter E_1 (when only three modes are available).

Similarly, TABLE 5.6 summarizes the updating results using the conventional modal property difference approach. The updated parameter changes are apparently different from the ideal percentages listed in TABLE 5.4. Figure 5.8 shows the relative errors of the updating results, as compared to the actual values. The conventional approach can update some structural properties to a fairly good accuracy, but the results are generally worse than the proposed modal dynamic residual approach. The maximum error for conventional modal property difference approach is -7.98% for parameter E_1 (with five available modes).

TABLE 5.6. Updated parameter changes (%) for substructure elements on the plane truss model by minimization of modal property differences

Available modes	Steel elastic modulus change (%)			Change in k_{x1} (%)	Change in k_{y1} (%)
	Top (E_1)	Diag. & Vert. (E_2)	Bottom (E_3)		
3 modes	5.23	2.84	-7.86	-60.2	37.02
4 modes	7.71	4.59	-4.58	-58.44	38.90
5 modes	2.03	7.70	-5.88	-57.82	38.23
6 modes	4.33	7.74	0.16	-55.43	41.11

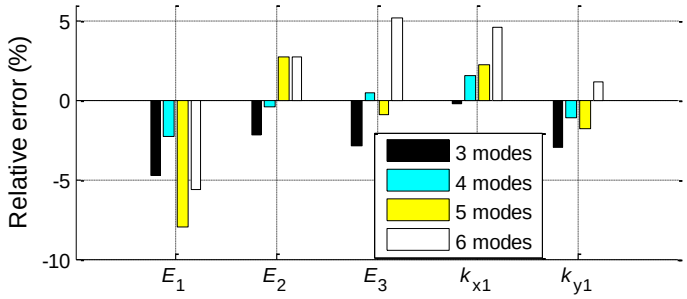

Figure 5.8. Relative errors of the updated parameters on the plane truss model by minimization of modal property differences

5.3.3 Plane Frame Model

Figure 5.9 shows the plane portal frame model. The frame model contains 42 elements and 131 DOFs in total. The portal frame has a pin support on each side. Distinct elastic moduli are assigned along frame members as actual values (Figure 5.9). For example, lower-left corner of the substructure has four elements with the same modulus 0.8E; the upper eight elements at left column have the same modulus 1.0E. In the initial model as starting point of model updating, it is assumed that the same elastic modulus (E) is assigned to all elements.

A substructure at the upper right corner, containing 14 elements, is selected for model updating. The selected substructure contains 13 substructure nodes and 2 interface nodes. Each node has two translational DOFs and one rotational DOF, so the substructure

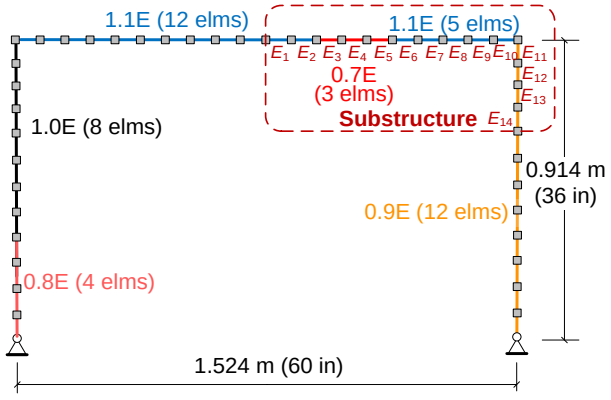

Figure 5.9. Illustration of substructure selection of a plane portal frame

DOF vector $\mathbf{x}_s \in \mathbb{R}^{39\times1}$ and the interface DOF vector $\mathbf{x}_i \in \mathbb{R}^{6\times1}$. It is assumed only translational DOFs at substructure and interface nodes are instrumented with accelerometers for experimentally capturing substructure vibration modes; rotational DOFs are not measured. Again, no measurement is required on the residual structure. Dynamic response of the residual structure is approximated using ten modal coordinates, i.e. $n_q = 10$ in Equation (5.3). As a result, the entire structural model is condensed to $n_s+n_i+n_q$=55 DOFs (from 131 DOFs in the original structure). Similar to previous examples, mass parameters $\boldsymbol{\beta}$ is not among the updating variables. The selected updating parameters are the stiffness parameters $\boldsymbol{\alpha}$ (the 14 different elastic moduli of the 14 substructure elements), and modal parameters of the residual structure with free interface (ζ_3, ζ_4, ..., ζ_{16} and η_1, η_2, ..., η_{16}). Note that $n_i+n_q = 16$ and that the modal parameters ζ_1 and ζ_2 are not included, because the first two resonance frequencies of the residual structure with free interface are zero, similar as in Section 5.3.1. Again, using modal frequencies and substructure mode shapes (ω_j and $\boldsymbol{\psi}_{\mathrm{m},j}$) of the simulated damaged structure as "experimental data", both the proposed modal dynamic residual approach and the conventional modal property difference approach are applied for substructure model updating.

TABLE 5.7 summarizes the updating results using the proposed modal dynamic residual approach for substructure model updating. The results are presented in terms of relative change percentage from initial values. Similar to the previous examples, for

TABLE 5.7. Updated parameter changes (%) for substructure elements on the plane frame model by minimization of modal dynamic residuals

Available modes	E_1	E_2	E_3	E_4	E_5	E_6	E_7	E_8	E_9	E_{10}	E_{11}	E_{12}	E_{13}	E_{14}
3 modes	10.59	10.29	-29.92	-29.93	-29.95	10.08	10.05	10.06	10.04	10.06	-9.97	-9.95	-9.95	-9.95
4 modes	14.12	13.21	-28.63	-28.62	-28.82	11.86	11.69	11.73	11.64	11.69	-8.66	-8.58	-8.58	-8.53
5 modes	10.67	10.60	-29.94	-29.89	-29.97	10.10	10.01	10.07	10.02	10.05	-9.98	-9.96	-9.98	-10.02
6 modes	13.16	12.46	-29.08	-29.07	-29.30	10.98	10.84	10.78	10.70	10.67	-9.47	-9.48	-9.47	-9.41

every available number of modes, the updating parameter changes are fairly close to the ideal percentages that can be easily calculated from Figure 6, element by element in the substructure. For example, the correct/ideal change should be 10% for E_1, 10% for E_2, -30% for E_3, etc. Figure 5.10 plots the relative errors of the updating results as compared to the actual values, for different numbers of available modes. The proposed approach can correctly identify most of the structural parameters. The larger errors are with E_1 and E_2, which are close to an interface node. The maximum error is 4.12% (when four modes are available), which is higher than the maximum error in previous plane truss example in Section 5.3.2. Nevertheless, in most scenarios, the majority of the parameters can be identified within 2% error. Note that in this frame example, only translational DOFs of the substructure and interface nodes are measured; rotational DOFs are unmeasured, as commonly encountered in practice. In the plane truss example, no rotational DOFs exist, so all DOFs on substructure and interface nodes are measured. This can be the reason that the updating results in this frame example are less accurate than the results in the truss example.

TABLE 5.8 summarizes the updating results using the conventional modal property difference approach. The updated parameter changes are apparently different from the correct/ideal values. Figure 5.11 plots the relative errors of the updating results as compared to the actual values. The figure shows that the updating results from conventional approach have much larger errors than the results from the proposed modal

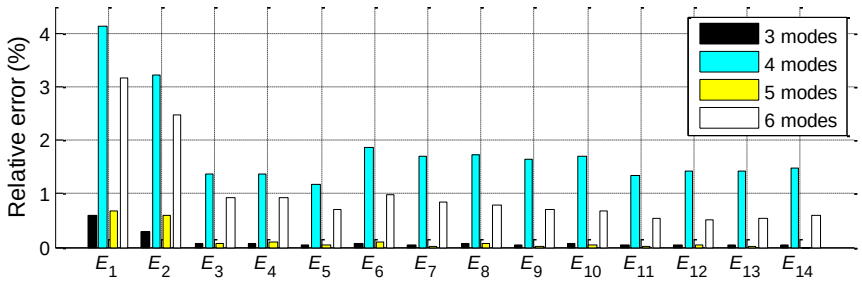

Figure 5.10. Relative errors of the updated parameters on the plane frame model by minimization of modal dynamic residuals

TABLE 5.8. Updated parameter changes (%) for substructure elements on the plane frame model by minimization of modal property differences

Available modes	E_1	E_2	E_3	E_4	E_5	E_6	E_7	E_8	E_9	E_{10}	E_{11}	E_{12}	E_{13}	E_{14}
3 modes	-0.96	-2.18	-3.41	-5.62	-4.26	-2.52	0.02	1.81	2.07	1.14	-0.39	-1.75	-2.04	-1.29
4 modes	0.42	0.05	-0.26	-1.25	-0.82	-1.50	-1.26	-0.48	-0.17	0.43	0.48	0.44	-0.43	-0.61
5 modes	1.15	-0.88	-4.18	-10.79	-10.02	-7.00	-2.31	2.46	0.94	-4.88	-9.78	-6.62	-2.99	0.11
6 modes	4.85	0.28	-1.91	-3.83	-4.49	-2.09	-0.68	-0.56	0.45	-0.02	-1.80	-1.41	-0.27	-1.14

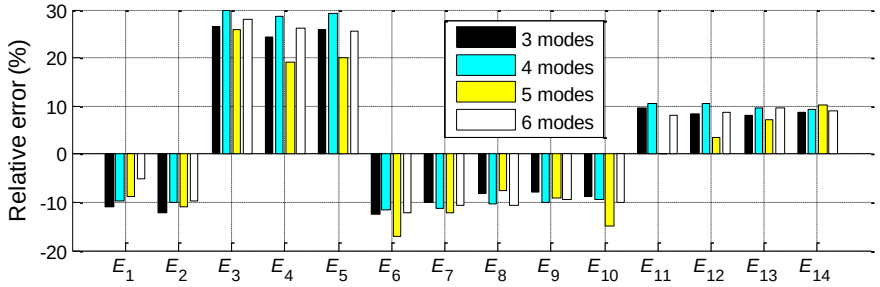

Figure 5.11. Relative errors of the updated parameters on the plane frame model by minimization of modal property differences

dynamic residual approach (Figure 5.10). It can be concluded that the conventional approach minimizing modal property differences, when used for substructure model updating, cannot achieve a reasonable accuracy in this example.

5.3.4 Space Frame Model

Figure 5.12 shows the numerical model of a space frame bridge. The space frame model contains 46 nodes, each node with six DOFs. Although mainly a frame structure, the segment cross bracings in top plane and two side planes are truss members. Transverse and vertical springs (k_y and k_z) are allocated at both ends of the frame

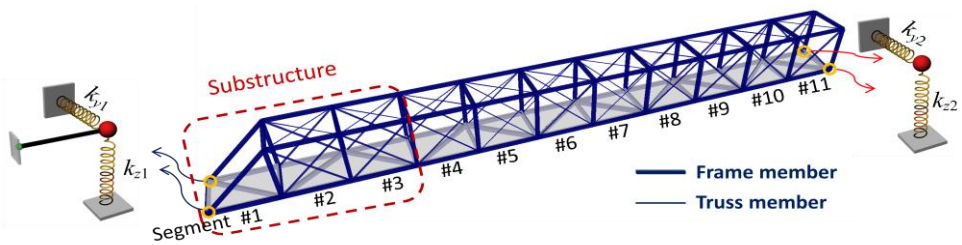

Figure 5.12. Illustration of substructure selection of a space frame bridge

structure to simulate non-ideal boundary conditions. In this study, it is assumed to have accurate information on structural mass; structural stiffness parameters are to be updated. TABLE 5.9 summarizes the structural stiffness parameters of the model. The parameters are divided into three categories. The first category contains six parameters (starting from top in the table), which are elastic moduli of the frame and truss (diagonal bracings in top plane) members along the entire length of the frame structure. The second category contains ten parameters, which are the elastic moduli of truss members (diagonal bracings in two side planes) for different segments. The third category contains stiffness parameters of the four types of support springs. TABLE 5.9 provides initial (nominal) values for all parameters, as starting point for model updating. The table also lists actual values, which ideally are to be identified. Note that the actual values are just simply assumed for the purpose of demonstration. The relative changes from initial to actual values, to be identified, are also listed.

TABLE 5.9. Structure stiffness parameters

Updating parameters			Initial value	Actual value	Change (%)
Elastic moduli of members along the frame structure (kips/in^2)	Frame members	E_1 – Longitudinal top chord	29,000	30,450	5
		E_2 – Longitudinal bottom chord	29,000	30,450	5
		E_3 – Vertical members	29,000	27,550	-5
		E_4 – Transverse top chord	29,000	26,100	-10
		E_5 – Transverse & diagonal bottom chord	29,000	30,450	5
	Truss members	E_6 – Diagonal bracings in top plane	29,000	27,550	-5
Elastic moduli of side-plane diagonal bracings (truss members) for each segment (kips/in^2)	E_{S2} – 2nd segment		29,000	26,100	-10
	E_{S3} – 3rd segment		29,000	26,100	-10
	E_{S4} – 4th segment		29,000	26,100	-10
	E_{S5} – 5th segment		29,000	27,550	-5
	E_{S6} – 6th segment		29,000	27,550	-5
	E_{S7} – 7th segment		29,000	27,550	-5
	E_{S8} – 8th segment		29,000	24,650	-15
	E_{S9} – 9th segment		29,000	26,100	-10
	E_{S10} – 10th segment		29,000	27,550	-5
	E_{S11} – 11th segment		29,000	27,550	-5
Support springs (kips/in)	k_{y1} – Left transverse		200	140	-30
	k_{z1} – Left vertical		500	800	60
	k_{y2} – Right transverse		200	140	-30
	k_{z2} – Right vertical		500	800	60

A substructure containing first three segments from left is selected for model updating (Figure 5.12). The selected substructure contains 10 substructure nodes and 4 interface nodes. Since each node has six DOFs and the longitudinal DOFs of the two support nodes are constrained, the substructure DOF vector is $\mathbf{x}_s \in \mathbb{R}^{58\times1}$ and the interface DOF vector is $\mathbf{x}_i \in \mathbb{R}^{24\times1}$. For practicality, it is assumed only translational DOFs of the substructure and interface nodes are instrumented with accelerometers for capturing substructure vibration modes; rotational DOFs are not measured. No measurement is required on the residual structure. For model condensation, dynamic response of the residual structure is approximated using twenty modal coordinates, i.e. n_q = 20 in Equation (5.3). As a result, the entire structural model is condensed to $n_s+n_i+n_q=102$ DOFs (reduced from 274 DOFs in the original structure).

Since accurate structural mass matrix is assumed to be known, mass parameters $\boldsymbol{\beta}$ is not among the updating parameters. Figure 5.13 shows the detailed view of the substructure containing the first three segments. The substructure stiffness parameters $\boldsymbol{\alpha}$ (being updated) include the five elastic moduli of the frame members (E_1~E_5), the elastic moduli of top bracing truss members (E_6), the elastic moduli of side-bracing truss

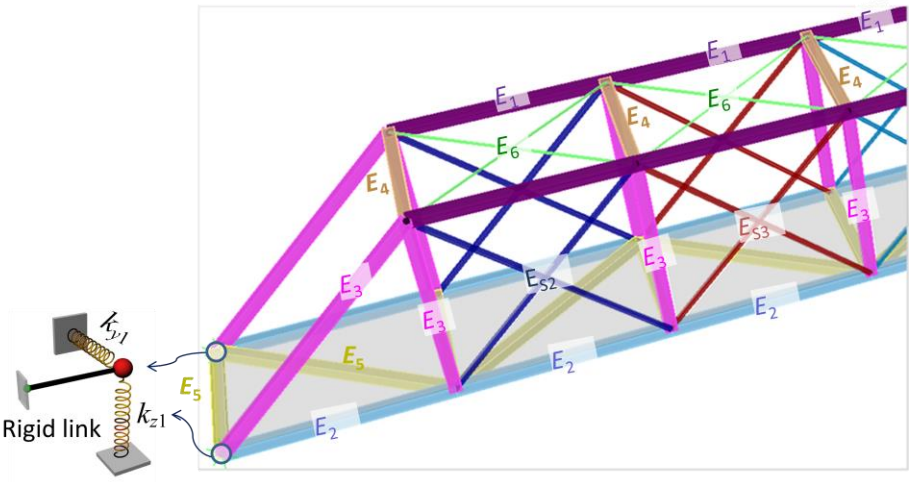

Figure 5.13. Detailed view of the substructure showing stiffness parameters to be updated

members at the 2nd and 3rd segments (E_{S2} and E_{S3}), and the spring stiffness values at the left support (k_{y1} and k_{z1}). On the other hand, the residual structure is updated through modal parameters of the residual structure with free interface (ζ_2, ζ_3, ..., ζ_{44} and η_1, η_2, ..., η_{44}). Note that $n_i+n_q = 44$ and that modal parameter ζ_1 is not included because the first resonance frequency of the residual structure with free interface is zero, similar as previous examples. Using modal frequencies and substructure mode shapes of the simulated actual structure (ω_j and $\boldsymbol{\psi}_{m,j}$) as "experimental data", both updating approaches are applied for substructure model updating.

TABLE 5.10 summarizes the updating results using the proposed modal dynamic residual approach for substructure model updating. The results are presented in terms of relative change percentages from initial values. For every available number of modes, most of the updated parameter changes are close to the ideal percentages listed in TABLE 5.9. The updating results for E_4, the elastic moduli of the transverse frame members in top plane, are between -5.90% (with 5 modes) and -5.48% (with four available modes). These results are most different from the actual/ideal change of -10%. The reason is this parameter is less sensitive to translational DOFs. For verification, a sensitivity analysis is performed to each stiffness parameter around of initial parameter values. Due to page limit, Figure 5.14 shows the sensitivity plots of two updating parameters, E_4 and E_6. For each sensitivity plot, the objective function (Equation (5.17)) is calculated by changing one selected parameter from -20% to +20%, while keeping all other parameters at initial values. The plots show that the objective function varies within the a smaller range

TABLE 5.10. Updated parameter changes (%) for substructure elements on the space frame model by minimization of modal dynamic residuals

Available modes	Frame member					Truss member			Spring	
	E_1	E_2	E_3	E_4	E_5	E_6	E_{S2}	E_{S3}	k_{y1}	k_{z1}
3 modes	4.21	4.17	-5.61	-5.76	4.16	-6.24	-10.68	-10.94	-30.54	59.01
4 modes	4.70	4.65	-5.08	-5.48	4.64	-5.61	-10.26	-10.61	-30.21	59.90
5 modes	4.91	5.00	-5.05	-5.90	4.99	-5.16	-10.05	-10.48	-29.99	59.94
6 modes	4.73	4.39	-5.10	-5.65	4.36	-6.39	-10.32	-12.11	-30.43	59.83

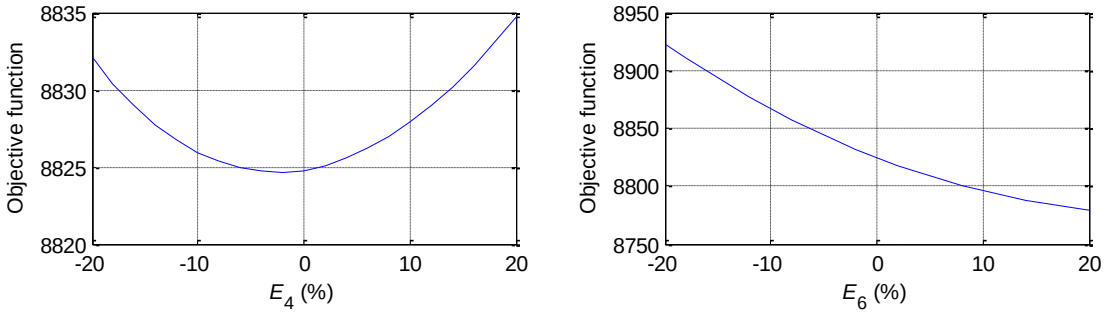

Figure 5.14. Sensitivities of the updated parameters to the objective function

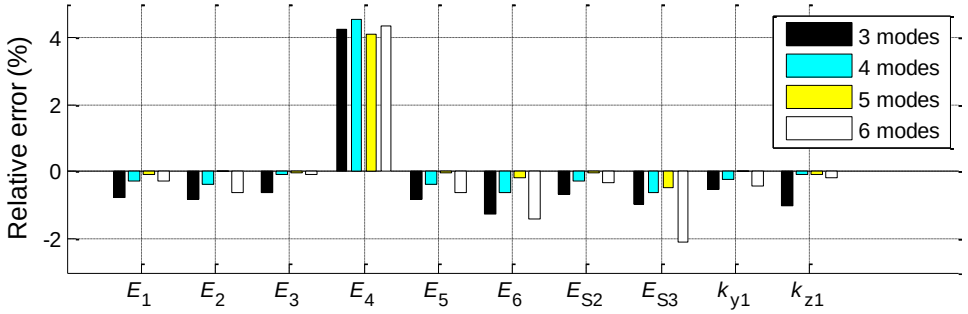

Figure 5.15. Relative errors of the updated parameters on the space frame model by minimization of modal dynamic residuals

(8825~8835) for E_4, while within a much larger range (8782~8924) for E_6. The comparison indicates that E_4 is not a sensitive updating parameter. For clear demonstration of the updating accuracy, Figure 5.15 plots the relative errors of the updating results, i.e. relative difference of updated values from the actual parameter values, for different numbers of available modes. The figure shows that except for E_4, the updating results accurately identify all other substructure stiffness parameters. In addition, the updating accuracy generally improves when more measured modes are available.

TABLE 5.11 summarizes the updating results using the conventional approach minimizing modal property differences. Many of the updated/identified parameter changes are apparently different from the correct/ideal values listed in TABLE 5.9. For clear demonstration of updating accuracy, Figure 5.16 plots the relative errors of the updating results. The figure shows that the updating results from conventional approach

TABLE 5.11. Updated parameter changes (%) for substructure elements on the space frame model by minimization of modal property differences

Available modes	Frame member					Truss member			Spring	
	E_1	E_2	E_3	E_4	E_5	E_6	E_{S2}	E_{S3}	k_{y1}	k_{z1}
3 modes	3.21	5.89	-4.68	-2.40	1.77	-4.25	-3.12	-2.74	0.02	0.00
4 modes	3.60	5.18	-5.71	-3.53	1.64	-5.60	-3.06	-2.97	0.02	0.02
5 modes	4.78	6.83	-5.01	-4.87	3.73	-2.49	-1.49	-1.21	0.05	0.06
6 modes	6.93	6.42	-5.58	-8.25	3.53	-4.69	-2.84	-2.72	-0.22	0.13

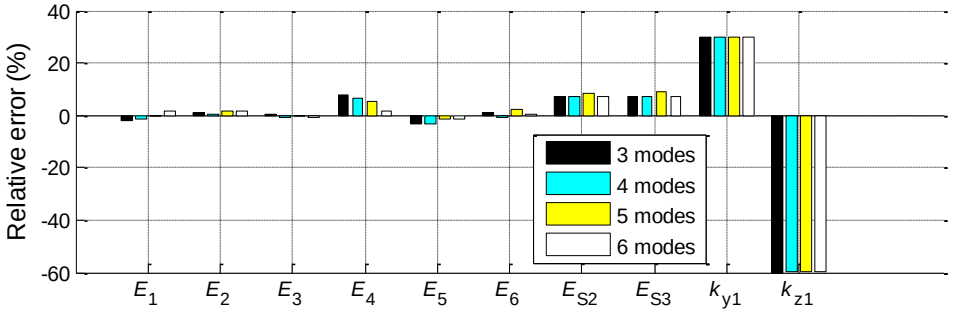

Figure 5.16. Relative errors of the updated parameters on the space frame model by minimization of modal property differences

have much larger errors than the results from the proposed modal dynamic residual approach (Figure 5.15), particularly for stiffness parameters k_{y1} and k_{z1} of the support spring. The conventional approach minimizing modal property differences, when used for substructure model updating, cannot achieve a reasonable accuracy in this example.

5.3.5 Discussion of Model Updating Results

The numerical simulations in this section demonstrate that the proposed substructure updating approach minimizing modal dynamic residuals is capable of accurately identifying most parameters in the substructure. Meanwhile, when the conventional approach minimizing modal property differences is applied, the updating process either generates results with much lower accuracy (Section 5.3.1 and Section 5.3.2), or cannot achieve a reasonable solution at all for some parameters (Section 5.3.3 and Section 5.3.4). The main reason is likely that the objective function in the modal property difference approach is less sensitive to minor changes in structural parameters.

It should be noted that the solutions given by the proposed modal dynamic residual approach still show small errors. The errors are mainly caused by the approximations made in the model condensation process for substructure model updating. First, the Craig-Bampton transform used in model condensation adopts the static condensation matrix as the transformation matrix from interface DOFs to residual DOFs (Equation (5.3)), which neglects interface dynamic contribution. Second, the Craig-Bampton transform uses only a few dominant modes describing dynamic behavior of the residual structure; higher-frequency modes are neglected. Third, while updating modal parameters for the residual structure, it is assumed that potential physical parameter changes in the residual structure do not significantly alter the generalized eigenvectors of the residual structural matrices (Equation (5.11)). Nevertheless, the overall substructure updating performance through minimization of modal dynamic residuals is reasonably accurate.

5.4 Investigations on Substructure Location and Size

This section continues investigating the performance of the proposed substructure model updating approach. Three subjects of interest are studied, including performance comparison with model updating of entire structure, performance evaluation with respect to substructure location, and performance evaluation with respect to substructure size. The space frame example (Figure 5.12 and TABLE 5.9) in Section 5.3.4 is adopted in the study.

5.4.1 Performance Comparison with Model Updating of Entire Structure

To gain more perspective on the proposed substructure model updating, model updating of the entire structure is performed. It is assumed that 14 tri-axial accelerometers, the same amount as used for the substructure updating in Section 5.3.4,

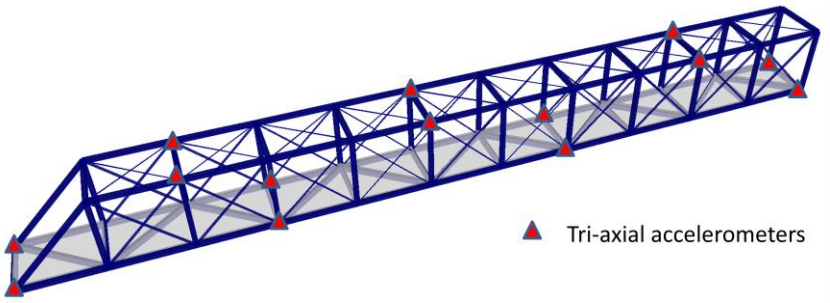

Figure 5.17. Uniform sensor instrumentation on the entire structure

are adopted for model updating of entire structure. The 14 accelerometers are instrumented uniformly on the entire structure, as shown in Figure 5.17.

The model updating of entire structure is performed to minimize modal dynamic residuals of the generalized eigenvalue equation:

$$\begin{aligned} &\underset{\boldsymbol{\alpha},\boldsymbol{\beta},\boldsymbol{\psi}_{\mathrm{u}}}{\text{minimize}} \quad && \sum_{j=1}^{n_{\mathrm{m}}} \left\| \left[\mathbf{K}(\boldsymbol{\alpha}) - \omega_j^2 \mathbf{M}(\boldsymbol{\beta}) \right] \begin{Bmatrix} \boldsymbol{\psi}_{\mathrm{m},j} \\ \boldsymbol{\psi}_{\mathrm{u},j} \end{Bmatrix} \right\|^2 \\ &\text{subject to} \quad && \boldsymbol{\alpha}_L \le \boldsymbol{\alpha} \le \boldsymbol{\alpha}_U ; \quad \boldsymbol{\beta}_L \le \boldsymbol{\beta} \le \boldsymbol{\beta}_U \end{aligned} \tag{5.24}$$

where **K** and **M** are stiffness and mass matrices of the entire structure; other notations are defined same as those in Equation (5.17). Note that only physical parameters **α** and **β**, together with unmeasured mode shape DOFs, are the optimization variables.

The same iterative linearization procedure (Figure 5.2) is adopted to solve the optimization problem. Every iteration step contains two operations, i.e. modal expansion and parameter updating. In this simulation, it is assumed to have accurate information on structural mass, and that structural stiffness parameters are to be updated. The updating parameters **α** are the same as the parameters list in TABLE 5.9.

TABLE 5.12 summarizes the updating results for model updating of entire structure. The results are presented in terms of relative change percentages from initial values. For every available number of modes, most of the updated parameter changes are close to the ideal percentages listed in TABLE 5.9, while some updated parameter changes have large deviation from the actual/ideal changes. For example, the updating

value for E_3, the elastic moduli of the vertical frame members, is between -0.14% (with 5 modes) and +1.17% (with 4 modes), while its actual/ideal change is -5%. In addition, the updating results for E_{S2}, the elastic moduli of the side bracings for the 2nd segment, are around -15% ~ -18% for different numbers of available modes, while its actual/ideal change is -10%. Note that E_4, the elastic moduli of the transverse frame members in top plane, is also not sensitive to in the model updating of the entire structure, when only translational DOFs are measured. Thus, E_4 is excluded in the followed comparison.

To compare with the substructure updating results in Figure 5.12 from Section 5.3.4, Figure 5.18 plots the relative updating errors for the physical parameters in the entire structure, with different numbers of available modes. The comparison shows that with same amount of accelerometer channels, the accuracy of substructure updating

TABLE 5.12. Updated stiffness parameter changes (%) for the entire structure by minimization of modal dynamic residuals

Available modes	**Frame member**					**Spring**			
	E_1	E_2	E_3	E_4	E_5	k_{y1}	k_{z1}	k_{y1}	k_{z2}
3 modes	4.58	4.22	0.62	-0.26	3.56	-30.87	62.67	-30.27	61.96
4 modes	5.19	4.67	1.17	0.63	3.62	-30.48	64.29	-29.19	63.49
5 modes	4.83	4.87	-0.14	-1.44	3.05	-30.89	61.24	-29.52	60.76
6 modes	5.00	4.99	0.31	-0.77	3.18	-30.85	61.66	-29.86	61.93

Available modes	**Truss member**										
	E_6	E_{S2}	E_{S3}	E_{S4}	E_{S5}	E_{S6}	E_{S7}	E_{S8}	E_{S9}	E_{S10}	E_{S11}
3 modes	-5.54	-16.38	-10.80	-12.63	-4.32	-7.11	-5.85	-16.81	-9.80	-6.47	-3.75
4 modes	-6.39	-15.24	-10.60	-12.68	-4.64	-6.09	-6.46	-15.76	-10.65	-3.33	-6.27
5 modes	-5.93	-17.91	-10.35	-11.93	-4.73	-4.69	-6.47	-15.08	-11.28	-6.65	-3.51
6 modes	-5.95	-17.84	-10.45	-10.91	-4.94	-4.48	-6.35	-14.99	-11.86	-6.47	-3.18

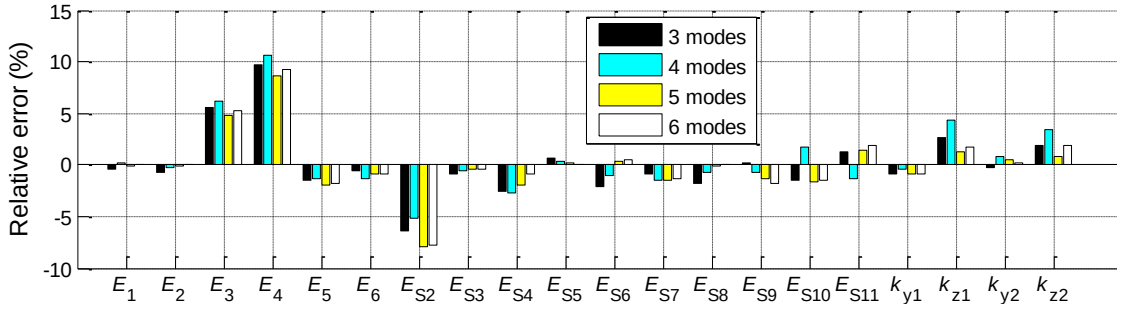

Figure 5.18. Relative errors of the updated parameters for the entire structure by minimization of modal property differences

results is better than that of updating the entire structure. The conclusion can be due to the two advantages of the proposed substructure approach. First, the number of physical parameters to be updated is smaller for the substructure approach, when compared with updating an entire structure. Second, the number of the unmeasured DOFs in the substructure approach is much smaller than that when updating the entire structure; or in other words, the substructure approach encounters less difficulty during modal expansion. Thus, the optimization procedure for model updating converges more readily for the substructure approach.

5.4.2 Investigation on Substructure Location

Choosing appropriate substructure location can be a complicated issue, depending on the objective and interest of model updating, the type and size of the entire structure, the categories of updating parameters, and the accuracy of the initial finite element model, among others. Therefore, it is difficult to provide a universal guide for choosing appropriate substructure location. This subsection conducts a preliminary study on the particular example of the space frame structure (Figure 5.12). It is assumed that there is no preference for any parameters. When assigning initial and actual values for the stiffness parameters of the space frame structure shown in TABLE 5.9, as often happening in practice, it is assumed that the initial model has higher accuracy for material properties (with maximum relative difference of -15% for E_{S8}), and lower accuracy for the stiffness of boundary springs (with maximum relative difference of 60% for k_{z1} and k_{z2}).

The entire space frame model is divided into four substructures with similar size, as shown in Figure 5.19. Substructure #1 contains segments 1~3, substructure #2 contains segments 4~6, substructure #3 contains segments 7~9, and substructure #4 contains segments 10~11. Substructure model updating is conducted on each substructure

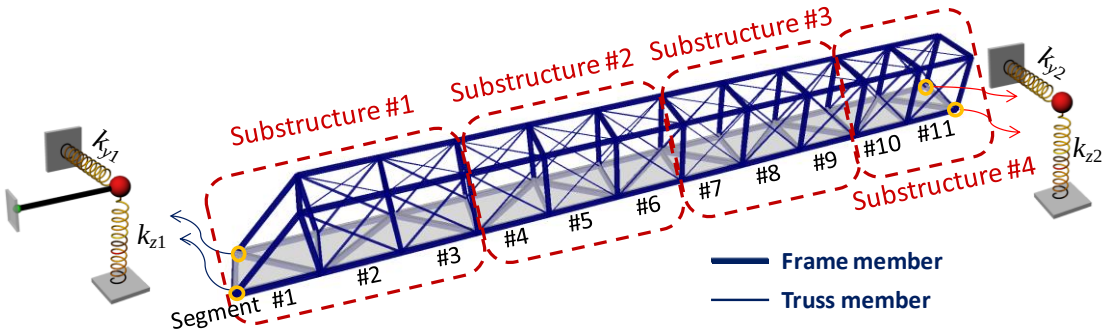

Figure 5.19. Substructures at various locations

separately, when the residual structure contains the rest of the structure. For example, when updating substructure #2, the residual structure contains substructures #1, #3 and #4. For practicality, it is also assumed only translational DOFs of the substructure and interface nodes are instrumented with accelerometers for capturing substructure vibration modes; rotational DOFs are not measured. Consistently, regardless of which substructure, no measurement is required on the residual structure. Same as before, modal frequencies and substructure mode shapes of the simulated actual structure (ω_j and $\boldsymbol{\psi}_{\mathrm{m},j}$) are used as "experimental data".

For model condensation, dynamic response of the residual structure for each substructure model updating is approximated using twenty modal coordinates, i.e. $n_q = 20$ in Equation (5.3). Accurate structural mass matrix is assumed to be known, so mass parameters $\boldsymbol{\beta}$ is not among the updating parameters for each substructure model updating. All substructure models contain updating parameters along the entire structure, such as the five elastic moduli of the frame members (E_1~E_5), and the elastic moduli of top bracing truss members (E_6). Meanwhile, each substructure model also contains its own location-dependent updating parameters. For example, substructure #1 contains elastic moduli of side-bracing truss members at the 2nd and 3rd segments (E_{S2} and E_{S3}), and the spring stiffness values at the left support (k_{y1} and k_{z1}). Substructure #2 contains elastic moduli of side-bracing truss members at the 4th, 5th, and 6th segments (E_{S4}, E_{S5} and E_{S6}).

Substructure #3 contains elastic moduli of side-bracing truss members at the 7th, 8th, and 9th segments (E_{S7}, E_{S8} and E_{S9}). Finally, substructure #4 contains elastic moduli of side-bracing truss members at the 10th and 11thsegments (E_{S11} and E_{S12}), and the spring stiffness values at the right support (k_{y1} and k_{z1}).

TABLE 5.13 summarizes the updating results for all substructure models. For brevity, only the scenario with five available modes is simulated for each substructure. For each substructure updating, most of the updated parameter changes are close to the ideal percentages listed in TABLE 5.9. The parameters of the corresponding residual structure cannot be updated, and are marked with "—". Note that E_4 is not used to compare the performance, because it is less sensitive to translational DOFs.

To quantify the updating accuracy for each substructure updating, Figure 5.20 plots the relative updating errors of the physical parameters in each substructure (excluding the non-sensitive parameter E_4). The updating errors are generally small for each substructure updating (most errors are within -1% ~ +1%). An exception is E_3 in substructure #2, with a larger error of +2.83%. To further quantify the performance, the average values of the relative updating errors for each substructure are calculated and shown in the title of each plot in Figure 5.20, where substructures #2 gives the lowest updating accuracy (with an average error of 0.9%).

TABLE 5.13. Updated stiffness parameter changes (%) for the substructure models with five available modes

Sub-structure	Frame member					Spring			
	E_1	E_2	E_3	E_4	E_5	k_{y1}	k_{z1}	k_{y1}	k_{z2}
#1	4.21	4.17	-5.61	-5.76	4.16	-30.54	59.01	—	—
#2	4.85	4.24	-2.17	-3.76	4.06	—	—	—	—
#3	5.47	4.53	-4.85	-7.19	4.75	—	—	—	—
#4	4.44	4.29	-5.23	-5.43	4.08	—	—	-30.48	-59.42
Sub-structure	**Truss member**									
	E_6	E_{S2}	E_{S3}	E_{S4}	E_{S5}	E_{S6}	E_{S7}	E_{S8}	E_{S9}	E_{S10}	E_{S11}
#1	-6.24	-10.68	-10.94	—	—	—	—	—	—	—	—
#2	-4.14	—	—	10.52	-5.41	-5.73	—	—	—	—	—
#3	-4.54	—	—	—	—	—	-5.43	-14.82	-10.15	—	—
#4	-5.21	—	—	—	—	—	—	—	—	-5.58	-5.46

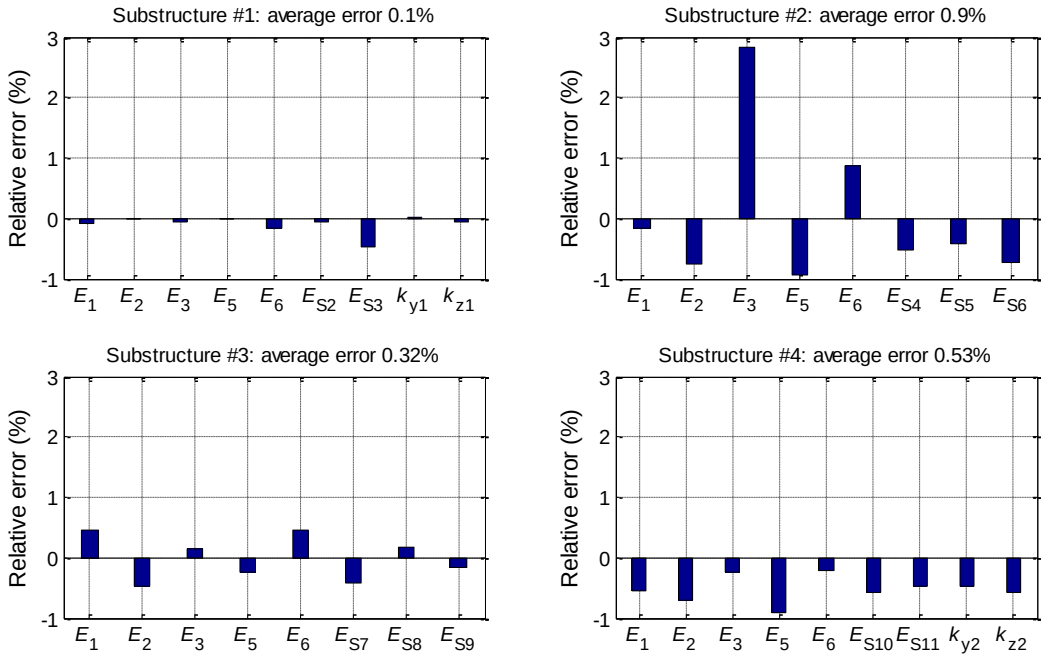

Figure 5.20. Relative errors of the updated parameters for substructures at various locations

Reviewing the substructure locations in Figure 5.19, it is easy to see that the substructures #1 and #4 are located close to the two ends of the frame structure, and contains the parameters with most inaccurate initial values (stiffness of the support springs). Substructure #3 contains the crossing bracing truss member with the most inaccurate initial value (E_{S8}), where the maximum relative difference is -15%. These inaccurate parameters get directly updated in the updating procedure of these three substructures. Meanwhile, substructure #2 is located close to the middle of the frame structure. The parameters with most inaccurate initial values are in the corresponding residual structure, and thus, cannot be directly updated. As shown in Equation (5.11), the residual structure is updated using modal parameters based on the assumption that parameter changes in the actual residual structure from initial values do not significantly alter the generalized eigenvectors $\boldsymbol{\varphi}_{R0,j}$. Therefore, those parameters with most inaccurate initial values in the residual structure cause more difficulties when updating

substructures #2. In summary, the simulation illustrates that to obtain higher updating accuracy, a substructure can be located to contain parameters associated with least prior knowledge (which tend to have largest initial errors), so that these parameters can be updated together with the substructure.

5.4.3 Performance Evaluation of Substructure Size

Choosing an appropriate substructure size is another interesting issue for substructure updating. A smaller substructure contains less number of DOFs, and thus the updating requires less computation efforts. However, decrease of substructure size increases the discrepancy between of the simulated residual structure and the actual residual structure. This may violate the assumption that the generalized eigenvectors $\boldsymbol{\varphi}_{R0,j}$ of the initial residual structural matrices are not significantly different to those of the actual residual structure (Equation (5.11)). This subsection conducts a preliminary study on the space frame structure (Figure 5.12) to verify updating accuracy with different sizes of the substructure.

The substructure containing the first three segments (Figure 5.12) has been studied in Section 5.3.4. This study extends to two additional examples with different substructure sizes. The first one adopts a smaller substructure with the first two segments (Figure 5.21), containing 6 substructure nodes and 4 interface nodes. The second one adopts a larger substructure with the first four segments (Figure 5.22), containing 14 substructure nodes and 4 interface nodes. For model condensation, dynamic response of the residual structure for each substructure model is approximated using twenty modal coordinates, i.e. n_q = 20 in Equation (5.3). Similar as Section 5.3.4, it is assumed only translational DOFs of the substructure and interface nodes are instrumented with accelerometers for capturing substructure vibration modes; rotational DOFs are not measured.

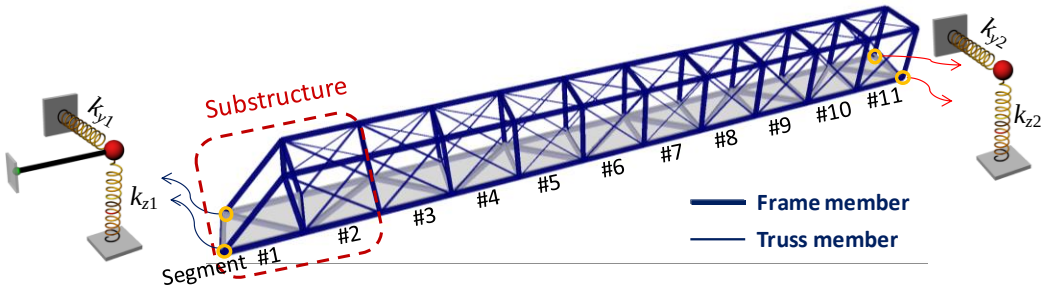

Figure 5.21. Smaller substructure with first two segments

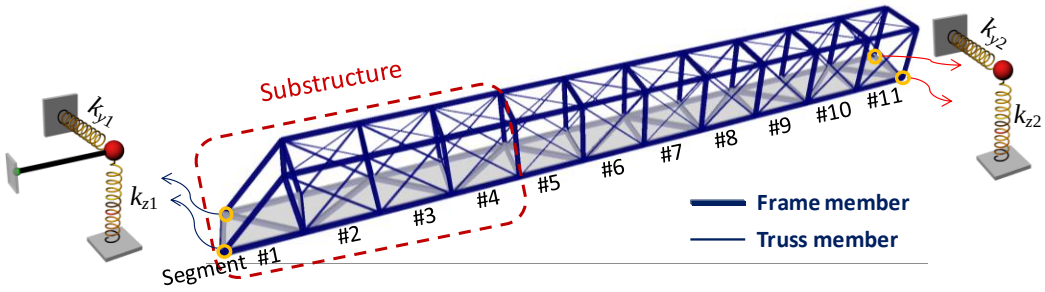

Figure 5.22. Larger substructure with first four segments

The stiffness parameters for both examples with smaller and larger substructures are similar as those described in Section 5.3.4. They both contain the five elastic moduli of the frame members (E_1~E_5), the elastic moduli of top bracing truss members (E_6), and the spring stiffness values at the left support (k_{y1} and k_{z1}). The difference for the smaller substructure model is that only the elastic moduli of side-bracing truss members at the 2nd segments (E_{S2}) is included; E_{S3} is not included. The difference for the larger substructure model is that besides E_{S2} and E_{S3}, the elastic moduli of side-bracing truss members at the 4th segments (E_{S4}) is also included.

TABLE 5.14 summarizes the updating results using the proposed modal dynamic residual approach for the smaller substructure model. The results are presented in terms of relative change percentages from initial values. When three modes are available, most of the updated parameter changes are quite different to the actual percentages listed in TABLE 5.9. With more available modes, the updating accuracy improves. Same as in

TABLE 5.14. Updated parameter changes (%) for substructure elements on the smaller substructure model by minimization of modal dynamic residuals

Available modes	Frame member					Truss member		Spring	
	E_1	E_2	E_3	E_4	E_5	E_6	E_{S2}	k_{y1}	k_{z1}
3 modes	-1.12	-2.69	-10.26	-10.29	-2.85	-11.88	-15.85	-35.19	51.09
4 modes	2.99	2.70	-6.65	-7.03	2.66	-7.96	-11.96	-31.53	57.23
5 modes	4.76	4.77	-5.15	-5.67	4.75	-5.59	-10.28	-30.14	59.76
6 modes	4.65	4.36	-5.05	-5.20	4.35	-5.91	-10.62	-30.44	59.91

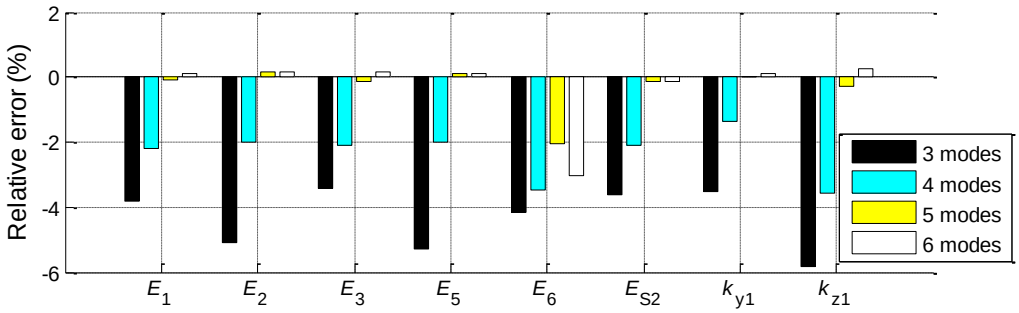

Figure 5.23. Relative errors of the updated parameters for the smaller substructure

previous examples, the non-sensitive updating parameter E_4 is not considered for evaluating the updating performance. Figure 5.23 plots the relative errors of the updating results (excluding E_4) for different numbers of available modes. The figure also shows the updating accuracy significantly improves when more measured modes are available.

TABLE 5.15 summarizes the updating results using the proposed modal dynamic residual approach for the larger substructure model. For every available number of modes, most of the updated parameter changes are close to the ideal percentages listed in TABLE 5.9. Figure 5.24 plots the relative errors of the updating results (excluding E_4) for different numbers of available modes. The maximum error is only 0.46% for E_6 with six available modes, which indicates that reasonable results can be achieved for all available modes. The figure also shows the updating accuracy is generally improved when more measured modes are available.

To compare the performance related to substructure size, Figure 5.25 plots the relative errors of the updating results for the structure with reference size of three

segments in Section 5.3.4. Comparing Figure 5.23, Figure 5.24 and Figure 5.25, it can be concluded that the updating accuracy generally increases with the increment of substructure size, especially for a small number of available modes. The comparison also indicates that when more measured modes are available, the updating accuracy are satisfactory for all three different substructure sizes.

TABLE 5.15. Updated parameter changes (%) for substructure elements on the larger substructure model by minimization of modal dynamic residuals

Available modes	Frame member					Truss member				Spring	
	E_1	E_2	E_3	E_4	E_5	E_6	E_{S2}	E_{S3}	E_{S4}	k_{y1}	k_{z1}
3 modes	4.87	4.80	-4.96	-5.19	4.79	-5.14	-10.13	-10.12	-10.03	-30.12	60.10
4 modes	4.89	4.83	-4.89	-5.23	4.82	-5.19	-10.12	-10.07	-10.01	-30.09	60.22
5 modes	4.88	4.86	-5.07	-6.01	4.85	-4.64	-10.07	-10.02	-10.10	-30.08	59.89
6 modes	5.06	4.76	-4.92	-5.68	4.74	-4.53	-10.01	-9.94	-10.25	-30.18	60.14

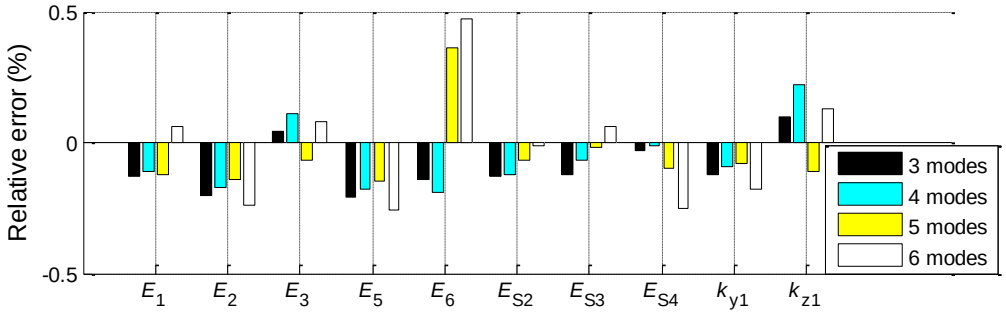

Figure 5.24. Relative errors of the updated parameters for the larger substructure

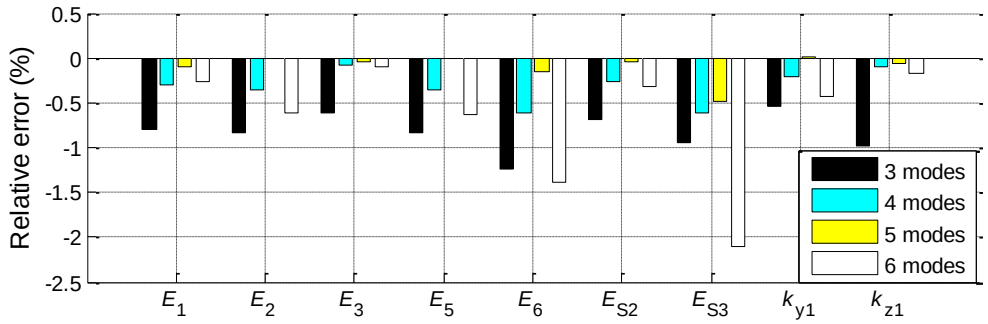

Figure 5.25. Relative errors of the updated parameters for the substructure with three frame segments in Section 5.3.4 (excluding E_4)

5.5 Summary

This chapter studies substructure model updating through minimization of modal dynamic residuals. The entire structural model is divided into the substructure (currently being instrumented and to be updated) and the residual structure. The Craig-Bampton transform is adopted to condense the residual structure using a limited number of dominant mode shapes, while the substructure remains at high resolution. To update the condensed structural model, physical parameters in the substructure and modal parameters of the residual structure are chosen as optimization variables; minimization of the modal dynamic residuals is determined as the optimization objective. An iterative linearization procedure is adopted for efficiently solving the optimization problem.

The proposed substructure updating method is validated through numerical examples, including a lumped spring-mass model, a plane truss, a plane frame, and a space frame structure. For each example, the proposed approach accurately identifies most of the substructure parameters. For comparison, a conventional approach minimizing modal property differences is also applied. With simpler examples (the spring-mass model and the plane truss model), the conventional approach achieves reasonable results but with lower accuracy than the proposed modal dynamic residual approach. With more complicated models (the plane and space frame structures), the conventional approach performs even worse and overall cannot achieve reasonable updating results.

The performance of the proposed substructure model updating approach is further investigated through numerical simulation of the space frame structure on three topics of interest. The first topic is performance comparison with model updating of an entire structure. Assuming the same number of sensor channels is used, the entire space frame model is updated using modal dynamic residual approach. The achieved updating accuracy is much lower than the proposed substructure approach. The second topic focuses on the effect of substructure location. Four substructures of similar size are

selected at different locations. The simulations show that three substructures covering parameters with least prior knowledge give more accurate updating results, because in this way, these parameters are directly updated together with the substructures. The third topic focuses on the effect of substructure size. Three different substructure sizes are simulated. With enough sensors instrumented on all substructure and interface nodes, the results indicates that the updating accuracy generally increases with larger substructure size, especially when a smaller number of measured modes are available. When the substructure size is too small, the updating accuracy can be unacceptable when very small number of modes are available. When more measured modes are available, the updating accuracy are satisfactory for all three substructure sizes.

CHAPTER 6 CONCLUSIONS AND FUTURE DIRECTIONS

Building upon wireless sensing technologies, this thesis proposes mobile sensing network for structure health monitoring. Furthermore, decentralized structural damage detection and model updating algorithms have been proposed in this research for analyzing wireless and mobile sensor data collected at high spatial resolutions. This chapter first provides a conclusion of the dissertation, and then discusses future research directions.

6.1 Conclusions

The research on mobile sensing network and decentralized structural damage detection and model updating leads to following main conclusions:

1. To achieve high spatial resolution measurement and reduce instrumentation labor and cost, mobile sensing network can be adopted for applications in structure health monitoring. Two mobile sensing prototypes have been developed. The first prototype adopts a single-car design with accelerometers fixed on the body. The second prototype adopts a flexure-based design that can attach an accelerometer to structural surface for higher-accuracy measurement. The mobile sensing network has been proved to be feasible and reliable through laboratory and field tests.

2. Decentralized structural damage detection is explored using transmissibility functions. A decentralized structural damage detection procedure is proposed herein for the mobile sensing nodes (MSNs). The decentralized procedure only requires measurements in one small neighborhood at a time, and thus, is ideal for adoption by a small group of MSNs that take measurements in one area at a time and automatically scan through a structure. Laboratory experiments are conducted and demonstrate that the approach can locate various damage scenarios using mobile sensor data.

3. The nature of transmissibility functions for damage detection is analytically investigated on a general multi-DOF spring-mass-damper model. The analytical derivation shows that the difference in transmissibility functions between undamaged and damaged structures is sensitive to various damage scenarios. Furthermore, the largest damage indicator should always occur near a damage location. The analytical derivations are validated through numerical simulations and laboratory experiments on a five-story shear-building structure using MSNs.

4. Decentralized structural model updating is explored by minimizing modal dynamic residuals. The entire structural model is divided into a substructure (currently being instrumented and to be updated) and the residual structure. The Craig-Bampton transform is adopted to condense the residual structure using a limited number of dominant mode shapes. To update the condensed structural model, physical parameters in the substructure and modal parameters of the residual structure are chosen as optimization variables; minimization of the modal dynamic residuals is determined as the optimization objective. The proposed approach has been validated through numerical simulations, and shows better updating accuracy compared to the conventional approach minimizing modal property differences. The performance of the proposed substructure model updating approach is further investigated through numerical simulations on three topics of interest. The first topic compares the proposed approach with updating of an entire structure, and proves that given the same amount of sensing channels, the proposed substructure approach improves updating accuracy. The second topic focuses on substructure location selection, and illustrates that substructures containing parameters with least prior knowledge give more accurate updating results. The third topic focuses on substructure size, and indicates the updating accuracy generally increases with a larger structure size.

6.2 Future Work

Building upon current work, future research can be expanded along following directions.

1. The mobile sensing nodes developed in this research only work on smooth ferromagnetic structural surface. Significant efforts will be needed for developing mobile sensing nodes with advanced mobility to operate reliably on various structural surfaces with complex obstacles. For example, a flying mobile sensing node can be realized by equipping wireless sensing modules to a quadricopter. Multi-functional mobile sensing nodes can be developed to measure and record various physical stimuli. Wireless cameras can be equipped on future generations of mobile sensing nodes, to allow the mobile sensing nodes to observe their surroundings. In addition, a mobile excitation node can be developed for applying small-magnitude impact forces to one local area of a structure.

2. In this study, the decentralized damage detection approach using transmissibility functions of mobile sensor data has been validated on small-scale laboratory experiments. Further validations are needed on more complicated and realistic structures. Furthermore, the damage sensitivities of transmissibility functions have been studied on a lumped mass model in this research, using inversion of a tri-diagonal matrix. Future studies are needed for general 2D and 3D structural models, where inversion formulation of block-diagonal matrices can be utilized. In addition to damage detection, future studies can be extended to damage quantification, in order to facilitate structural condition assessment and retrofitting decisions. Furthermore, it is necessary that methodologies investigated in this research be performed in conjunction with other techniques for determining the type and nature of damage.

3. The proposed substructure updating approach has been successfully validated through numerical simulations. Performance of the updating approach minimizing modal dynamic residuals still requires validation on more complex large-scale models. In this thesis, the connections between structural members are assumed to be ideal, e.g. rigid

connections between frame members and pinned connections for truss members. In reality, the difference between simulation and measurement arises from not only member properties, but also non-ideal connection stiffnesses. How to distinguish the root cause can be a very interesting future direction. In addition, when applied on experimental data, the updating results are not as satisfactory. Further investigation is needed on the performance using noisy measurement. Furthermore, the current substructure approach can be strengthened by adopting probabilistic theories [99, 100].

4. This research investigates substructure model updating using modal properties in frequency domain, thus the proposed approach is only valid on linear structural models. As mentioned in the literature review, another popular category of model updating algorithms operates in time domain, in which non-linear structural models can be considered. Therefore, substructure updating can also be explored using time-domain approaches, such as the quadratic sum-square error (QSSE) approach [57-59].

5. This research explores decentralized structural damage detection and model updating in an offline manner. Future research efforts can be devoted to online (real-time) decentralized approaches using wireless and mobile sensing network, in order to provide real-time structural condition assessment during sudden events.

REFERENCES

[1] ASCE, *Report Card for America's Infrastructure*. Reston, VA: American Society of Civil Engineers, 2013.

[2] M. Moore, B. Phares, B. Graybeal, D. Rolander, and G. Washer, "Reliability of Visual Inspection for Highway Bridges," Federal Highway Administration, McLean, VA Report No. FHWA-RD-01-020, 2001.

[3] J. M. Ko and Y. Q. Ni, "Technology developments in structural health monitoring of large-scale bridges," *Engineering Structures*, vol. 27, pp. 1715-1725, 2005.

[4] C. R. Farrar, H. Sohn, F. M. Hemez, M. C. Anderson, M. T. Bement, P. J. Cornwell, *et al.*, "Damage Prognosis: Current Status and Future Needs," Los Alamos National Laboratory, Los Alamos, NM Report No. LA-14051-MS, 2003.

[5] M. Çelebi, "Seismic Instrumentation of Buildings (with Emphasis on Federal Buildings)," United States Geological Survey, Menlo Park, CA Report No. 0-7460-68170, 2002.

[6] E. G. Straser and A. S. Kiremidjian, "A Modular, Wireless Damage Monitoring System for Structures," John A. Blume Earthquake Eng. Ctr., Stanford University, Stanford, CA Report No. 128, 1998.

[7] J. P. Lynch and K. J. Loh, "A summary review of wireless sensors and sensor networks for structural health monitoring," *The Shock and Vibration Digest*, vol. 38, pp. 91-128, 2006.

[8] S. Kim, S. Pakzad, D. Culler, J. Demmel, G. Fenves, S. Glaser, *et al.*, "Health monitoring of civil infrastructures using wireless sensor networks," presented at the Proceedings of the 6th International Conference on Information Processing in Sensor Networks (IPSN '07), Cambridge, MA, 2007.

[9] B. F. Spencer, Jr., M. E. Ruiz-Sandoval, and N. Kurata, "Smart sensing technology: opportunities and challenges," *Structural Control and Health Monitoring*, vol. 11, pp. 349-368, 2004.

[10] M. Shinozuka, M. Q. Feng, P. Chou, Y. Chen, and C. Park, "MEMS-based wireless real-time health monitoring of bridges," presented at the Proceedings of

the 3rd International Conference on Earthquake Engineering, Nanjing, China, 2004.

[11] M. Kane, D. Zhu, M. Hirose, X. Dong, B. Winter, M. Häckell, *et al.*, "Development of an extensible dual-core wireless sensing node for cyber-physical systems," in *Proceedings of SPIE, Nondestructive Characterization for Composite Materials, Aerospace Engineering, Civil Infrastructure, and Homeland Security*, San Diego, California, USA, 2014.

[12] Y. Wang, J. P. Lynch, and K. H. Law, "A wireless structural health monitoring system with multithreaded sensing devices: design and validation," *Structure and Infrastructure Engineering*, vol. 3, pp. 103-120, 2007.

[13] Y. Wang, K. J. Loh, J. P. Lynch, M. Fraser, K. H. Law, and A. Elgamal, "Vibration monitoring of the Voigt Bridge using wired and wireless monitoring systems," presented at the Proceedings of the 4th China-Japan-US Symposium on Structural Control and Monitoring, Hangzhou, China, 2006.

[14] J. P. Lynch, Y. Wang, K. J. Loh, J.-H. Yi, and C.-B. Yun, "Performance monitoring of the Geumdang Bridge using a dense network of high-resolution wireless sensors," *Smart Materials and Structures*, vol. 15, pp. 1561-1575, 2006.

[15] J.-H. Weng, C.-H. Loh, J. P. Lynch, K.-C. Lu, P.-Y. Lin, and Y. Wang, "Output-only modal identification of a cable-stayed bridge using wireless monitoring systems," *Engineering Structures*, vol. 30, pp. 1820-1830, 2008.

[16] I. F. Akyildiz, W. Su, Y. Sankarasubramaniam, and E. Cayirci, "A survey on sensor networks," *Communications Magazine, IEEE*, vol. 40, pp. 102-114, 2002.

[17] F. Tache, W. Fischer, G. Caprari, R. Siegwart, R. Moser, and F. Mondada, "Magnebike: a magnetic wheeled robot with high mobility for inspecting complex-shaped structures," *Journal of Field Robotics*, vol. 26, pp. 453-476, May 2009.

[18] C. Choi, B. Park, and S. Jung, "The design and analysis of a feeder pipe inspection robot with an automatic pipe tracking system," *Ieee-Asme Transactions on Mechatronics*, vol. 15, pp. 736-745, Oct 2010.

[19] M. P. Murphy and M. Sitti, "Waalbot: an agile small-scale wall-climbing robot utilizing dry elastomer adhesives," *Mechatronics, IEEE/ASME Transactions on,* vol. 12, pp. 330-338, 2007.

[20] W. R. Provancher, S. I. Jensen-Segal, and M. A. Fehlberg, "ROCR: an energy-efficient dynamic wall-climbing robot," *Ieee-Asme Transactions on Mechatronics,* vol. 16, pp. 897-906, Oct 2011.

[21] D. R. Huston, B. Esser, G. Gaida, S. W. Arms, and C. P. Townsend, "Wireless inspection of structures aided by robots," in *Proceedings of SPIE, Health Monitoring and Management of Civil Infrastructure Systems*, Newport Beach, CA, 2001, pp. 147-154.

[22] P. G. Backes, Y. Bar-Cohen, and B. Joffe, "The multifunction automated crawling system (MACS)," presented at the Proceedings of the 1997 IEEE International Conference on Robotics and Automation, Albuquerque, New Mexico, 1997.

[23] M. Todd, D. Mascarenas, E. Flynn, T. Rosing, B. Lee, D. Musiani, *et al.*, "A different approach to sensor networking for SHM: remote powering and interrogation with unmanned aerial vehicles," in *Proceedings of the 6th International Workshop on Structural Health Monitoring*, Stanford, CA, 2007.

[24] S. W. Doebling, C. R. Farrar, and M. B. Prime, "A summary review of vibration-based damage identification methods," *The Shock and Vibration Digest,* vol. 30, pp. 91-105, 1998.

[25] W. Fan and P. Z. Qiao, "Vibration-based damage identification methods: a review and comparative study," *Structural Health Monitoring-an International Journal,* vol. 10, pp. 83-111, Jan 2011.

[26] H. Y. Li and H. Xu, "Damage detection for structural health monitoring using ultrasonic guided waves," in *Advances in Fracture and Damage Mechanics Xi*. vol. 525-526, Q. F. Li, Y. L. Li, and M. H. Aliabadi, Eds., ed, 2013, pp. 433-436.

[27] H. Uchida, L. Brigatti, and J. Caprioli, "Detection of structural damage from glaucoma with confocal laser image analysis," *Investigative Ophthalmology & Visual Science,* vol. 37, pp. 2393-2401, Nov 1996.

[28] C. Colla, P. C. Das, D. McCann, and M. C. Forde, "Sonic, electromagnetic and impulse radar investigation of stone masonry bridges," *Ndt & E International,* vol. 30, pp. 249-254, Aug 1997.

[29] C. Cheng and M. Sansalone, "The Impact-echo response of concrete plates containing delaminations - numerical, experimental and field studies," *Materials and Structures,* vol. 26, pp. 274-285, Jun 1993.

[30] T. K. Lin, S. L. Hung, and C. S. Huang, "Detection of damage location using a novel substructure-based frequency response function approach with a wireless sensing system," *International Journal of Structural Stability and Dynamics,* vol. 12, Jul 2012.

[31] H. Zhang, M. J. Schulz, F. Ferguson, and P. F. Pai, "Structural health monitoring using transmittance functions," *Mechanical Systems and Signal Processing,* vol. 13, pp. 765-787, Sep. 1999.

[32] H. R. Kess and D. E. Adams, "Investigation of operational and environmental variability effects on damage detection algorithms in a woven composite plate," *Mechanical Systems and Signal Processing,* vol. 21, pp. 2394-2405, Aug 2007.

[33] C. Devriendt and P. Guillaume, "Identification of modal parameters from transmissibility measurements," *Journal of Sound and Vibration,* vol. 314, pp. 343-356, July 2008.

[34] Z. Mao and M. Todd, "A model for quantifying uncertainty in the estimation of noise-contaminated measurements of transmissibility," *Mechanical Systems and Signal Processing,* vol. 28, pp. 470-481, Apr 2012.

[35] T. J. Johnson and D. E. Adams, "Transmissibility as a differential indicator of structural damage," *Journal of Vibration and Acoustics-Transactions of the ASME,* vol. 124, pp. 634-641, 2002.

[36] M. I. Friswell and J. E. Mottershead, *Finite element model updating in structural dynamics*. Dordrecht, Boston: Kluwer Academic Publishers, 1995.

[37] S. Liu, "Improvement of analytical dynamic-models using complex model test data," *International Journal of Mechanical Sciences,* vol. 34, pp. 817-829, Oct 1992.

[38] S. R. Ibrahim, "Dynamic modeling of structures from measured complex modes," *AIAA Journal,* vol. 21, pp. 898-901, 1983.

[39] O. S. Salawu, "Detection of structural damage through changes in frequency: A review," *Engineering Structures,* vol. 19, pp. 718-723, Sep 1997.

[40] P. W. Moller and O. Friberg, "Updating large finite element models in structural dynamics," *AIAA Journal,* vol. 36, pp. 1861-1868, Oct 1998.

[41] B. Jaishi and W. X. Ren, "Damage detection by finite element model updating using modal flexibility residual," *Journal of Sound and Vibration,* vol. 290, pp. 369-387, Feb 2006.

[42] C. Farhat and F. M. Hemez, "Updating finite element dynamic models using an element-by-element sensitivity methodology," *AIAA Journal,* vol. 31, pp. 1702-1711, Sep 1993.

[43] M. Sanayei, J. A. McClain, S. Wadia-Fascetti, and E. M. Santini, "Parameter estimation incorporating modal data and boundary conditions," *Journal of structural engineering,* vol. 125, pp. 1048-1055, 1999.

[44] M. Sanayei, B. Arya, E. M. Santini, and S. Wadia‐Fascetti, "Significance of modeling error in structural parameter estimation," *Computer‐Aided Civil and Infrastructure Engineering,* vol. 16, pp. 12-27, 2001.

[45] D. Zhu, X. Dong, and Y. Wang, "A comparative study on modal-based finite element model updating approaches using noisy measurements," presented at the Proceedings of the 11th International Conference on Structural Safety & Reliability (ICOSSAR), New York, NY, USA, 2013.

[46] P. Caravani, M. L. Watson, and W. T. Thomson, "Recursive least-squares time domain identification of structural parameters," *Journal of Applied Mechanics,* vol. 44, pp. 135-140, 1977.

[47] M. Hoshiya and E. Saito, "Structural identification by extended Kalman filter," *Journal of Engineering Mechanics-ASCE,* vol. 110, pp. 1757-1770, 1984.

[48] A. W. Smyth, S. F. Masri, A. G. Chassiakos, and T. K. Caughey, "On-line parametric identification of MDOF nonlinear hysteretic systems," *Journal of Engineering Mechanics-ASCE,* vol. 125, pp. 133-142, Feb 1999.

[49] C. H. Loh and I. C. Tou, "A system identification approach to the detection of changes in both linear and nonlinear structural parameters," *Earthquake Engineering & Structural Dynamics,* vol. 24, pp. 85-97, Jan 1995.

[50] A. W. Smyth, S. F. Masri, E. B. Kosmatopoulos, A. G. Chassiakos, and T. K. Caughey, "Development of adaptive modeling techniques for non-linear hysteretic systems," *International Journal of Non-Linear Mechanics,* vol. 37, pp. 1435-1451, Dec 2002.

[51] J. N. Yang, S. L. Lin, H. W. Huangl, and L. Zhou, "An adaptive extended Kalman filter for structural damage identification," *Structural Control & Health Monitoring,* vol. 13, pp. 849-867, Jul-Aug 2006.

[52] J. N. Yang, H. W. Huang, and S. L. Lin, "Sequential non-linear least-square estimation for damage identification of structures," *International Journal of Non-Linear Mechanics,* vol. 41, pp. 124-140, Jan 2006.

[53] J. N. Yang, S. Pan, and H. Huang, "An adaptive extended Kalman filter for structural damage identifications II: unknown inputs," *Structural Control & Health Monitoring,* vol. 14, pp. 497-521, Apr 2007.

[54] J. N. Yang and H. Huang, "Sequential non-linear least-square estimation for damage identification of structures with unknown inputs and unknown outputs," *International Journal of Non-Linear Mechanics,* vol. 42, pp. 789-801, Jun 2007.

[55] T. Sato and K. Qi, "Adaptive H-infinity filter: Its application to structural identification," *Journal of Engineering Mechanics-Asce,* vol. 124, pp. 1233-1240, Nov 1998.

[56] T. Sato and M. Chung, "Structural identification using adaptive Monte Carlo filter," *Journal of Structural Engineering, JSCE,* vol. 51, pp. 471-477, 2005.

[57] H. Huang, J. N. Yang, and L. Zhou, "Adaptive quadratic sum-squares error with unknown inputs for damage identification of structures," *Structural Control and Health Monitoring,* vol. 17, pp. 404-426, 2010.

[58] J. N. Yang, H. W. Huang, and S. W. Pan, "Adaptive quadratic sum-squares error for structural damage identification," *Journal of Engineering Mechanics-Asce*, vol. 135, pp. 67-77, Feb 2009.

[59] R. Li, L. Zhou, and J. N. Yang, "Experimental verifications of a structural damage identification technique using reduced order finite-element model," in *SPIE Smart Structures and Materials+ Nondestructive Evaluation and Health Monitoring*, 2010, pp. 76470A-76470A-8.

[60] R. R. Craig, Jr., "Coupling of substructures for dynamic analyses - an overview," in *Proceedings of the 41st AIAA/ASME/ASCE/AHS/ASC Structures, Structural Dynamics, and Materials Conference and Exhibit*, Atlanta, GA, 2000.

[61] R. R. Craig and M. C. C. Bampton, "Coupling of substructures for dynamic analyses," *Aiaa Journal*, vol. 6, pp. 1313-&, 1968.

[62] M. Link, "Updating analytical models by using local and global parameters and relaxed optimisation requirements," *Mechanical Systems and Signal Processing*, vol. 12, pp. 7-22, 1998.

[63] Q. Zhao, T. Sawada, K. Hirao, and Y. Nariyuki, "Localized identification of MDOF structures in the frequency domain," *Earthquake Engineering & Structural Dynamics*, vol. 24, pp. 325-338, Mar 1995.

[64] D. Zhang and E. A. Johnson, "Substructure identification for shear structures I: Substructure identification method," *Structural Control and Health Monitoring*, vol. 20, pp. 804-820, 2013.

[65] D. Zhang and E. A. Johnson, "Substructure identification for shear structures II: Controlled substructure identification," *Structural Control and Health Monitoring*, vol. 20, pp. 821-834, 2013.

[66] C. G. Koh and K. Shankar, "Substructural identification method without interface measurement," *Journal of Engineering Mechanics*, vol. 129, p. 769, 2003.

[67] C. G. Koh, L. M. See, and T. Balendra, "Estimation of structural parameters in time domain - a substructure approach," *Earthquake Engineering & Structural Dynamics*, vol. 20, pp. 787-801, Aug 1991.

[68] C. G. Koh, B. Hong, and C. Y. Liaw, "Substructural and progressive structural identification methods," *Engineering structures*, vol. 25, pp. 1551-1563, 2003.

[69] T. N. Trinh and C. G. Koh, "An improved substructural identification strategy for large structural systems," *Structural Control and Health Monitoring*, vol. 19, pp. 686-700, 2012.

[70] K. F. Tee, C. G. Koh, and S. T. Quek, "Substructural first- and second-order model identification for structural damage assessment," *Earthquake Engineering & Structural Dynamics*, vol. 34, pp. 1755-1775, 2005.

[71] K.-V. Yuen and L. S. Katafygiotis, "Substructure identification and health monitoring using noisy response measurements only," *Computer-Aided Civil and Infrastructure Engineering*, vol. 21, pp. 280-291, 2006.

[72] J. N. Yang and H. Huang, "Substructure damage identification using damage tracking technique," in *Proceedings of SPIE, Sensors and Smart Structures Technologies for Civil, Mechanical, and Aerospace Systems 2007*, San Diego, CA, USA, 2007, p. 65292R.

[73] J. Hou, Ł. Jankowski, and J. Ou, "A substructure isolation method for local structural health monitoring," *Structural Control and Health Monitoring*, vol. 18, pp. 601-618, 2011.

[74] D. Zhu, Q. Qi, Y. Wang, K.-M. Lee, and S. Foong, "A prototype mobile wireless sensor network for structural health monitoring," in *Proceedings of SPIE, Nondestructive Characterization for Composite Materials, Aerospace Engineering, Civil Infrastructure, and Homeland Security 2009*, San Diego, CA, 2009, p. 72941A.

[75] K.-M. Lee, Y. Wang, D. Zhu, J. Guo, and X. Yi, "Flexure-based mechatronic mobile sensors for structure damage detection," in *Proceedings of the 7th International Workshop on Structural Health Monitoring*, Stanford, CA, USA, 2009.

[76] D. Zhu, X. Yi, Y. Wang, J. Guo, and K.-M. Lee, "Mobile sensor network: a new apporach for structural health monitoring," presented at the Proceedings of the 2010 Structures Congress and 19th Analysis and Computation Specialty Conference, Orlando, FL, USA, 2010.

[77] D. Zhu, J. Guo, X. Yi, Y. Wang, and K.-M. Lee, "A flexure-based mobile sensing node for the health monitoring of steel structures," presented at the Proceedings of the 2011 NSF CMMI Research and Innovation Conference, Atlanta, GA, USA, 2011.

[78] J. Guo, K.-M. Lee, D. Zhu, X. Yi, and Y. Wang, "Large-deformation analysis and experimental validation of a flexure-based mobile sensor node," *IEEE/ASME Transactions on Mechatronics,* vol. 17, pp. 606-616, 2011.

[79] G. F. Franklin, J. D. Powell, and M. L. Workman, *Digital Control of Dynamic Systems,* 3rd ed. Menlo Park, CA: Addison-Wesley, 1998.

[80] D. Zhu, J. Guo, C. Cho, Y. Wang, and K.-M. Lee, "Wireless Mobile Sensor Network for the System Identification of a Space Frame Bridge," *IEEE-ASME Transactions on Mechatronics,* vol. 17, pp. 499-507, Jun 2012.

[81] Y. Q. Ni, B. Li, K. H. Lam, D. Zhu, Y. Wang, J. P. Lynch, *et al.*, "In-construction vibration monitoring of a super-tall structure using a long-range wireless sensing system," *Smart Structures and Systems,* vol. 7, pp. 83-102, 2011.

[82] A. T. Zimmerman, M. Shiraishi, R. A. Swartz, and J. P. Lynch, "Automated modal parameter estimation by parallel processing within wireless monitoring systems," *Journal of Infrastructure Systems,* vol. 14, pp. 102-113, 2008.

[83] R. A. Swartz, D. Jung, J. P. Lynch, Y. Wang, D. Shi, and M. P. Flynn, "Design of a wireless sensor for scalable distributed in-network computation in a structural health monitoring system," in *Proceedings of the 5th International Workshop on Structural Health Monitoring,* Stanford, CA, 2005.

[84] R. A. Swartz and J. P. Lynch, "Strategic network utilization in a wireless structural control system for seismically excited structures," *Journal of Structural Engineering,* vol. 135, pp. 597-608, 2009.

[85] J. N. Juang and R. S. Pappa, "An eigensystem realization algorithm for modal parameter identification and modal reduction," *Journal of Guidance Control and Dynamics,* vol. 8, pp. 620-627, 1985.

[86] F. McKenna. (2001, October 27). *OpenSees: Open System for Earthquake Engineering Simulation (web page and software).* Available: http://opensees.berkeley.edu/

[87] F. N. Catbas, S. K. Ciloglu, O. Hasancebi, K. Grimmelsman, and A. E. Aktan, "Limitations in structural identification of large constructed structures," *Journal of Structural Engineering,* vol. 133, pp. 1051-1066, 2007.

[88] E. Aktan, N. Catbas, A. Türer, and Z. Zhang, "Structural identification: analytical aspects," *Journal of Structural Engineering,* vol. 124, pp. 817-829, 1998.

[89] MathWorks Inc., *Optimization Toolbox™ User's Guide*, R2011b ed. Natick, MA: MathWorks Inc., 2011.

[90] D. Zhu, X. Yi, Y. Wang, K.-M. Lee, and J. Guo, "A mobile sensing system for structural health monitoring: design and validation," *Smart Materials and Structures,* vol. 19, p. 055011, 2010.

[91] D. Zhu, X. Yi, and Y. Wang, "Sensitivity analysis of transmissibility functions for structural damage detection," presented at the Proceedings of SPIE, Nondestructive Characterization for Composite Materials, Aerospace Engineering, Civil Infrastructure, and Homeland Security V, San Diego, CA, USA, 2011.

[92] E. M. Godfrin, "A method to compute the inverse of an n-block tridiagonal quasi-Hermitian matrix," *Journal of Physics: Condensed Matter,* vol. 3, p. 7843, 1991.

[93] D. Zhu and Y. Wang, "Substructure model updating through iterative convex optimization," in *Proceeding of the ASME 2012 Conference on Smart Materials, Adaptive Structures and Intelligent Systems (SMASIS 2012)*, Stone Mountain, GA, USA, 2012.

[94] S. P. Boyd and L. Vandenberghe, *Convex Optimization*. Cambridge, UK ; New York: Cambridge University Press, 2004.

[95] M. Grant and S. Boyd. (2014, Feb). *CVX: MATLAB software for disciplined convex programming, version 2.0*. Available: http://stanford.edu/~boyd/cvx.

[96] J. Moré, "The Levenberg-Marquardt algorithm: Implementation and theory," in *Numerical Analysis*. vol. 630, G. A. Watson, Ed., ed Berlin, Heidelberg, Germany: Springer, 1978, pp. 105-116.

[97] D. Zhu, X. Dong, and Y. Wang, "Substructure model updating through iterative minimization of modal dynamic residual," presented at the Proceedings of SPIE, Nondestructive Characterization for Composite Materials, Aerospace Engineering, Civil Infrastructure, and Homeland Security, San Diego, California, USA, 2014.

[98] D. Zhu, X. Dong, and Y. Wang, "Substructure model updating through modal dynamic residual approach," presented at the Proceedings of the 9th International Workshop on Structural Health Monitoring (IWSHM), Stanford, CA - USA, 2013.

[99] K. Alvin, "Finite element model update via Bayesian estimation and minimization of dynamic residuals," *AIAA journal*, vol. 35, pp. 879-886, 1997.

[100] T. Marwala and S. Sibisi, "Finite element model updating using Bayesian framework and modal properties," *Journal of Aircraft*, vol. 42, pp. 275-278, 2005.